UNIVERSITÀ DEGLI STUDI DI NAPOLI FEDERICO II

Dipartimento di Ingegneria Civile, Edile e Ambientale

Dottorato di Ricerca in

Ingegneria dei Sistemi Civili XXXVIII ciclo

Ph.D. student

Mehdi Valizadeh

Research Title

Smoothed Particle Hydrodynamics (SPH) model for numerical simulation of Non-Newtonian Fluids Flows

Ph.D. coordinator:

Prof. Ing. Andrea Papola

Tutor:

Prof. Ing. Cristiana Di Cristo

Prof. Ing. Stefano Sibilla

Abstract

Numerical simulations of mudflows are crucial in different fields of application such as environmental management and geotechnical engineering. Accurate modelling of such free-surface flows is vital for risk assessment and mitigation yet remains challenging because of their multiphase nature. They are usually described as continuous fluid with a non-Newtonian rheology, with shear-thinning or shear-thickening behaviour. Smoothed Particle Hydrodynamics (SPH), a fully Lagrangian and mesh-free method, provides an effective framework for simulating free-surface flows of both Newtonian and non-Newtonian fluids, also highly unsteady dynamics condition. In the present work, a new SPH code, PVSPH, was developed to investigate gravity-driven dam-break flows of non-Newtonian fluids describing mudflows. The study addresses the complex rheology of concentrated sediment–water mixtures by implementing a generalized power-law model for describing the fluids characteristics. The incorporation of power-law models into the SPH model represents the main original contribution of the work and it furnishes an accurate PVSPH method for reproducing mudflows. The PVSPH results are compared with the output of two Eulerian approaches: a depth-averaged model (EDAM) and a depth-resolved model (EDRM).

The PVSPH code was validated through appropriate test cases considering turbulent water and non-Newtonian laminar fluid flows. The first validation is performed with the SPHERIC dam-break benchmarks (both dry and wet bed) for water. To validate the code with power-law fluids the analytical solution of the plane Poiseuille flows was adopted. All preliminary tests were used to tune numerical parameters, including particle resolution, artificial viscosity, CFL number, smoothing coefficients, time integration scheme, etc. The PVSPH code successfully reproduced benchmarks and analytical solutions with generally low errors. In the SPHERIC dry-bed tests, the model accurately matched the measured free-surface profiles, yielding an RMSE value as low as 3.4%. Although the RMSE for the wet-bed tests was slightly higher, the model still presented the height and shape of the wave, as well as the bubble formed by wave plunging. For the plane Poiseuille power-law fluid flow, the results yielded R^2 values greater than 0.95 and RMSE values typically below 4.5% across a wide range of rheological indices. Therefore, validation confirms the validity of the adopted PVSPH model in simulating dam-break flows of both Newtonian and non-Newtonian fluids.

Laboratory experiments of dam-break simulations with non-Newtonian fluids were conducted at the University of Zaragoza using a non-Newtonian shear-thinning fluid realized with Carbopol-940. Free-

surface measurements were obtained using an RGB-D device (Kinect v1), velocity fields were captured with Particle Image Velocimetry (PIV), and the speed of the removal gate was controlled by pressure. The experimental data, under elaboration, will provide information on the characteristics of the dam-break wave propagation and impact against a rigid obstacle. They will be subsequently used to evaluate the performance of the PVSPH code.

Numerical simulation of non-Newtonian dam-break were performed to study the characteristics of the phenomenon and the performance of the numerical models. Different power-law fluids with rheological indices n =0.1 and 0.2 were considered. The geometrical scheme is a flume with an upstream reservoir closed by a moving gate (dam-break scheme) and dry-bed condition downstream. Three different configurations were assumed: horizontal open-end channel; horizontal and inverse slope closed-end channels. By calculating the Reynolds number, it was observed that the flow was laminar for n =0.1 and transitional for n =0.2. Since the SPH simulations did not include specific turbulence modelling, the cases for n =0.2 were treated with caution. For all flume configurations in the dam-break simulations at the gate section, the numerical results showed consistent agreement between PVSPH, EDAM, and EDRM for higher viscosity (n =0.1) compared to lower viscosity (n =0.2). Due to the lower viscosity and greater ease of flow, the fluid depth of the returning wave for n =0.2 was approximately 20% higher than that for n =0.1 across all models with closed-end and inverse slope configurations.

This thesis provides new insights into debris-flow and mudflow behaviour by applying dam-break simulations with a novel mesh-free SPH approach. The findings are expected to serve as a foundation for future advancements in numerical techniques and risk mitigation. Moreover, the collected experimental data will provide information to study the phenomenon and will be used to verify the performance of numerical models.

Acknowledgements

First, I thank God for enabling me to successfully complete this important step in my life.

I would like to express my sincere gratitude to my supervisor, **Dr. Cristiana Di Cristo**, for her patience, continuous guidance, and invaluable support throughout every stage of this thesis, especially during the Eulerian simulation work. I am also grateful to her for giving me the opportunity to carry out my PhD research at the University of Pavia. This work would not have been possible without her dedicated assistance.

My heartfelt thanks go to my supervisor, **Dr. Stefano Sibilla**, whose advice and encouragement were fundamental throughout all stages of this thesis, especially during the Lagrangian (SPH) simulation work. I am also sincerely grateful to him for giving me the opportunity to pursue my doctoral studies at the University of Pavia. His continuous and invaluable support made this research possible.

I am deeply grateful to my co-supervisor, **Dr. Gabriella Petaccia**, for her guidance and kind support throughout my PhD journey, and for her essential role in enabling me to carry out my doctoral research at the University of Pavia.

I would like to extend my sincere thanks to my co-supervisor, **Dr. Andrea Vacca**, whose valuable assistance, suggestions, and thoughtful comments played a significant role in shaping and completing this thesis.

I also wish to express my sincere gratitude to **Dr. Michele Iervolino** for his guidance and valuable assistance in carrying out the Eulerian simulation work of this thesis.

A special thanks goes to **Dr. Sergio Martínez-Aranda** for his essential support during the experimental part of this research, carried out at the University of Zaragoza in Spain. His contributions were fundamental to the completion of this study.

I am also thankful to **Dr. Andrea Papola**, coordinator of the PhD program, for his support and guidance, and for providing me with all the necessary information throughout my academic journey.

Furthermore, I would like to express my deepest gratitude to **my wife and my son,** whose constant encouragement and support have sustained me throughout this path. I am forever indebted to them. I am also grateful to my family and my wife's family for their continuous support.

Finally, I would like to thank all the professors at the University of Napoli Federico II, the University of Pavia, and the University of Zaragoza, who contributed to my academic development and made my studies in Italy a truly memorable experience.

List of Contents

List of Figures

List of Tables

List of Abbreviations

AMR	Adaptive Mesh Refinement scheme
AOBC	Adaptive Open Boundary Condition
CFD	Computational Fluid Dynamics
CFL	Courant Friedrichs Lewy condition
CISPH	Corrected Incompressible SPH
COBC	Characteristic Open Boundary Condition
DEM	Discrete Element Method
EDAM	Eulerian Depth Averaged Model
EDRM	Eulerian Depth Resolved Model
FOBC	Flather's Open Boundary Condition
FVM	Finite Volume Methods
HLL	Harten-Lax-Van Leer scheme
ISPH	Incompressible SPH
LES	Large Eddy Simulation
MUSCL	Monotone Upstream-centered Scheme for Conservation Laws
NIR	Near-Infrared sensor
PIV	Particle Image Velocimetry
PVSH	Smoothed Particle Hydrodynamics which is developed by Pavia University
RMSE	Root mean square error
SPH	Smoothed Particle Hydrodynamics
SPHERIC	SPH European Research Interest Community
SWE	Shallow Water Equation
TiO_2	Titanium dioxide
WC-MPS	Weakly Compressible Moving Particle Semi-implicit
WCSPH	Weakly Compressible SPH

List of Symbols

$\vec{v}_i$	velocity of the fixed particle
$\vec{v}_j$	velocity of the neighboring particle
$\frac{\partial u}{\partial y}$	velocity gradient perpendicular to the plane of shear
f_i	acceleration term at fixed point
$\vec{n}$	unit vector normal to the surface S
Re_c	critical Reynolds number
ζ_{ij}	value is obtained from artificial viscous term
μ_0	zero-shear viscosity or viscosity at very low shear rates
μ_∞	infinite-shear viscosity or viscosity at very high shear rates
ν_i	kinematic viscosity of the interested particle
$\frac{D}{Dt}$	material derivative
P_i	absolute pressure acting on the interested particle
P_i	absolute pressure acting on the neighboring particle
c	speed of sound
$\langle f(x) \rangle$	approximate value of the scalar function $f(x)$ at the fixed point x
$\vec{g}$	gravitational acceleration
m_j	mass of the neighboring particles
p_0	reference pressure (Pa)
x'	position of the variable point
Π_{ij}	artificial viscosity
α_D	kernel's normalization constant.
α_Π	Monaghan's viscosity coefficient
β_Π	Monaghan's viscosity coefficient
λ_1	constant value (0.25)

λ_1	constant value (0.4)
μ_{eff}	apparent viscosity
$\nu\nabla^2.\vec{v}$	viscosity forces per unit volume
ρ_0	reference density (kg/m3)
ρ_j	density of the neighboring particles
ρ_l	density of the water
ρ_s	density of the solid
τ_y	yield stress
$\frac{\partial p}{\partial x}$	pressure gradient
Δt	temporal time step
$\nabla.f(x)$	divergent of the smoothing function
C_v	volume concentration of kaolinite suspension
dx'	infinitesimal volume element
h	smoothing length
H	source terms
i	fixed particle (interested particle)
j	neighboring particle
k	constant related to the smoothing function at x
k	flow consistency index
K	square of the maximum velocity
Kh	support radius (radius of the circumference of the domain of influence)
Ma	Mach number
n	flow behaviour index or rheological index
N	number of particles in the support domain.
n_1	constant value (12)
n_2	constant value (4)

Q	heat flux
q	relative distance of fixed and a variable point to the smoothing length
r_0	initial space between particles
U	local velocity at y
U_{max}	maximum velocity at the centerline
$W(x - x', h)$	kernel or smoothing function evaluated at the position $(x - x')$
β	momentum flux factor
$\gamma^{\cdot}$	shear rate
$\overline{\gamma^{\cdot}}$	cut-off shear rate
$\delta(x - x')$	Dirac delta function evaluated in the position $(x - x')$
τ_b	bottom shear stress
Ω	support domain
Re	Reynolds number
T	extra-stress tensor
$f(x')$	function value at the variable point
$f(x)$	function value at the fixed point
x	position of the fixed point
ε	Young's modulus (bulk modulus
λ	time constant or time scale for structural breakdown
μ	dynamic viscosity
τ	share stress
φ	parameter employed to prevent the denominator of a fraction from becoming zero when two particles approach one another.
ϑ	bed slope

Introduction

Debris and mudflows are dangerous natural phenomena that can cause significant damage to infrastructure, property, and human lives. Due to their catastrophic impact, analysing and predicting debris and mudflows is essential for risk assessment and designing countermeasures. Consequently, numerical models are important for predicting these physical processes. The study of debris and mudflows has historically relied on empirical observations and simple analytical models, with more recent approaches combining theoretical insights with advanced numerical simulations. Most of these numerical models are based on the assumption of laminar flow conditions. However, this simplification does not always represent the complex dynamics of real-world fluid behaviour, especially when dealing with non-Newtonian fluids, which exhibit shear-thinning or shear-thickening properties.

The development of numerical models for simulating non-Newtonian flows has gained considerable attention in recent years. One of the most popular approaches is Smoothed Particle Hydrodynamics (SPH), which is a fully Lagrangian, mesh-free and particle-based method. Smoothed Particle Hydrodynamics (SPH) was proposed independently by Lucy and by Gingold & Monaghan in 1977 to simulate nonaxisymmetric phenomena in astrophysics. SPH has shown great potential in simulating complex fluid dynamics (Ye et al., 2019), particularly in cases involving free-surface flows, multiphase flow modelling, and non-Newtonian fluids. SPH has become a powerful tool for simulating Newtonian and non-Newtonian fluid flows and providing several advantages in comparison to traditional grid-based methods. A primary advantage of SPH is its ability to simulate complex geometries and large deformations (Monaghan, 1994), making it particularly useful for simulating free surface and dam-break. In addition, SPH is extremely well-suited for modelling fluids with variable viscosity, thanks to its mesh-free nature can naturally accommodate changes in material properties. Recent studies have demonstrated that the Smoothed Particle Hydrodynamics technique has high potential to be applied in the development of the next generation of numerical models, including jet impact, multi-phase mixing processes, sloshing, wave-structure interactions, ocean modelling, flood inundation, tsunami modelling, and sediment transport modelling (Violeau and Rogers, 2016).

The ability of SPH to model non-Newtonian fluids was represented by Martys et al. (2010), who successfully applied SPH to simulate shear-thinning fluids and concentrated suspensions. The application of SPH to non-Newtonian fluid flows (spanning from generalized Newtonian fluids to complex viscoelastic fluids) has become popular in recent years (Ellero and Tanner, 2005; Fan et al., 2010). The SPH method has been applied in the simulation of non-Newtonian fluids using various rheological models, including Herschel-Bulkley (e.g., Laigle and Labbe 2017), Bingham (e.g., Zhu et al. 2010), and power-law (e.g., Shao and Lo, 2003; (Ellero and Tanner, 2005; Fan et al., 2010), and their impact against the obstacles (e.g., Wang et al. 2016; Laigle and Labbe 2017).

For a long time, dam-break flow has always been a significant challenge in civil engineering. It has led to catastrophic consequences, particularly in flood-prone areas, and has been the subject of extensive study through both analytical and experimental research (Stansby et al. 1998).

The application of SPH to dam-break simulations has a well-established history, starting with pioneering work by Monaghan (1994) and Cummins and Rudman (1999) for dry-bed simulations. Later, studies by Janosi et al. (2004) and Crespo et al. (2008) extended SPH to wet-bed simulations, further reinforcing its potential for simulating free-surface flows in complex environments.

The objective of this thesis is to enhance our understanding of gravity-driven dam-break flows of non-Newtonian fluids by developing a new Smoothed Particle Hydrodynamics (SPH) code, named PVSPH, to analyze debris and mudflows propagation, which present significant challenges due to their complex rheological behaviours. Then, in order to evaluate the model's accuracy and efficiency, the results obtained from the PVSPH model can be compared with those from other established numerical methods, such as Eulerian Depth Averaged Model (EDAM) and Eulerian Depth Resolved Model (EDRM).

Model validation is essential to ensure the reliability and accuracy of the SPH code (PVSPH) for simulating both Newtonian and non-Newtonian flows. In order to validate the model, the SPH European Research Interest Community (SPHERIC) has provided several benchmark cases, including several 2D dam-break flow scenarios characterized by varying initial water depths upstream of the gate and both dry and wet bed conditions (Janosi et al., 2004). Moreover, for validating the model for non-Newtonian fluids, the analytical velocity profile of the plane Poiseuille flow for a power-law fluid has been utilized. The results of the PVSPH model can be compared with those obtained from other numerical methods, such as EDAM and ERAM, as well as experimental data. By comparing the PVSPH model with other numerical methods and experimental results, this work will also contribute to the growing body of research on SPH's application for non-Newtonian fluids and offer new insights into the simulation of natural hazards such as debris and mudflows.

Thesis Outline

This thesis presents the numerical investigation and findings derived from the PhD project in the following order:

Introduction: This section introduces the Smoothed Particle Hydrodynamics (SPH) method, providing an overview of its principles, followed by a description of the background and objectives of the present study.

Chapter 1. Literature Review: A comprehensive review of the existing literature is provided in this chapter, focusing on the application of SPH in various fields. Specific areas covered include the application of SPH in free-surface flow modelling, multiphase flow modelling, dam-break simulations, and modelling non-Newtonian fluids (debris flows and mudflows).

Chapter 2. Model Description: This chapter presents a detailed description of the PVSPH model, the Shallow Water Equations model (EDAM), and the OpenFOAM model (EDRM), describing their theoretical foundations and their relevance to the current study.

Chapter 3. Experimental Campaign: This chapter discusses the experimental setup, including the preparation of the experimental facility, fluid preparation, free-surface measurement using an RGB-D sensor, and velocity measurement with a Particle Image Velocimetry (PIV) camera. The data collected is still being processed and will be used for future comparisons and studies.

Chapter 4. Results and Discussion: This section first presents the model validation against literature experimental water dam-break tests and for non-Newtonian fluids against the analytical plane Poiseuille flow solution. Subsequently, further comparisons are presented between numerical output and water dam-break experimental results. Finally, the results obtained from PVSPH, EDAM, and EDRM are also compared considering both water and non-Newtonian dam- break tests.

Chapter 5. Conclusion: This chapter summarizes the key findings of the thesis, presenting conclusions drawn from the study and potential directions for future research.

1. Literature Review

This chapter reviews prior research relevant to SPH-based dam-break modelling of non-Newtonian fluids and is organized into five parts: (i) Introduction to Smoothed Particle Hydrodynamics (SPH), (ii) Application of SPH in Free Surface Flow Modelling, (iii) Application of SPH in multiphase flow modelling, (iv) Application of SPH in non-Newtonian fluids: Debris flows and mudflows, and (v) Application of SPH in dam-break simulation.

1.1. Introduction to Smoothed Particle Hydrodynamics (SPH)

For several decades, Smoothed Particle Hydrodynamics (SPH) based on the Lagrangian approach, has been developed as a fundamental and effective methodology for modelling mud and debris flows. Compared to Eulerian methods, SPH offers many advantages due to its Lagrangian framework, enabling it to effectively handle problems such as asymmetrical flows, the existence of large voids, and rapid free surface flows of complex fluids in intricate geometries (Gomez-Gesteira, 2004).

The concept of SPH as a mesh-free method was developed to solve problems for large deformations and free surface flow (Simeunović and Steeb, 2019). Smoothed particle hydrodynamics was invented independently by Gingold and Monaghan, and Lucy, in 1977. Initially, it was introduced for astrophysical applications (Gingold and Monaghan, 1977), but due to its ability to integrate the complexity of physical problems, was widely used in solid and fluid mechanics (Dutra Fraga Filho 2019).

Generally, SPH has been extended to model a wide range of problems including compressible fluids (e.g., Takeda et al. 1994), incompressible fluids (e.g., Monaghan, 1994; Morris et al. 1997), deformation and impact problems (e.g., Swegle and Attaway, 1995), suspension flows (Tartakovsky et al. 2009), multiphase flows (e.g., Monaghan and Kocharyan, 1995; Sibilla et al. 2020), and multiphase flow in porous media (e.g., Tartakovsky et al. 2007; Gouet-Kaplan et al. 2009).

Among the most well-known in Smoothed Particle Hydrodynamics (SPH), Gingold and Monaghan, (1977) is widely recognized, and also Gomez-Gesteira, Rogers, Dalrymple, and Crespo (2010) provided an overview focusing on free surface flow hydrodynamics. The modelling of local scouring and sediment scouring using SPH was investigated by Sibilla (2008) and Khanpour (2016). Furthermore, a comprehensive study conducted in past, present and future of SPH for free surface flows by Violeau and

Rogers (2016), and by Gotoh and Khayyer (2018) in the context of coastal and ocean engineering. Recent developments in SPH methodology and applications were explored by Ye, Pan, Huang, and Liu (2019), with several specialized SPH books published, including those by Liu and Liu (2003), Violeau (2012), and Dutra Fraga Filho (2019).

1.2. Application of SPH in Free Surface Flow Modelling

Free surface flows in hydrodynamics are crucial to both industrial and environmental fields; however, simulating them is particularly challenging. This difficulty arises from the need to apply boundary conditions to a surface that moves in an unpredictable manner.

In the framework of continuum approach, an alternative to the traditional Eulerian mesh-based modelling is represented by the Smoothed Particle Hydrodynamics method for its attractive properties: it is fully Lagrangian, meshless and particle based, yielding advantages over the traditional grid-based numerical methods in modelling rapid free surface flows of complex fluids in complex geometries (Ye et al., 2019). In the case of free surface flow, physical boundary conditions must be met at this surface, and the interpolation accuracy near the boundary must be preserved. SPH naturally satisfies these boundary conditions, and surface tension forces are calculated for multiphase flows in cases where surface tension is a factor (Colagrossi et al. 2009; Li et al. 2011).

In 1994, Monaghan applied Smoothed Particle Hydrodynamics (SPH) for the first time to simulate free surface flows, with potential applications in coastal engineering and other fluid dynamics problems. His findings demonstrated that the SPH method, unlike most Eulerian methods, can be easily applied to simulate various hydrodynamic problems, such as complex, turbulent free surface flows and accommodate moving boundaries, due to its robustness, simplicity, and flexibility. However, it also encountered challenges related to time-stepping and density fluctuations within the fluid, which, if not properly managed, can impact the reliability and accuracy of the results.

Monaghan (1994) used a nearly compressible fluid for simulating free surface flow and derived the pressure using an equation of state. Even though the fluid was modelled as compressible, its behaviour closely resembled that of an incompressible fluid, where density variations were minimal.

In 1997, Monaghan conducted a shock tube simulation using the SPH method. The comparison of results demonstrated that SPH is capable of simulating complex fluid dynamics problems, such as shock waves, more effectively than Riemann-based methods.

Monaghan and Kos (1999) examined the SPH method and experimental tests to model the run-up and return of a solitary wave traveling over a shallow water surface near the shore with a vertical wall. Their findings showed that the solitary wave collapses, hits the wall without wrapping around the shore, splashes, curls over, and eventually returns as a turbulent wave. The comparison between the experimental and simulation results was highly satisfactory.

Dalrymple and Knio (2001) explored the application of Smoothed Particle Hydrodynamics (SPH) in modelling free surface flows with splashing, particularly for coastal dynamics. They applied SPH to simulate a wave tank with large amplitude waves to study wave breaking and the effects of waves on structures and walls, while also addressing boundary conditions and computational efficiency.

In 2002, Kitsionas and Whitworth studied the challenges associated with modelling boundaries in Smoothed Particle Hydrodynamics simulations. They specifically focused on the difficulty in accurately modelling the interaction between boundaries and the flow of nearby particles, which is crucial for simulating phenomena like thin boundary layers. To overcome this limitation, they introduced a technique called particle splitting, which significantly improves resolution in regions of interest. This approach proved effective in scenarios involving self-gravitating collapse, such as those in astrophysical contexts. They demonstrated that particle splitting helps avoid issues like the violation of the Jeans Condition, important for accurate simulations of gravitational collapse. The results were compared with those obtained from traditional methods like Adaptive Mesh Refinement (AMR), showing that particle splitting achieved similar accuracy with obviously lower computational cost.

A study conducted by Rogers et al. (2003) on the application of Smoothed Particle Hydrodynamics (SPH) in marine hydrodynamics, specifically focusing on simulating the free surface flow behind a naval vehicle. Their numerical studies showed the sensitivity and accuracy of the SPH method in relation to the particle size and the number of particles used. The results obtained from these simulations reported good agreement with experimental findings.

In 2003, Vaughan et al. developed a model of the Seiching basin using an SPH Lagrangian method. Their model was the first application of SPH in that field and also an initial step towards developing a model for wave breaking phenomena. Some of the advantages of their model include its ability to efficiently simulate free surfaces, manage complex and turbulent fluid flows, and account for fluid fragmentation. The results were compared with theoretical solutions and previous studies, demonstrated that the behaviour of the model is highly sensitive to the initial conditions and model parameters, which need to be determined carefully. They expected that the model could be applied to problems such as analysing forces on coastal structures and studying sediment transport in the coastal zone.

Molteni et al. (2007) investigated the use of new equations of state within the Smoothed Particle Hydrodynamics (SPH) framework to improve simulations of incompressible water flows. The new approach provided a smoother pressure response during violent impact events by explicitly incorporating internal energy terms, leading to improvements over the traditional Tait equation. In order to validate the model, a series of dam-break experiments were conducted, and the final results demonstrated a closer agreement with simulated pressures. This indicated the potential of the modified state equations to improve the accuracy and stability of SPH in simulating free surface flow problems.

Khayyer et al. (2008) introduced the Corrected Incompressible SPH (CISPH) method, which enhanced the standard ISPH by adding correction terms to preserve angular momentum and improve the accuracy of velocity fields. The CISPH method significantly refined the tracking of the water surface compared to both ISPH and VOF models. The model provided more accurate wave profiles, which closely matched laboratory measurements, and improved the representation of the water surface in both breaking and post-breaking waves.

An SPH-based framework to simulate local scour, combining a Lagrangian SPH solver for free surface flow with the Exner equation for bed evolution developed by Sibilla (2008). The model was tested on a laboratory setup involving a planar jet from a sluice gate over a protection apron. It successfully showed key features like jet diffusion, scouring depth, the location of the hydraulic jump, and was matched well with experimental data. However, the model did have some limitations, such as underestimating dune height and incomplete recirculation above the bed.

Ferrari et al. (2009) presented a 3D weakly compressible SPH method for modelling non-hydrostatic free surface flows. Their scheme incorporated third-order TVD Runge–Kutta time-stepping, and for the density equation, a monotone upwind flux was applied, eliminating the artificial-viscosity term. Additionally, a mirrored-particle wall method was used to ensure smooth pressure near solid boundaries. The model was implemented with parallelization and dynamic load balancing for large simulations. Validation against laboratory data demonstrated good agreement with experimental results and other numerical methods for mesh-convergent free surface evolution.

Ni et al. (2016) studied on the application of the Smoothed Particle Hydrodynamics method in simulating free surface flow, particularly with two new open boundary conditions: Adaptive Open Boundary Condition (AOBC) and Flather's Open Boundary Condition (FOBC). These methods were compared to traditional approaches, Characteristic Open Boundary Condition (COBC). Results reported that AOBC and FOBC are easier to implement and simulate disturbance propagation high effectively. The SPH-based Shallow Water Equation

(SWE) model using these boundary conditions was tested for real-world applications (the Okushiri tsunami). The results showed that the SPH-based SWE model is a useful and effective tool for simulating free surface flow over non-uniform coastlines and ocean floor areas.

Parallelization in Smoothed Particle Hydrodynamics (SPH) facilitates the efficient simulation of complex fluid dynamics problems, optimizes the use of available hardware resources, and ensures that simulations involving millions of particles are completed within a practical timeframe. Jagtap et al. (2021) introduced an efficient parallelization of the SPH algorithm on modern multi-core CPUs and GPUs, addressing challenges such as neighbour search scalability, force calculations, thread divergence, and memory access patterns.

1.3. Application of SPH in multiphase flow modelling

Smoothed Particle Hydrodynamics (SPH) has become an effective method for simulating multiphase flows, particularly in complex scenarios involving interactions between different fluid phases, such as air-water and water-sediment mixtures. In multiphase flow simulations, the Lagrangian SPH method has a significant advantage over Eulerian methods: the advection process is straightforward. This enables the direct identification of phase interfaces from the positions of particles and removes the need for a separate interface reconstruction step (Pozorski and Olejnik, 2024). In 1997, Monaghan for the first time used the SPH method to study two-phase flow.

Colagrossi and Landrini (2003) employed the Smoothed Particle Hydrodynamics (SPH) method to simulate interfacial flows, with a particular emphasis on two-phase flows such as dam-break and impact problems. They demonstrated that SPH can effectively model both compressible and incompressible fluids, which enhances simulation accuracy and resolves challenges such as the air-cushion effect on impact pressure. Their study focused on dam-break dynamics, including backward plunging breakers and air entrapment. Although some differences were observed in quantitative comparisons, these were likely due to the inherent complexity of wave-structure interactions and the limitations of experimental data.

Cuomo et al. (2007) developed a Smoothed Particle Hydrodynamics (SPH) model for simulating two-phase flows with high density and compressibility ratios, such as air–water interactions. The model integrated a Large Eddy Simulation (LES) turbulence approach and solved the compressible Navier–Stokes equations. The model was utilized to simulate wave impact on structures, and the results were compared with established numerical solvers, showing good agreement.

Fourtakas and Rogers (2016) used a two-phase SPH model (DualSPHysics) to simulate dam-break flow by integrating a Herschel-Bulkley-Papanastasiou model (enhanced with the Drucker-Prager yield criterion) and a sediment suspension model. The results of the proposed model had a satisfactory agreement with experimental data and numerical solutions, for scouring simulation in dry-bed dam-break.

Shi et al. (2019) developed an advanced two-phase Smoothed Particle Hydrodynamics (SPH) model to simulate massive sediment motion in free surface flows, focusing on the limitations of earlier single-phase and two-fluid SPH approaches. Their model relied on a continuum formulation of water-sediment mixtures, solving individual mass and momentum equations for each phase. By introducing a rheology-based constitutive law for intergranular stresses and using the drag force for interphase interactions, the model effectively represented sediment transport dynamics. The model's applicability was demonstrated in various scenarios such as underwater granular column collapse and dam-break erosion, by showing good agreement with experimental data. These findings confirmed the model's capability to simulate real-world sediment transport phenomena, such as in dam-break scenarios.

De Padova et al. (2022) represented a multi-phase Smoothed Particle Hydrodynamics (SPH) model to simulate hydraulic-jump oscillations and local scour downstream of bed sills. Their model uses a symplectic weakly compressible SPH (WCSPH) framework and represents water-sediment mixtures as two distinct phases with different rheologies. The model was validated by comparing results with laboratory measurements. They applied the standard k-ε turbulence model to simulate flow dynamics features including bed profiles, velocity fields, and turbulence intensities.

1.4. Application of SPH in dam-break simulation

In fluid dynamics, the simulation of dam-break has long been utilized as a benchmark for analytical and numerical solutions, assisting in the development of innovative flood mitigation measures (Sturm, 2010; Khayyer and Gotoh, 2010).

Several significant studies have addressed the problem of dam-break waves in horizontal channels, including the Ritter (1892), Dressler (1952 and 1954), and Whitham (1955).

A theoretical formulation of the two-dimensional dam-break problem was introduced by Ritter (1892) for an inviscid fluid on a dry bed. Ritter assumed a smooth rectangular channel, an infinitely long reservoir, no energy losses, and hydrostatic pressure distribution. Subsequently, Dressler (1954) incorporated frictional effects by using Chezy's formula, and Whitham (1955) divided the wave profile into two regions, applying negligible resistance in the upper region and using integral forms of the momentum and continuity equations near the wave head in the second region. However, Ritter's foundational assumptions continue to be the most widely used basis for analytical calculations in dam-break investigations studies (Manciola et al. 1994).

The foundation for applying SPH in dam-break simulations was established by pioneering work on dry bed by e.g., Monaghan (1994) and Cummins and Rudman (1999), and on wet bed by e.g., Janosi et al. (2004), and (Crespo et al. 2008).

Janosi et al. (2004) added polyethylene oxide (PEO) (a water-soluble polymer with a high molecular weight) to water-based dam-break experiments to examine its effects on turbulence and drag. The finding indicated that PEO significantly reduced drag force in dry bed flows, whereas even a shallow layer of fluid at the downstream of the gate could effectively neutralize this effect. This emphasized the critical role of initial flow conditions and types of turbulence in SPH simulations of dam-break, which can accurately represent detailed hydrodynamic features such as the formation of gravity current, undular bore, and solitary wave following abrupt gate removal.

A study conducted by Gómez-Gesteira and Dalrymple, (2004) explores the use of a 3D Smoothed Particle Hydrodynamics (SPH) method to simulate wave impact on tall structures, with a focus on wave propagation from a dam-break. They found that simulations of dam-break scenarios in wet and dry beds yielded different results. Furthermore, the comparisons between the numerical results and experimental data showed good agreement in terms of velocity and force measurements.

Ata and Soulaïmani (2005), solve the Shallow Water Equations (SWEs) with an SPH method, based on the Riemann solution, by ignoring the friction terms and bed slope. The proposed model was a suitable tool for practical dam-break simulations at field scale.

In order to simulate real dam-break flows, Gu et al. (2017) solved Shallow Water Equations (SWEs) used the Smoothed Particle Hydrodynamics (SPH) method SWE-SPHysics by incorporating a Monotone Upstream-centered Scheme for Conservation Laws (MUSCL) and a virtual boundary particle method. The model results demonstrated its ability to accurately determine wet-dry boundaries of shallow dam-break flows.

Lee et al. (2008) compared the weakly compressible SPH (WCSPH) method with a semi-implicit incompressible SPH (ISPH) method for simulating incompressible flows. They concluded that ISPH offers significant improvements in simulating incompressible flows and provides more reliable results than WCSPH across various fluid dynamics applications. However, Hughes and Graham (2010) investigated the application of Smoothed Particle Hydrodynamics (SPH) to simulate free surface flows, particularly in scenarios involving overturning flows and impacts with solid surfaces. They applied two primary SPH approaches for modelling incompressible flows: weakly-compressible SPH (WCSPH) and incompressible SPH (ISPH). The study compared the performance of WCSPH and ISPH using two standard dam-break problems and water waves impacting a vertical wall. Their findings demonstrated that WCSPH performed as well as or in some cases better than ISPH.

Amicarelli et al. (2017) proposed a 3D Smoothed Particle Hydrodynamics (SPH) model for bed load transport on erosional dam-break floods, integrating a mixture model that combines both fluid and non-cohesive granular materials. The model which implemented in the SPHERA v8.0 code, was validated using experimental data from various 2D and 3D erosional dam-break cases. This approach demonstrated strong capabilities in simulating complex bed-load transport and sediment interactions. Their findings showed good agreement with experimental results, particularly in bed profiles and velocity distributions.

In 2023, LI et al. developed an improved Smoothed Particle Hydrodynamics (SPH) model for simulating dam-break floods. They concluded that the SPH method has many advantages, such as boundary issues and longer computational times compared to Finite Volume Methods (FVM).

1.5. Application of SPH to non-Newtonian fluids: Debris flows and mudflows propagation

The growing environmental concerns surrounding mudflows have initiated extensive research on their numerical simulation, particularly focusing on non-Newtonian fluids.

Mud and debris flows, characterized by sediment-water mixtures, are common in mountainous regions due to land instability and heavy rainfall (e.g., Iverson, 2000; Jeng and Sue, 2016) in presence of large quantities of sediments which, saturated with water, surge down steep slopes with high speeds (Iverson, 1997). These destructive flows often cause significant socio-economic damage, like human and material losses, and have a substantial environmental impact (Berti et al. 1999). These flows are often distinguished based on the quantity and the characteristics of the solid fraction (Takahashi, 2007) and mud-flows are characterized by highly-concentrated mixtures of water and fine sediments, in which volumetric solid concentration varies from 6 to 60 % (Ng and Mei, 1994; O'Brien, 2003)

Some examples of these catastrophic phenomena have occurred in Italy along the Amalfi coast, such as the mudflows in Minori, Maiori, and Vietri Sul Mare in 1954, and also more recently in Erchie in 2001 and Atrani in 2010 (Papa et al. 2013) These events show similarities in terms of meteorological, geomorphological, and urban contexts, such as Mediterranean rainstorms, steep slopes in small coastal catchments, and flood-prone rivers flowing under streets and squares (Ciervo et al. 2015). Due to their destructive impact, analysing and predicting mudflows and their interaction with structures is crucial for risk assessment and countermeasures design (Hungr et al. 1984). The increasing environmental concerns around these phenomena have led to extensive research on their reproduction.

One-phase models which consider the mixture as a homogeneous continuum with a non-Newtonian rheology, are more frequently used to describe mudflows. Unlike Newtonian fluids which maintain a linear relation between stress and rate-of-strain, fluids like mud show a non-Newtonian behaviour characterized by non-linearity between stress and rate-of-strain.

The numerical analysis of non-Newtonian behaviours holds significant importance in both academic and practical contexts, with over a century of continuous exploration. During this time, numerous mathematical models have been developed to understand and describe these complex behaviours, including generalized Newtonian models, linear or elementary nonlinear viscoelastic models, and memory-integral expansion models (Chen and Shu, 2020).

Different rheological models have been proposed, some considering yield stress, such as the Bingham (e.g., Imran et al. 2001) and Herschel–Bulkley models (e.g., Huang and Garcia, 1998), some neglecting it, such as the power-law model (e.g., Ng and Mei, 1994). The latter model is adequate to describe the behaviour of mudflows, landslides and flows of natural estuarine muds where deformation occurs continuously without any abrupt transition or yielding behaviour (Bai and Tian, 2011).

Sakakiyama and Byker (1989) developed a theoretical model for mud mass transport based on Newtonian fluid and conducted experiments with a kaolinite-water mixture that behaves as a Bingham fluid. They found that the transport of mud mass is directly proportional to a higher power of the surface wave height, with the model indicating differences in the transport profile compared to experimental observations, especially near the rigid bottom.

Ng and Mei (1994) developed a theory of permanent roll waves in a shallow layer of mud flow modelled as a power-law fluid, indicating that only wavelengths longer than a specific threshold are physically feasible. Additionally, highly non-Newtonian fluids can sustain very long roll waves even when the uniform flow is stable to infinitesimal disturbances.

The power-law model's applicability for various natural phenomena, including landslides and estuarine mudflows, is well-documented. In these scenarios, clay concentration, which can reach up to 80%, significantly increases the effective viscosity of water, altering its rheology (Ng and Mei, 1994).

In 2011, Soltanpour and Samsami investigated the rheological behaviour of kaolinite and a specific mud from southern Iran. They discovered that the rheological properties of mudflow, whether natural or artificial, are strongly dependent on the specific site.

A study conducted by Di Cristo et al. (2014) assessed the applicability of kinematic, diffusion, and quasi-steady wave models to the analysis of unsteady power-law mudflows. Through linear analysis, these simplified models were compared with the full dynamic model, demonstrating over 95% accuracy for predicting wave propagation characteristics. Also, they found the diffusion model to have a wider applicability range and noted that criteria used for turbulent clear-water flows are conservative when applied to power-law mudflows.

Shallow linearized models have been proven to be powerful tools for analysing a range of fluids (Di Cristo et al. 2014). They have been used to investigate instability conditions and wave dynamics in various fluids, including clear-water (e.g., Di Cristo et al. 2012), Herschel-Bulkley fluids (e.g., Coussot, 1994; Di Cristo et al., 2013a, 2013b, 2013c), dense granular flows (e.g., Forterre and Pouliquen, 2003; Di Cristo et al., 2009), and power-law fluids (Ng and Mei, 1994).

Under the long-wave approximation, i.e. using shallow-water models, numerous studies investigated the wave propagation generated by a sudden release of a finite volume of a non-Newtonian fluid downstream of a gate (Dam-break wave) and its interaction with obstacles (see for instance Bukreev, 2009; Kattel et al., 2018; Di Cristo et al. 2022). All these models are developed assuming that the pressure is hydrostatically distributed in the vertical direction and the shape of the velocity profile is the one pertaining to uniform condition. These assumptions can fail particularly when a strong wave-obstacle interaction occurs.

Without restoring the long-wave approximation, i.e. depth resolving the flow filed in the vertical direction, the free surface problem of the wave propagation with or without the rigid obstacle interaction has solved using both Eulerian and Lagrangian approaches.

In the former framework and tracking the free surface by using the volume of fluid (VOF) technique, the dynamics of a dam-break wave of several non-Newtonian fluids has been deeply analysed in absence of obstacles (see for instance: Minussi and Maciel, 2012; Liu et al., 2016; Schaer et al., 2018; Jing et al., 2018). Tang et al. (2022) developed a 2D depth-resolved numerical model based on Herschel-Bulkley rheology to study the impact of a dam-break wave against vertical structures.

The application of SPH modelling in debris flows and mudflows has been extensively examined (e.g., Yeylaghi et al., 2017; Jandaghian et al. 2021; Aslami et al. 2023; Yuan et al., 2024), demonstrating its adaptability and effectiveness in simulating debris flow dynamics. Below are some notable studies that highlight the application of the SPH framework in simulating non-Newtonian fluids.

Ellero et al. (2002) extended the Smoothed Particle Hydrodynamics (SPH) method to model viscoelastic and isothermal flows by adding a differential constitutive equation for the anisotropic stress using the simple corotational Maxwell model. In a 2D channel-flow test, the method reproduced the expected oscillatory response of viscoelastic materials, with dissipation arising from stress evolution rather than artificial viscosity. This proposed SPH approach will be applicable to 3D viscoelastic time-dependent flows in complex geometries and can produce a more accurate representation of viscoelastic behaviour.

Shao and Lo (2003) introduced an incompressible SPH (ISPH) projection scheme for free surface flows. The scheme uses a predictor–corrector time-stepping method and enforces incompressibility by solving a pressure Poisson equation built with SPH-consistent gradient, divergence, and Laplacian operators. The model applied to both Newtonian (water) and non-Newtonian (mudflow) cases by the Cross rheological model. Validation against 2D dam-break experiments showed close agreement with laboratory results in terms of front positions and free surface profiles. Moreover, for the non-Newtonian case, the simulations also showed that mudflows propagate more slowly than water and develop much steeper fronts.

Ellero and Tanner (2005) developed a weakly-compressible SPH scheme to simulate viscoelastic fluids. Their approach discretized both the momentum and constitutive equations using the Oldroyd-B and UCM models and introduced a boundary particle method to manage stress evolution near walls. For Poiseuille flow at low Reynolds numbers, the results showed excellent agreement with analytical solutions across a wide range of Weissenberg numbers. For the UCM fluid, the simulations accurately represented wall-generated shear waves and achieved stable transients without requiring artificial diffusion.

To simulate unsteady free surface flows for both Newtonian and viscoelastic fluids (Maxwell and Oldroyd-B models) Rafiee et al. (2007) applied an incompressible SPH model (projection). The incompressibility condition was satisfied using a Poisson pressure equation within an explicit predictor–corrector algorithm. The model was validated with droplet impact and jet-buckling benchmark problems across a wide range of Weissenberg numbers. The results demonstrated stable and accurate free surface evolution, in comparison with available data.

A fully explicit three-step SPH algorithm for simulating incompressible inelastic non-Newtonian fluid flows introduced by Hosseini et al. (2007). Their algorithm calculated viscous stresses based on strain-rate invariants and maintained quasi-incompressibility by coupling density and pressure, which led to the solution of a pressure Poisson equation. The study used three constitutive models including power-law, Herschel–Bulkley, and Bingham. The method was validated through benchmark tests including a non-Newtonian dam-break, annular viscometer flow, and a mud gravity current under water. The results showed close agreement with experimental data and analytical solutions in both 2D and 3D domains.

A semi-implicit, matrix free Smoothed Particle Hydrodynamics (SPH) method developed by Fan et al. (2010) for modelling non-Newtonian, high viscosity polymer moulding flows. This technique integrated the generalized-Newtonian rheology with realistic polymer equations of state (Tait and SSY) to simulate compressibility under high-pressure conditions. They employed artificial pressure stabilisation to keep particles from becoming unstable under tension. This term guaranteed that the simulation remained stable at very low Reynolds numbers, where explicit SPH would not be effective. The method was validated using a silt flow benchmark and a 2D mould-filling case.

To improve the stability and accuracy of transient viscoelastic fluid flow simulations, Jiang et al. (2011) suggested a Corrected Smoothed Particle Hydrodynamics (CSPH) approach. Their model combined the standard SPH approximation for interior particles with Corrected SPH for exterior particles. The transient Couette flow, transient Poiseuille flow, and their combined state were simulated. The results were compared with both the analytical solution and the standard SPH method. The findings showed that CSPH provide greater accuracy and stability than the standard SPH method; however, it has a higher computational cost.

An incompressible SPH (ISPH) method was applied by Zainali et al. (2013) to investigate multiphase flows involving both Newtonian and non-Newtonian fluids. Their formulation included a pressure Poisson equation together with appropriate rheological models. The model was validated through benchmark tests, such as dam-break cases. The study demonstrated that ISPH can effectively model interface evolution, velocity distribution, and the effects of non-Newtonian properties. It also showed that ISPH can accurately simulate multiphase flow problems with high density and viscosity ratios.

Since Smoothed Particle Hydrodynamics (SPH) methods often suffer from inaccurate pressure fields, the diffusion-based incompressible SPH (ISPH) method, introduced by Lind et al. (2012) was developed by Xenakis et al. (2015) to achieve a more precise and nearly noise-free pressure field. They enhanced this approach by adapting it to simulate free surface generalized Newtonian fluids, including Bingham, power-law, and Herschel–Bulkley models. They integrated standard viscosity calculation techniques and a newly formulated viscous term to address the challenges posed by non-Newtonian stresses. The approach was validated through analytical and experimental results from plane Poiseuille flows and dam-break scenarios. The findings demonstrated that the enhanced ISPH method provided smoother and more accurate pressure predictions than traditional weakly compressible SPH (WCSPH) methods, aligning closely with results from control-volume finite element methods. Additionally, the study highlighted the stabilizing effect of particle-shifting techniques, particularly in representing realistic flow dynamics.

Wang et al. (2016) developed a 3D Smoothed Particle Hydrodynamics (SPH) framework in DualSPHysics for simulating debris flow propagation, using the full Navier–Stokes equations and the general Cross model to represent non-Newtonian fluid behaviour. For implementation in DualSPHysics, they utilized density diffusion techniques and Wendland kernels to ensure stable pressure and free surface evolution over complex terrain. The model's results were compared with the Yohutagawa debris flow event in Japan (2010), demonstrating strong performance in reproducing the debris flow process. The simulated deposition depth and mass volume showed excellent agreement with the observed data.

Yeylaghi et al. (2017) used the Incompressible Smoothed Particle Hydrodynamics (ISPH) method to study landslide-generated waves in Newtonian and non-Newtonian reservoir fluids, considering both rigid and deformable slide scenarios. They validated the model with experimental data, and findings showed that ISPH, as a mesh-free approach, effectively simulates slide motion, turbulence, and the evolution of the free surface in complex landslide-induced wave phenomena.

Hosseini et al. (2019) developed a weakly-compressible SPH by SPHysics2D code to simulate the interaction between Newtonian water and a non-Newtonian granular phase with a viscoplastic rheology model named μ(I) model. The model integrated Grenier et al. (2009) framework for particles of varying phases interacting at the interface, alongside Owen's model for the interaction of particles with various viscosities at their interfaces, and an equation-of-state pressure with a back-pressure correction for sediment. They validated the approach through simulations of granular-column collapse, dry and submerged landslide, and dam-break over an erodible bed. The results showed that the SPH model successfully reproduced free surface evolution, bed deformation, runout, and velocity fields, with satisfactory results that closely matched the laboratory data.

An improved Weakly Compressible Moving Particle Semi-implicit (WC-MPS) technique was presented by Jandaghian et al. (2021) to simulate immersed multiphase granular flows. The method introduced improvements in particle collision modelling and pressure calculation, enabling stable and accurate treatment of highly non-linear interactions between granular material and the surrounding fluid. Validation against experimental data showed that the developed WC-MPS could reproduce key flow features, such as velocity fields, granular deposition, and fluid–particle coupling, with higher accuracy than earlier particle methods. This study demonstrated the effectiveness of WC-MPS as a mesh-free approach for exploring complex multiphase flows involving granular materials.

Shi and Huang (2022) developed a weakly compressible GPU-accelerated SPH framework for simulating multiphase non-Newtonian flows using the Herschel–Bulkley rheology model. Their model incorporated a particle-shifting scheme with a modified diffusive term to reduce pressure oscillations, along with a large eddy simulation (LES) sub-particle stress term to account for viscoplastic and turbulent effects. The model was validated with several cases, including two-phase Poiseuille flow (Newtonian and non-Newtonian), a static tank, and an immersed debris flow test. The results demonstrated the model's ability to simulate multi-material free surface problems with large deformations, showing accurate interfacial pressure continuity and realistic velocity profiles.

Hejazi et al. (2023) developed an advanced incompressible SPH model to simulate wave attenuation and mud mass transport, indicating that the non-Newtonian behaviour impacts significantly on both wave dissipation and sediment movement.

To simulate non-isothermal viscoplastic mixed convection, such as droplet impact on a solid wall and dam-break flow, an improved SPH approach can be utilized. Xu and Yu, (2025) introduced an improved weakly-compressible SPH method for simulating non-isothermal viscoplastic free surface flows. To improve accuracy and stability, they combined the Herschel-Bulkley-Papanastasiou rheology with techniques such as kernel-gradient correction, δ-SPH density dissipation, and particle-shifting. The model validation results demonstrated its effectiveness in modelling temperature-dependent rheology and free surface dynamics, with outcomes comparable to those from other solvers.

Aslami et al. (2023) developed a 2D coupled depth-averaged SPH solver for shallow-water flows with 3D debris motion to simulate tsunami-driven debris transport. Their model is implemented in the open-source DualSPHysics framework with a Euler-Lagrange SWE-SPH scheme. The debris dynamics are modeled using the modified Morison equation, coupled with the Discrete Element Method (DEM) for the collision mechanism. The model was validated using data from physical experiments (Parma dam-break and the Okushiri tsunami, 1993) and analytical solutions. The final results demonstrated strong agreement in water levels, run-up, and debris trajectories. This method showed the capability to represent transport pathways for debris under extreme shallow-water conditions, proving its utility in simulating complex tsunami events.

Yuan et al. (2024) proposed a two-phase, two-layer Smoothed Particle Hydrodynamics (SPH) model for simulating surge waves induced by debris flows. The approach divides water and debris into separate layers and solves coupled continuity and momentum equations for both phases: the Navier–Stokes equations for water and Newton's second law for the solid phase within an SPH framework. Interfacial interactions are modeled using pressure and friction terms, and boundary treatments ensure stability in steep slope areas. Their model was validated using laboratory experiment data on debris flow. The findings showed good agreement in wave height, velocity, and run-up when compared to the simulated results.

2. Numerical Models

In this chapter, the Smoothed Particle Hydrodynamics (SPH) method, a fully Lagrangian and meshless approach, is discussed as an efficient technique for simulating free surface flows in both Newtonian and non-Newtonian fluids. The discretization of the governing equations using this method will also be explained. Additionally, the chapter discusses the use of different types of smoothing functions, the wall boundary conditions – such as neighbor particles –and other important aspects relevant to the SPH method. A brief description of the Eulerian Depth Averaged Model (EDAM) and Eulerian Depth Resolved Model (EDRM) will also be provided.

2.1. Fundamental Concepts of SPH

Numerical simulation has become an essential tool in engineering and science for solving complex physical problems. It reduces the need for costly, time-consuming, or hazardous experiments, offering deeper insights compared to traditional methods. By discretizing the governing equations with appropriate initial and boundary conditions, simulations can accurately approximate real-world phenomena. The quality of the mesh and discretization significantly affects the results, linking numerical theory with practical applications. Numerical simulations also validate theories, interpret experimental findings, and bridge the gap between theoretical predictions and experimental observations, providing a powerful method for understanding in the fields of science and engineering (Liu and Liu, 2003).

The SPH method, first introduced independently by Lucy (1977) and by Gingold & Monaghan (1977) for astrophysical modelling, discretizes a continuous domain into a finite set of particles. These particles possess physical quantities which, rather than being local, are distributed in space through a weighted interpolation depending on a finite distance h, defined as smoothing length. Being the physical quantities defined in a discrete way only at the particle locations, only neighboring particles within a defined influence zone (up to a distance of κh) affect the properties of the interested particle (see Figure 2.1). The support domain is therefore circular (in 2D) or spherical (in 3D) with a radius equal to κh.

SPH relies on a mathematical identity that applies to any continuous function $f(x)$ of the position x, as shown in the following equation:

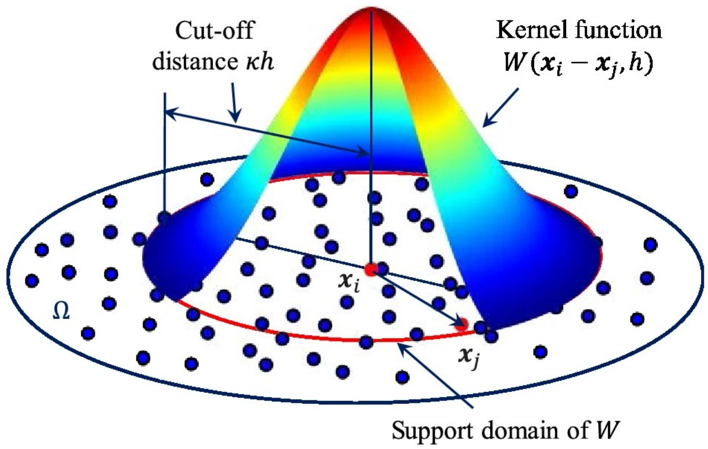

Figure 2. 1. Schematic representation of a 2D SPH particle approximation of reference particle *i* whose its physical properties influenced by the neighbor particles j inside the support domain of the kernel function *W* (Li et al., 2022)

The concept of the integral form of the function $f(x)$ used in the SPH method is summarized below:

$$f(x) = \int_{\Omega} f(x')\delta(x - x')\, \mathrm{d}x' \tag{2.1}$$

where,

- x is the position of the fixed point
- x' is the position of the variable point
- Ω is the domain
- $f(x)$ is the value of the scalar function at the fixed point
- $f(x')$ is the value of the scalar function at the variable point
- $\delta(x - x')$ is the Dirac delta function evaluated in the position $(x - x')$, equal to 1 if $x = x'$, 0 otherwise
- $\mathrm{d}x'$ is the infinitesimal volume element

Equation (2.1) has general validity, provided that $f(x)$ is a regular and continuous function, and shows that a function can be represented in an integral form.

That equation can constitute the basis for an interpolation over Ω by substituting the Dirac delta function $\delta(x - x')$ with a kernel function $\mathrm{W}(x - x', h)$. The integral representation of $f(x)$ is thus obtained by:

$$\langle f(x)\rangle = \int_{\Omega} f(x')\mathrm{W}(x-x',h)\,dx' \qquad (2.2)$$

where,

- $\langle f(x)\rangle$ is the approximate value of the scalar function $f(x)$ at the fixed point x
- h is the smoothing length defining the influence area of the smoothing function W
- W is smoothing kernel function
- $\mathrm{W}(x-x',\mathrm{h})$ is the smoothing kernel function evaluated in the position $(x-x')$

To be consistent with (2.1), $\mathrm{W}(x-x',\mathrm{h})$ must approximate the Dirac delta function and, therefore, have the following properties:

- symmetry $\quad W(x-x',h) = W(x'-x,h)$
- positivity $\quad W(x-x',h) \geq 0$
- compact support *Ω* $\quad W(x-x',h) = 0 \quad \text{if} \quad |x-x'| \geq \kappa h$
- tending to the Dirac d function $\quad \lim_{\mathrm{h}\to 0} \mathrm{W}(x-x',\mathrm{h}) = \delta(x-x')$
- normalization (unity condition) $\quad \int_{\Omega} \mathrm{W}(x-x',\mathrm{h})\mathrm{d}x' = 1$

where,

- κ is a constant related to the smoothing function at *x, as a* non-zero area of the smoothing function.

Any function that satisfies the properties mentioned above can serve as a smoothing kernel function in the SPH method.

By using the Taylor series expansion of $f(x')$ around *x*, where $f(x')$ (Eq. 2.2) is differentiable, one obtains:

$$\langle f(x)\rangle = \int_{\Omega} [f(x) + f'(x)(x-x') + \mathrm{r}((x-x')^2)]W(x-x',\mathrm{h})\,\mathrm{d}x' =$$

$$= f(x) \int_\Omega W(x - x', \mathrm{h})\, \mathrm{d}x' + f(x') \int_\Omega (x - x') W(x - x', \mathrm{h})\, \mathrm{d}x' + \mathrm{r}(h^2) \tag{2.3}$$

where r stands for the residual.

Since the smoothing function is required to be an even function:

$$\int_\Omega (x - x') W(x - x', \mathrm{h})\, \mathrm{d}x' = 0 \tag{2.4}$$

the kernel approximation becomes:

$$\langle f(x) \rangle = f(x) + \mathrm{r}((h^2) \tag{2.5}$$

Therefore, in the SPH method, the kernel approximation of a function is of second order accuracy.

2.1.1. Kernel approximation of derivatives

In order to obtain an SPH approximation of the divergence of the vector function $f(x)$ we can be substituted $\nabla \cdot f(x)$ in Eq. (2.2) to obtain its kernel approximation:

If $f(x)$ is continuous and differentiable on Ω:

$$\langle \nabla \cdot f(x) \rangle = \int_\Omega [\nabla \cdot f(x')] W(x - x', \mathrm{h})\, \mathrm{d}x'$$

which, according to the property of the derivative of a product, becomes:

$$\langle \nabla \cdot f(x) \rangle = \int_\Omega \nabla \cdot [f(x') W(x - x', \mathrm{h})]\, \mathrm{d}x' - \int_\Omega f(x') \cdot \nabla W(x - x', \mathrm{h})\, \mathrm{d}x' \tag{2.6}$$

Applying the divergence theorem to the first term on the right-hand side, (1.6) becomes:

$$\langle \nabla \cdot f(x) \rangle = \int_{\delta\Omega} f(x') W(x - x', \mathrm{h}) \cdot \vec{\mathrm{n}}\mathrm{ds} - \int_\Omega f(x') \cdot \nabla W(x - x', \mathrm{h})\, \mathrm{d}x' \tag{2.7}$$

Here $\vec{n}$ is the unit vector normal to the surface $\delta\Omega$, where the kernel function is zero on its domain boundary. The first integral in (2.7) vanishes, leaving:

$$\langle \nabla \cdot f(x) \rangle = -\int_{\Omega} f(x') \cdot \nabla W(x - x', \mathrm{h})\, \mathrm{d}x' \tag{2.8}$$

Equation (2.8) indicates that the derivative operator in the integral approximation is transferred to the kernel smoothing function (Liu and Liu, 2003).

Similarly, kernel approximations of 2nd order derivatives can be built:

$$\frac{\partial f(x_i)}{\partial x_i \, \partial x_j} = \int_{\Omega} f(x') \frac{\partial W(x' - x, \mathrm{h})}{\partial x_i \, \partial x_j}\, \mathrm{d}x' \tag{2.9}$$

leading to a possible kernel approximation of the Laplacian of a function:

$$\nabla^2 . f(x_i) = \int_{\Omega} f(x') . \nabla^2 W(x' - x, \mathrm{h})\, \mathrm{d}x' \tag{2.10}$$

However, Sibilla (2015) showed that the numerical approximation of the viscous terms of the Navier-Stokes equations obtained by direct SPH discretization of eq. (2.10) can be rather poor.

2.1.2. Discretization of the continuum domain

In the Smoothed Particle Hydrodynamics approach, the system is depicted by a discrete set of particles, each possessing its own mass. This is accomplished through a particle-based approximation, which is a fundamental operation in SPH techniques. For all particles in the support domain, the continuous integral representations linked to the SPH kernel approximation can be translated into discrete summation forms (Liu and Liu, 2003), as shown in Fig. 2.2.

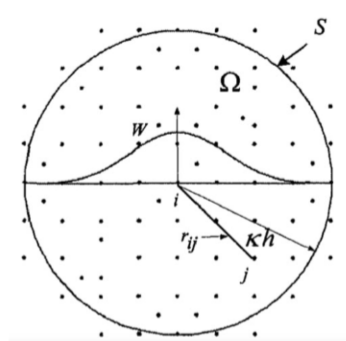

Figure 2. 2. Approximations of particles utilizing particles within the support domain of the smoothing function W for particle i (Morris, 1995)

If the infinitesimal volume $\mathrm{d}x'$ at particle j is replaced by the finite particle volume ΔV_j related to its mass m_j and density ρ_j :

$$\Delta V_j = \frac{m_j}{\rho_j} \tag{2.11}$$

In this way, eq. (2.2) can be written in discrete form by approximating the volume integral with a summation extended to all the *N* particles located inside the support domain *Ω*:

$$f(x_i) = \sum_j \frac{m_j}{\rho_j} f(x_j) W\left(x_i - x_j, h\right), \qquad \text{if } \left|x_i - x_j\right| \leq \kappa h \tag{2.12}$$

In particular, the particle approximation of density takes the form:

$$\rho_i = \sum_{j=1}^{N} m_j W_{ij} \tag{2.13}$$

where,

the compact notation $W_{ij} = W\left(x_i - x_j, h\right)$ is adopted.

The SPH approximation of $\nabla f(x_i)$ is obtained in analogy:

$$\langle \nabla f(x_i) \rangle = \sum_j \frac{m_j}{\rho_j} f(x_j) \nabla W_{ij} \tag{2.14}$$

as well as the SPH approximation of the divergence of a vector function $\nabla \cdot f(x_i)$:

$$\nabla \cdot f(x_i) = \sum_j \frac{m_j}{\rho_j} f(x_j) \cdot \nabla W_{ij} \tag{2.15}$$

2.1.3. SPH approximations to the conservation equations

In the SPH technique, the governing equations must be expressed as particle approximations. The fundamental governing equations of fluid motion (conservation of mass and momentum) are presented here.

2.1.3.1. Mass Conservation

The continuity equation can be written:

$$\frac{D\rho}{Dt} + \rho\nabla.\vec{\mathrm{v}} = 0 \ , \qquad \rho\vec{\nabla}\cdot\vec{\mathrm{v}} = \vec{\nabla}\cdot(\rho\vec{\mathrm{v}}) - \vec{\mathrm{v}}\cdot\vec{\nabla}\rho \tag{2.16}$$

the SPH approximation can be obtained:

$$\frac{D\rho_i}{Dt} = \sum_j m_j(\vec{\mathrm{v}}_i - \vec{\mathrm{v}}_j)\cdot\vec{\nabla}W\left(x_i - x_j, \mathrm{h}\right) \tag{2.17}$$

where,

- $\vec{\mathrm{v}}_i$ is the velocity of the fixed particle
- $\vec{\mathrm{v}}_j$ is the velocity of the neighboring particle

2.1.3.2. Momentum Conservation

The following is the momentum conservation equation:

$$\frac{D\vec{\mathrm{v}_i}}{Dt} = -\frac{\nabla \mathrm{P}}{\rho} + \frac{1}{\rho}\nabla.\vec{\tau} + \vec{g} \tag{2.18}$$

the pressure term in the momentum equation can be written:

$$\frac{\nabla p}{\rho} = \nabla\left(\frac{p}{\rho}\right) + \frac{p}{\rho^2}\nabla\rho \ , \quad \left\langle\frac{\nabla \mathrm{P}}{\rho}\right\rangle = \sum_j m_j\left[\frac{P_i}{{\rho_i}^2} + \frac{P_j}{{\rho_j}^2}\right]\nabla W\left(x_i - x_j, \mathrm{h}\right) \tag{2.19}$$

the viscous stress term can be computed:

$$\vec{\tau}_i = \mu_i\left(\vec{\nabla}\vec{\mathrm{v}}_i + \vec{\nabla}\vec{\mathrm{v}}_i^T\right), \quad \frac{1}{\rho}\nabla.\vec{\tau} = \frac{1}{\rho}\nabla.\left[\mu(\nabla\vec{\mathrm{v}} + \nabla\vec{\mathrm{v}}^T) - \frac{2}{3}\mu\nabla.\vec{\mathrm{v}}\right] \tag{2.20}$$

for incompressible form: $\nabla.\vec{\mathrm{v}} = 0$,

$$\frac{1}{\rho}\nabla.\vec{\tau} \cong \frac{1}{\rho}\mu\nabla^2.\vec{\mathrm{v}} = \nu\nabla^2.\vec{\mathrm{v}} \tag{2.21}$$

viscous stress can be computed by applying the second derivative directly to the kernel function:

$$\langle \nu \nabla^2 . \vec{\mathrm{v}} \rangle = \mathrm{v}_i \sum_j \frac{m_j}{\rho_j} \vec{\mathrm{v}}\, \nabla^2 W\left(x_i - x_j, \mathrm{h}\right) \tag{2.22}$$

alternatively, 2D viscous stress can be computed by direct estimation of the velocity gradient:

$$\begin{aligned} \sum_j \frac{m_j}{\rho_j}\left(\vec{\mathrm{v}}_j - \vec{\mathrm{v}}_i\right)\frac{\partial W(\vec{x}_i - \vec{x}_j, h)}{\partial x} &= \left.\frac{\partial \vec{\mathrm{v}}}{\partial x}\right|_i \sum_j \frac{m_j}{\rho_j}(x - x_i)\frac{\partial W(\vec{x}_i - \vec{x}_j, h)}{\partial x} + \left.\frac{\partial \vec{\mathrm{v}}}{\partial y}\right|_i \sum_j \frac{m_j}{\rho_j}(y - y_i)\frac{\partial W(\vec{x}_i - \vec{x}_j, h)}{\partial x} \\ \sum_j \frac{m_j}{\rho_j}\left(\vec{\mathrm{v}}_j - \vec{\mathrm{v}}_i\right)\frac{\partial W(\vec{x}_i - \vec{x}_j, h)}{\partial y} &= \left.\frac{\partial \vec{\mathrm{v}}}{\partial x}\right|_i \sum_j \frac{m_j}{\rho_j}(x - x_i)\frac{\partial W(\vec{x}_i - \vec{x}_j, h)}{\partial y} + \left.\frac{\partial \vec{\mathrm{v}}}{\partial y}\right|_i \sum_j \frac{m_j}{\rho_j}(y - y_i)\frac{\partial W(\vec{x}_i - \vec{x}_j, h)}{\partial y} \end{aligned} \tag{2.23}$$

the following SPH approximation can be obtained:

$$\frac{1}{\rho}\left\langle \vec{\nabla} \cdot \vec{\tau} \right\rangle_i = \sum_j \frac{m_j}{\rho_i \rho_j}\left(\vec{\tau}_i + \vec{\tau}_j\right) \cdot \vec{\nabla} W(\vec{x}_i - \vec{x}_j, h) \tag{2.24}$$

and, which can be directly applied also to non-Newtonian fluids flows:

$$\left\langle \vec{\nabla} \cdot \left(\mu \vec{\nabla} \vec{v}\right) \right\rangle = -\sum_j \frac{m_j}{\rho_j}\left(\mu_i + \mu_j\right)\frac{\vec{v}_{ij} \cdot \vec{r}_{ij}}{\left|\vec{r}_{ij}\right|^2 + \varepsilon h^2} \vec{\nabla} W(\vec{x}_i - \vec{x}_j, h) \quad , \quad \vec{r}_{ij} = \left(\vec{x}_i - \vec{x}_j\right) \tag{2.25}$$

consequently, the SPH approximation of Momentum Conservation can be written:

$$\frac{D\vec{\mathrm{v}_i}}{Dt} = \sum_j m_j \left[\frac{P_i}{{\rho_i}^2} + \frac{P_j}{{\rho_j}^2}\right] \nabla W(x - x', \mathrm{h}) + 2\mathrm{v}_i \sum_j \frac{m_j}{\rho_j}\left(\vec{\mathrm{v}}_j - \vec{\mathrm{v}}_i\right)\frac{(x_i - x_j)}{\left|x_i - x_j\right|^2} . \nabla W(x - x', \mathrm{h}) \; + \vec{g} \tag{2.26}$$

where,

- v_i is the kinematic viscosity of the interested particle
- P_i is the absolute pressure acting on the interested particle
- P_i is the absolute pressure acting on the neighboring particle
- $\vec{g}$ is the gravitational acceleration

2.1.4. Artificial viscosity

In order to avoid instabilities in shock waves and discontinuities and to prevent interpenetration of particle, Monaghan (1989) proposed to add an artificial viscosity term (Liu and Liu, 2003):

$$\Pi_{ij} = \begin{cases} \dfrac{-\alpha_\Pi \bar{c}_{ij} \zeta_{ij} + \beta_\Pi \zeta_{ij}^2}{\bar{\rho}_{ij}} \quad , & \vec{\mathrm{v}}_{ij} . x_{ij} < 0 \\ 0 & , \quad \vec{\mathrm{v}}_{ij} . x_{ij} > 0 \end{cases} \tag{2.27}$$

$$\zeta_{ij} = \frac{h_{ij}\vec{\mathrm{v}}_{ij}.x_{ij}}{|x_{ij}|^2+\varphi^2}, \ \bar{c}_{ij} = \frac{\bar{c}_i+\bar{c}_j}{2}, \ \bar{\rho}_{ij} = \frac{\bar{\rho}_i+\bar{\rho}_j}{2}, \ \ h_{ij} = \frac{h_i+h_j}{2}, \ \vec{\mathrm{v}}_{ij} = \vec{\mathrm{v}}_i - \vec{\mathrm{v}}_j, x_{ij} = x_i - x_j \tag{2.28}$$

$$\frac{D\vec{\mathrm{v}}_i{}^*}{Dt} = \frac{D\vec{\mathrm{v}}_i}{Dt} - \sum_j m_j \Pi_{ij} \vec{\nabla} W(x_i - x_j, h) \tag{2.29}$$

and, Eq (2.30) is the artificial viscosity term to be added to the Navier-Stokes equations.

$$\sum_j \frac{m_j}{\rho_j} \Pi_{ij} \vec{\nabla} W(x_i - x_j, h) \tag{2.30}$$

where,

- $\frac{D\vec{\mathrm{v}}_i{}^*}{Dt}$ represents the acceleration of the particle of interest, subsequent to the incorporation of the term associated with artificial viscosity into the momentum conservation equation (Dutra Fraga Filho, 2019)
- Π_{ij} is the artificial viscosity
- α_Π and β_Π are known as Monaghan's viscosity coefficient
- $\bar{c}_i$ and $\bar{c}_j$ are the velocities of sound in the interested and neighboring particles, respectively
- h_i and h_j are the support radius of the interested and neighboring particles, respectively
- φ is a parameter employed to prevent the denominator of a fraction from becoming zero when two particles approach one another.

2.1.5. Kernel functions

The core of the SPH discretization relies on the interpolation function which allows the computation of the flow properties and of their derivatives within the support domain Ω: its function is known, as previously said, the kernel, or smoothing function. A variety of kernel functions are available. The smoothing function must possess at least continuous second derivatives, and both the kernel and its derivatives should be computationally efficient. The choice of the kernel function affects the attainment of optimal approximations of the particles' physical attributes (Dutra Fraga Filho, 2019).

In the following, some of the most used kernel functions are summarized:

- Quartic bell-shaped kernel function (Fig. 1.3) (Lucy, 1977):

$$W(x-x',\mathrm{h}) = \alpha_D \begin{cases} (1+3q)(1-q) & q \leq 1 \\ 0 & q > 1 \end{cases} \tag{2.31}$$

where,

- α_D is $\frac{5}{\pi h^2}$ in 2D domain
- α_D is $\frac{105}{16\pi h^3}$ in 3D domain
- $q = \frac{|(x-x')|}{h}$

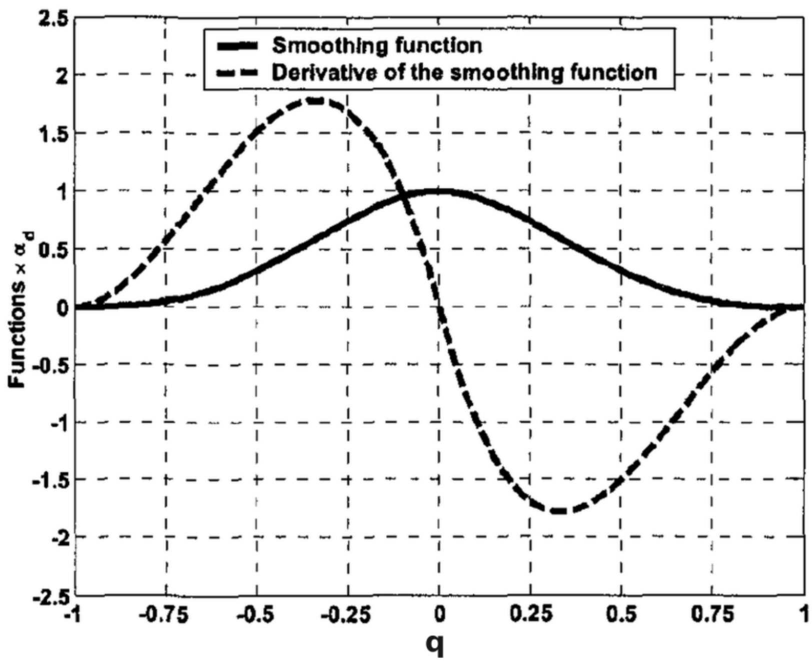

Figure 2. 3. The Quartic smoothing function and its first derivative (Lucy, 1977)

- Gaussian kernel function (Gingold and Monaghan, 1977):

$$W(x-x',\mathrm{h}) = \alpha_D e^{-q^2} \tag{2.32}$$

where,

- α_D is $\frac{1}{\pi h^2}$ in 2D domain
- α_D is $\frac{1}{\pi^{1.5} h^3}$ in 3D domain

- $q = \frac{|(x - x')|}{h}$

The Gaussian kernel has considerable smoothness even for high-order derivatives due to its high stability and accuracy, making it suitable for disordered particles (Fig. 1.4) (Liu and Liu, 2003). However, its support domain is theoretically infinite and must therefore be truncated at the required radius κh.

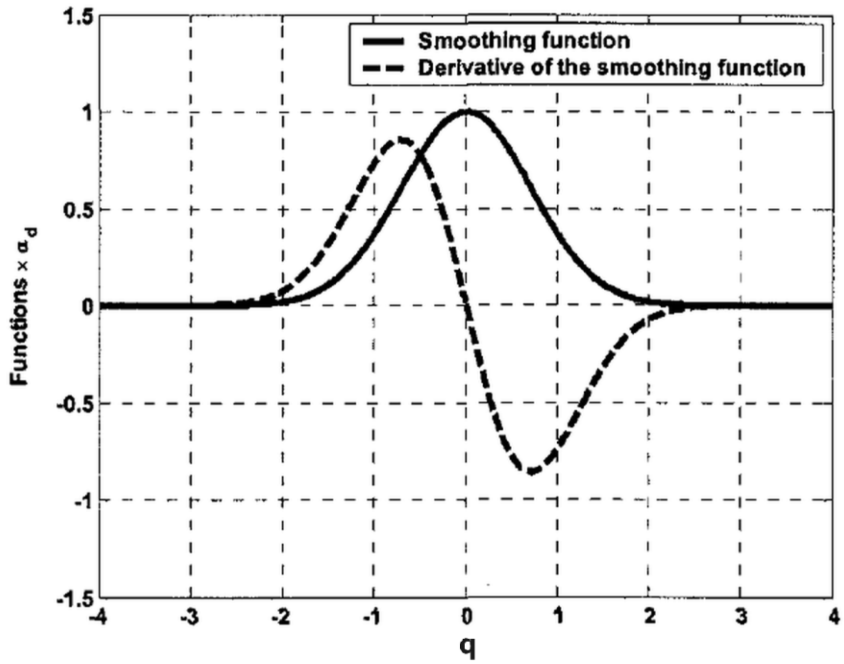

Figure 2. 4. The Gaussian kernel and its first derivative (Gingold and Monaghan, 1977)

- Cubic B-spline kernel function (Figure 1.5) (Monaghan and Lattanzio, 1985):

$$W(x - x', \mathrm{h}) = \alpha_D \begin{cases} \left(\frac{2}{3} - q^2 + \frac{q^3}{2}\right) & 0 \le q \le 1 \\ \frac{1}{6}(2 - q)^3 & 1 < q \le 2 \\ 0 & q > 2 \end{cases} \tag{2.33}$$

where,

- α_D is $\frac{15}{7\pi h^2}$ in 2D domain
- α_D is $\frac{3}{2\pi h^3}$ in 3D domain

- $q = \frac{|(x-x')|}{h}$

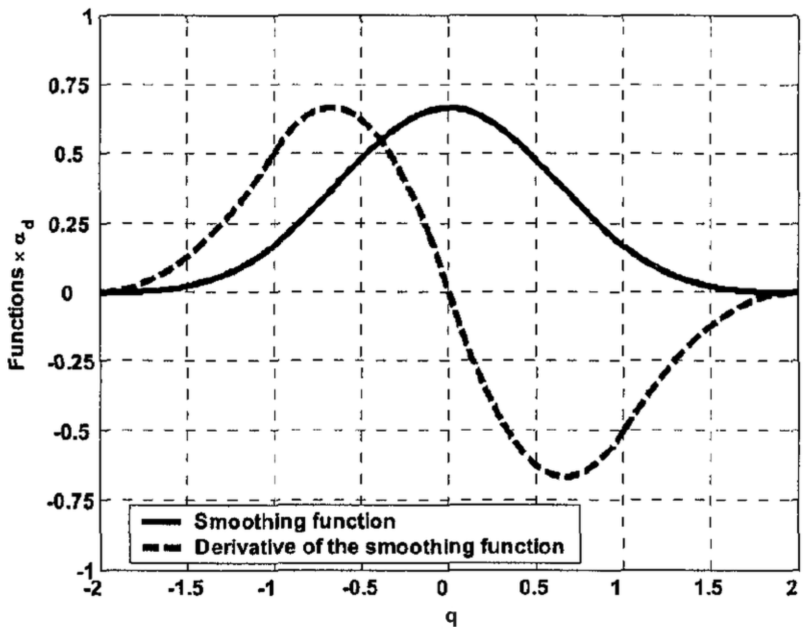

Figure 2. 5. The cubic spline kernel and its first derivative (Monaghan and Lattanzio, 1985)

- Wendland C-4 kernel function (Figure 1.6) (Wendland, 1995):

$$W(x-x',\mathrm{h}) = \alpha_D \begin{cases} \left(1-\frac{q}{2}\right)^5 \left[1+\frac{5}{2}q+2q^2\right] & 0 \le q \le 2h \\ 0 & q > 2h \end{cases} \tag{2.34}$$

where,

- α_D is $\frac{3}{2h}$ in 2D domain

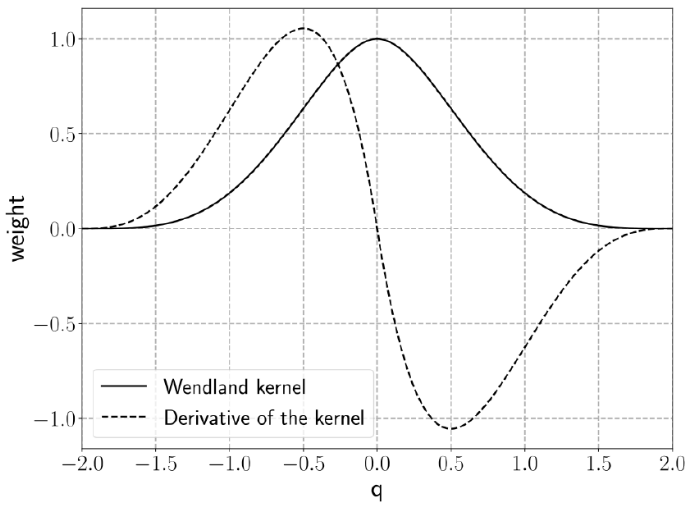

Figure 2. 6. The Wendland C-4 kernel function and its first derivative (Wendland, 1995)

- Quartic spline kernel function (Figure 1.7) (Morris, 1996):

$$W(x-x',\mathrm{h}) = \alpha_D \begin{cases} (q+2.5)^4 - 5(q+1.5)^4 + 10(q+0.5)^4 & 0 \le q < 0.5 \\ (2.5-q)^4 - 5(1.5-q)^4 & 0.5 \le q \le 1.5 \\ (2.5-q)^4 & 1.5 \le q \le 2.5 \\ 0 & q > 2.5 \end{cases} \tag{2.35}$$

where,

- α_D is $\frac{1}{24h}$ in 1D domain

- Quintic spline kernel function (Figure 1.8) (Morris, 1996):

$$W(x-x',\mathrm{h}) = \alpha_D \begin{cases} (3-q)^5 - 6(2-q)^5 + 15(1-q)^5 & 0 \le q < 1 \\ (3-q)^5 - 6(2-q)^5 & 1 \le q \le 2 \\ (2.5-q)^4 & 2 \le q \le 3 \\ 0 & q > 3 \end{cases} \tag{2.36}$$

where,

- α_D is $\frac{120}{h}$ in 1D domain
- α_D is $\frac{7}{478\pi h^2}$ in 2D domain

- α_D is $\frac{3}{359\pi h^3}$ in 3D domain

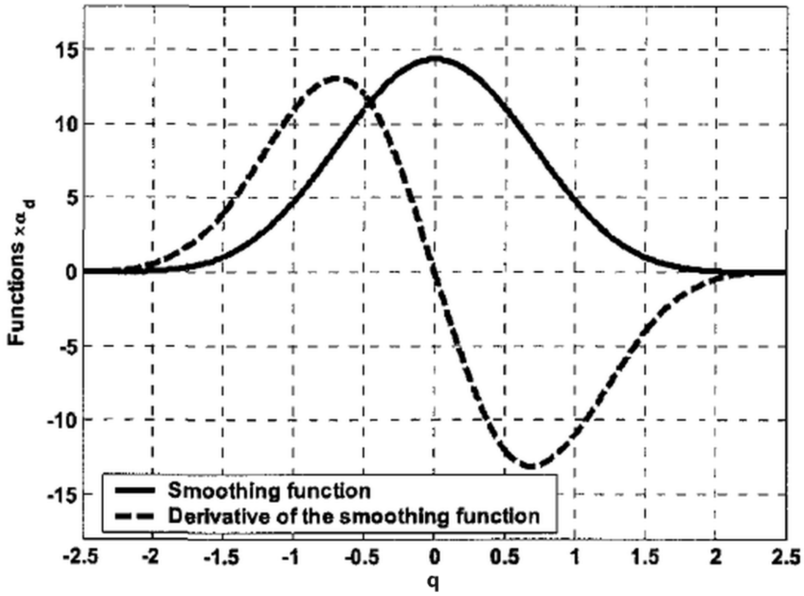

Figure 2. 7. The quartic smoothing function and its first derivative (Morris, 1996)

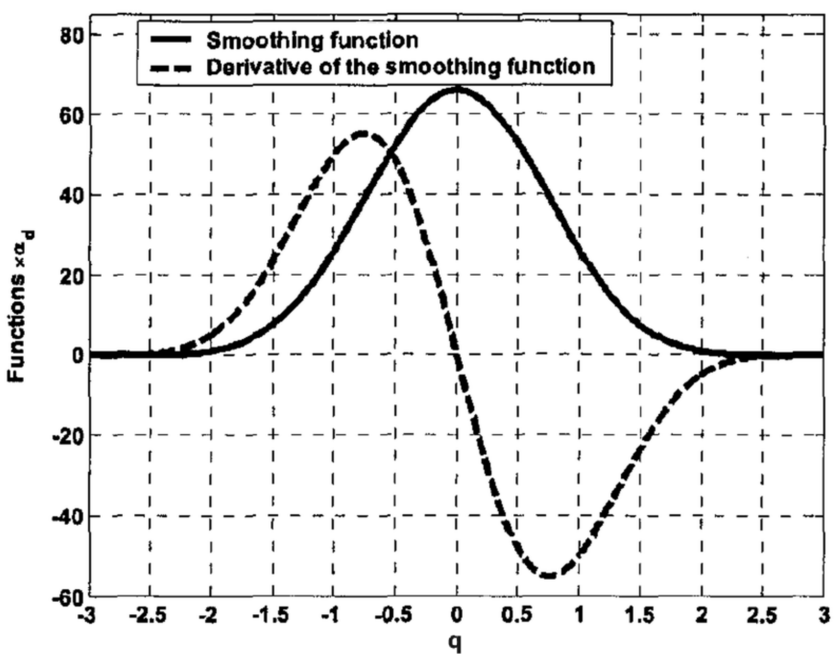

Figure 2. 8. The quintic smoothing function and its first derivative (Morris, 1996)

- Anti-cluster kernel function (Figure 1.9) (Gallati and Braschi, 2002):

$$W(x-x',\mathrm{h}) = \alpha_D \begin{cases} (2-q)^3 & 0 \leq q \leq 2h \\ 0 & q > 2 \end{cases} \tag{2.37}$$

where,

- α_D is $\frac{1}{8h}$ in 2D domain

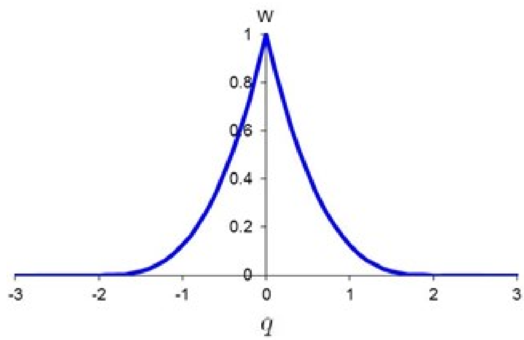

Figure 2. 9. The anti-cluster kernel function (Gallati and Braschi, 2002)

2.1.6. Boundary condition treatment

In the SPH approach, recognizing neighboring particles is essential because the method efficiency depends on the technique used for particle identification. In contrast to mesh-based methods, SPH requires finding neighbors based on a smoothing function, with only particles within a specified range influencing the calculation. Various techniques exist to identify the neighbors of a particle. Based on the compact support properties of the smoothing function, only a certain number of particles are located within the range of influence of the associated particle and are utilized in the particle approximation. Particle deficiency near boundaries presents a further issue, as boundary particles have no interactions beyond the domain. To overcome this challenge, three main classes of methods have been proposed, i.e. the Ghost (mirror) particle model, the real (dynamic) particle model, and the repulsive force (Boundary particle force model) methods (see Figure 1.10).

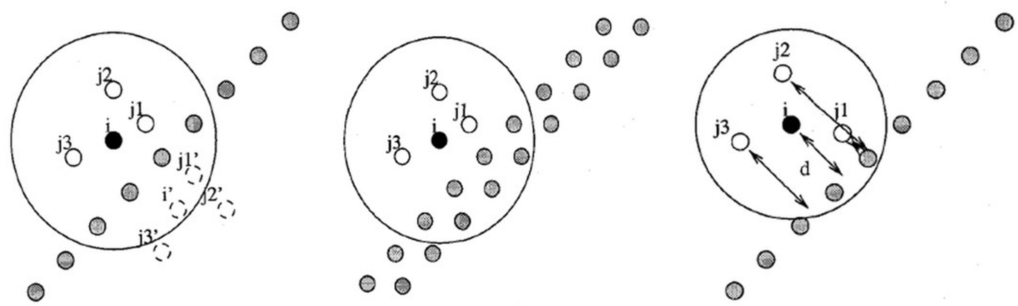

Figure 2. 10. Three kinds of SPH boundary conditions: ghost (left), dynamic (center) and repulsive force boundary (right) (Zou, 2007)

2.1.6.1. Ghost particle method

Libersky et al. (1993) introduced ghost particles for symmetrical surface boundary conditions. Then, Monaghan (1994) used ghost particles on the boundary to create a repulsive force and prevent penetration. Randles and Libersky (1996) assigned boundary values to ghost particles and interpolated these with interior values. Liu et al. (2002) introduced the method with ghost particles for solid boundary conditions. This method offers several benefits, including ease of implementation for plane boundaries, computational efficiency, effective prevention of particle penetration, and the restoration of consistency at boundaries. However, it also has some limitations, such as difficulty in handling irregular boundary shapes or two-phase flow scenarios. Additionally, curved boundaries can result in coarser or finer particle distribution, and corners generate duplication of ghost particles.

2.1.6.2. Dynamic particle method

The Dynamic Particles method introduced by Dalrymple and Knio (2001) is considered more stable and provides accurate results compared to other approaches, particularly when the smoothing length is carefully chosen. In this approach, boundary particles follow the same equations, including the momentum, continuity, and equation of state. However, the particles do not move according to the motion equations; they remain fixed or move based on external factors. The density of the boundary particle increases when a fluid particle approaches it, leading to a rise in pressure and, consequently, an applied force due to the pressure term. If the distance between fluid and boundary particles becomes smaller than $2h$, the density, pressure, and repulsive force created on the boundary particles increase, forming a repulsive mechanism (Gesteira et al. 2008).

2.1.6.3. Repulsive force method

The fundamental concept of the repulsive force model is to place boundary particles at the boundary zone, where they apply forces to the fluid particles inside. Monaghan initially proposed using a fixed set of particles at the boundary to prevent non-physical penetration of fluid particles through a repulsive force (Monaghan, 1994).

$$\begin{cases} K\left[\left(\frac{r_0}{x_i-x_j}\right)^{n_1} - \left(\frac{r_0}{x_i-x_j}\right)^{n_2}\right]\frac{(x_i-x_j)}{\left|(x_i-x_j)\right|^2} & \left|x_i - x_j\right| < 0 \\ 0 & \left|x_i - x_j\right| \geq 0 \end{cases} \tag{2.38}$$

where,

- n_1 and n_2 are often 12 and 4, respectively
- r_0 is the initial space between particles
- K is the square of the maximum velocity
- $(x_i - x_j)$ is the distance between particle i and j

If the value of K is too large, the strong force exerted by the boundary particles can cause calculation errors. It is important to note that if K is not sufficiently large, preventing fluid particles from penetrating the boundary becomes challenging. Additionally, this repulsive force model is highly sensitive and can easily cause disturbances during computations.

2.1.7. Time step calculation methods

The explicit time integration schemes must guarantee the CFL (Courant–Friedrichs–Lewy) condition to ensure the stability and convergence of the results. In a numerical simulation, the CFL condition expresses that the computational domain dependence in a numerical simulation must contain the physical domain dependence. This means that the maximum speed of numerical propagation must be lower than or equal to the maximum speed of physical propagation (Anderson, 2002). In SPH simulations, selection of the time step in SPH simulations is based on various criteria. According to the CFL condition, the time step should be proportional to the minimum spatial resolution, represented by the smallest smoothing length (h_i) in SPH applications (Liu and Liu, 2003).

$$\Delta t < \min\left(\frac{h_i}{c_i}\right) \tag{2.39}$$

where,

- c_i is the speed of sound (the physical one for compressible flow simulations, the artificial one for WCSPH simulations)
- h_i is the smoothing length

Monaghan (1992) proposed two expressions that consider the effects of viscous dissipation and external forces, and time step is Δt calculated as below:

$$\Delta t_{cv} = \min \left[\frac{h_i}{c_i + 0.6(\alpha_\Pi c_i + \beta_\Pi \max(\zeta_{ij})}\right], \ \Delta t_f = \min \left(\frac{h_i}{f_i}\right)^{0.5} \ , \Delta t = \min\left(\lambda_1 \Delta t_{cv} \, , \lambda_2 \Delta t_{cv}\right) \qquad (2.40)$$

where,

- f_i is acceleration term
- ζ_{ij} is obtained from artificial viscous term $\frac{h_{ij} \vec{v}_{ij} . x_{ij}}{|x_{ij}|^2 + \varphi^2}$
- $\lambda_1 = 0.4$ and $\lambda_2 = 0.25$

Morris et al. (1997) provided a method for determining the time step in the context of viscous diffusion.

$$\Delta t = 0.125 \left(\frac{{h_i}^2}{\nu}\right) \qquad (2.41)$$

where,

- ν is the kinematic viscosity $\left(\frac{m^2}{s}\right)$

Formulation used in the present method to calculate the time step takes into account the fact that the coefficient 0.125 in eq. (2.41) appears to be too restrictive and can be raised to 0.5, while the real propagation speed in the convection of a (weakly) compressible fluid is $|\vec{v}| \pm c$; the resulting constraint on the time step is:

$$\Delta t = \min \left[\frac{CFL.h_i}{|\overline{v}| \pm c_i}, \frac{1}{2} \frac{CFL.{h_i}^2}{v_i}\right] \qquad (2.42)$$

As a consequence, the adopted Courant condition is $\mathrm{CFL} = \frac{(|\vec{v}|+c)\Delta t}{h} < 1$

2.1.8. Temporal integration methods

Explicit methods are conditionally stable and require small time steps to ensure stability. They are often easier to implement, require less memory, and have a lower computational cost per time interval. Conversely, implicit methods are unconditionally stable, allowing for larger time steps while maintaining stability. However, they are more computationally expensive because solving systems of equations is an integral part of each step (Lee et al., 2024). The SPH method is an explicit method that can be implemented using algorithm time stepping methods such as Runge-kutta, Leap-Frog algorithm, Verlet algorithm, Beeman algorithm and prediction-corrector scheme. In the following section, the prediction-corrector, Leapfrog and Verlet approaches are presented.

2.1.8.1. Prediction-Corrector scheme

In 1989, Monaghan presented the prediction-corrector scheme (reversible scheme).

$$\vec{v}_i^{n+1} = \vec{v}_i^n + \vec{a}_i(\rho^n, p^n, \vec{x}^n)\Delta t \tag{2.43}$$

$$\vec{x}_i^{n+\frac{1}{2}} = \vec{x}_i^n + \vec{v}_i^{n+1}\frac{\Delta t}{2} \tag{2.44}$$

$$\rho_i^{n+1} = \rho_i^n + \dot{\rho}_i\left(\vec{v}^{n+1}, \vec{x}^{n+\frac{1}{2}}\right)\Delta t \tag{2.45}$$

$$\vec{x}_i^{n+1} = \vec{x}_i^{n+\frac{1}{2}} + \vec{v}_i^{n+1}.\frac{\Delta t}{2} \tag{2.46}$$

$\vec{a}_i$ is the acceleration to represent the force terms

2.1.8.2. Leap-Frog algorithm

The Leapfrog method typically includes the velocity update at half-steps and position update at full steps (Dutra Fraga Filho, 2019):

$$\vec{v}(t + \tfrac{1}{2}\Delta t) = \vec{v}(t - \tfrac{1}{2}\Delta t) + \frac{D\vec{v}}{Dt}(\Delta t) \tag{2.47}$$

Update of position at time $t + \Delta t$:

$$X(t + \Delta t) = X(t) + \Delta t \vec{v}(t + \frac{1}{2}\Delta t) \tag{2.48}$$

Velocity update at time *t* by averaging the velocities at the half-steps:

$$\vec{v}(t) = \frac{1}{2}\left[\vec{v}(t + \frac{1}{2}\Delta t) + \vec{v}(t - \frac{1}{2}\Delta t)\right] \tag{2.49}$$

Initial velocity update (if starting from *t=0*)

$$\vec{v}(\frac{1}{2}\Delta t) = \vec{v}(0) + \frac{\Delta t}{2}\frac{D\vec{v}}{Dt}\Big|_{t=0} \tag{2.50}$$

2.1.8.3. Verlet algorithm

The Verlet (1967) algorithm is a second-order time integration method commonly employed in Smoothed Particle Hydrodynamics (SPH) simulation:

$$\vec{v}_i^{n+1} = \vec{v}_i^n + \frac{1}{2}\left(\vec{a}_i^{\,n} + \vec{a}_i^{\,n+1}\right)\Delta t \tag{2.51}$$

$$\vec{x}_i^{n+1} = \vec{x}_i^n + \vec{v}_i^n \Delta t + \frac{1}{2}\vec{a}_i^{\,n}\Delta t^2 \tag{2.52}$$

$$\rho_i^{n+1} = \rho_i^n + \dot{\rho}_i^{\,n}\Delta t \tag{2.53}$$

$\dot{\rho}_i$ represents the time derivative of density

2.1.8.4. Runge-Kutta scheme (2nd Order)

The second-order Runge-Kutta scheme (Liu and Liu, 2003), often known as the midpoint approach, is commonly used in SPH to enhance accuracy over the first-order Euler method. First, velocity, position and density are evaluated at half of the time step:

$$\vec{v}_i^{\,n+\frac{1}{2}} = \vec{v}_i^n + \vec{a}_i^n \frac{\Delta t}{2} \tag{2.54}$$

$$\vec{x}_i^{\,n+\frac{1}{2}} = \vec{x}_i^n + \vec{v}_i^n \frac{\Delta t}{2} \tag{2.55}$$

$$\rho_i^{n+\frac{1}{2}} = \rho_i^n + \dot{\rho}_i{}^n \frac{\Delta t}{2} \tag{2.56}$$

then, the velocity, position, and density are updated for the full-time step (t + Δt) using the forces and derivatives calculated at the half-step state:

$$\vec{v}_i^{n+1} = \vec{v}_i^n + \vec{a}_i^{n+\frac{1}{2}} \Delta t \tag{2.57}$$

$$\vec{x}_i^{n+1} = \vec{x}_i^n + \vec{v}_i^{n+\frac{1}{2}} \Delta t \tag{2.58}$$

$$\rho_i^{n+1} = \rho_i^n + \dot{\rho}_i{}^{n+\frac{1}{2}} \Delta t \tag{2.59}$$

2.2. Non-Newtonian fluids

To describe non-Newtonian fluids, it is essential to first grasp the concept of Newtonian behaviour, which is characterized by a constant shear viscosity (under constant temperature and pressure). In Newtonian fluids:

- Viscosity remains constant regardless of the shear rate.
- Viscosity does not change over time.

For a simple planar shear flow, this reflects in Newton's rheological law:

$$\tau_{xy} = \mu \frac{\partial u}{\partial y} \tag{2.60}$$

where,

- τ_{xy} is the shear stress (Pa)
- u is the x-component of velocity
- μ is the dynamic viscosity (Pa.s)
- $\frac{\partial u}{\partial y}$ or $\dot{\gamma}$ is the velocity gradient perpendicular to the plane of shear or the shear rate (s^{-1})

Newton’s law can be generalized to any 3D flow by extending (2.54) to build up a relation between the deviatoric stress tensor $\bar{\bar{\tau}}$ and the velocity gradient tensor $\vec{\nabla}\vec{v}$. For an incompressible fluid, Newton’s law then reads as:

$$\tau_{xy} = \mu\left(\vec{\nabla}\vec{v} + \vec{\nabla}\vec{v}^{T}\right) \tag{2.61}$$

where the apex T indicates a transposed tensor.

If a fluid shows deviations from these behaviours, it is classified as a non-Newtonian fluid (see Figure 2.11).

In other words, for Newtonian fluids the correlation between shear stress and shear rate is linear at a given temperature, characterized by a constant slope that reflects the fluid viscosity (Capone, 2009). Conversely, a non-Newtonian fluid demonstrates a nonlinear correlation between shear stress and shear rate, wherein viscosity varies with flow properties, including shear rate, flow history, internal structure of the material, etc.

Non-Newtonian fluids are categorized into three classifications:

i. Fluids whose shear rate depends only on the current shear stress. These materials are known as generalized Newtonian fluids or time-independent fluids.

ii. Fluids for which the relationship between shear stress and shear rate depends on the duration of shearing as well as the fluid's kinematic history. These materials are known as time-dependent fluids.

iii. Fluids that possess the characteristics of both ideal fluids and elastic solids. They exhibit partial recovery to the initial state following applied deformation. These materials are known as viscoelastic (Chhabra and Richardson, 2004),

Only a few well-known models for describing non-Newtonian fluid behaviour, both without and with yield stress, are discussed here.

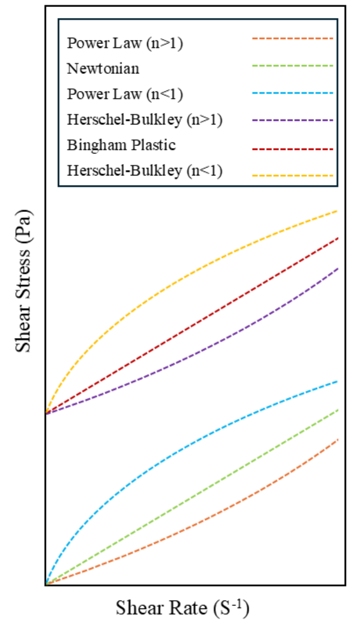

Figure 2. 11. Classification of fluids with shear stress as a function of shear rate

2.2.1. Bingham plastic model

A fluid that exhibits linear behaviour after exceeding yield stress is referred to as a Bingham plastic fluid. One of the simplest viscoplastic models is the Bingham plastic model, and it is commonly used to represent muddy flows in coastal engineering (Chhabra and Richardson, 2004). It is defined as follows:

$$\begin{cases} \tau = \mu_{\text{eff}}\gamma^{\cdot} + \tau_y & if \quad \tau \geq \tau_y \\ \gamma^{\cdot} = 0 & if \quad \tau < \tau_y \end{cases} \tag{2.62}$$

where,

- μ_{eff} is the apparent viscosity (Pa.s)
- $\gamma^{\cdot}$ is the velocity gradient perpendicular to the plane of shear or the shear rate (s^{-1})
- τ_y is the yield stress (Pa)

2.2.2. Herschel-Bulkley model

The Herschel-Bulkley model is a widely used and versatile rheological model that describes the flow behaviour of non-Newtonian fluids exhibiting yield stress. It extends the Power-law model by incorporating the concept of yield stress, accounting for materials that require a minimum stress to start flowing, followed by shear-thinning or shear-thickening behaviour. This model combines features of both the Bingham plastic and Power-law models, making it applicable to a wide range of complex fluids, including pastes, gels, slurries, and other materials that exhibit non-Newtonian behaviour (Kim, 2002). The formulation of this model is defined as follows:

$$\begin{cases} \tau = \mu_{eff}(\gamma^{\cdot})^{n} + \tau_y & if \quad \tau \geq \tau_y \\ \gamma^{\cdot} = 0 & if \quad \tau < \tau_y \end{cases}$$

and,

$$\mu_{eff} = \begin{cases} \frac{\tau_y}{\gamma^{\cdot}} + K\gamma^{\cdot\, n-1} & if \quad \gamma^{\cdot} > \overline{\gamma^{\cdot}} \\ \frac{\tau_y}{\overline{\gamma^{\cdot}}} + K\overline{\gamma^{\cdot}}^{\,n-1} & if \quad \gamma^{\cdot} \leq \overline{\gamma^{\cdot}} \end{cases} \tag{2.63}$$

where,

- μ_{eff} is the apparent viscosity (Pa.s)
- k is the flow consistency index (Pa.s^n)
- $\gamma^{\cdot}$ is the velocity gradient perpendicular to the plane of shear or the shear rate (s^{-1})
- τ_y is the yield stress (Pa)
- $\overline{\gamma^{\cdot}}$ is the cut-off shear rate (s^{-1})

2.2.3. Power-Law model

The power law model, also known as the Ostwald-de Waele model (1929), is a rheological model widely used to describe the non-Newtonian flow behaviour of various materials. The power-law model applicability for various natural phenomena, including landslides and estuarine mudflows, is well-documented. In other words, as a simple and powerful tool for describing a wide range of complex rheological behaviours, the Power law model identifies non-Newtonian fluids through exponential relationship between shear stress and shear rate (Macosko, 1994). The power law model is mathematically represented as:

$$\tau = \mu_{eff} \times \left(\frac{\partial u}{\partial y}\right) = k\left(\left\|\vec{\nabla}\vec{v}_i + \vec{\nabla}\vec{v}_i^{T}\right\|\right)^{n} \quad ,\text{and} \quad \mu_{eff} = K\left\|\vec{\nabla}\vec{v}_i + \vec{\nabla}\vec{v}_i^{T}\right\|^{n-1} \tag{2.64}$$

where,

- μ_{eff} is the apparent viscosity (Pa.s)
- k is the flow consistency index (Pa.s^n)
- $\vec{\nabla}\vec{v}_i$ is the velocity gradient or shear rate (s^{-1})
- n is the flow behaviour index or rheological index (dimensionless) indicating whether the fluid is shear-thinning (pseudoplasticity) (n<1) or shear-thickening (Dilatant) (n>1) or Newtonian (n=1) (see Figure 1.12).

As mentioned before, viscous stresses in the power law model can be computed from the direct estimation of the velocity gradient tensor equation (Eq. 2.58).

The implementation of the power-law model in SPH is rather straightforward, and can be obtained through a particle approximation of eq. (2.54):

$$\left\langle \vec{\nabla} \cdot \left(\mu \vec{\nabla} \vec{v} \right) \right\rangle = -\sum_j \frac{m_j}{\rho_j} (\mu_i + \mu_i) \frac{\vec{v}_{ij} \cdot \vec{r}_{ij}}{\left| \vec{r}_{ij} \right|^2 + \varepsilon h^2} \vec{\nabla} W(x_i - x_j, h) \tag{2.65}$$

In the present work, shear-thinning fluids with rheological indices ranging from 0.1 to 0.4 are considered. The Power Law model is explicitly implemented within the SPH framework to calculate the viscous stress. This implementation allows for accurate representation of non-Newtonian behavior by directly incorporating the flow behavior index n and the consistency index k into the particle-based viscosity calculations, enabling the simulation of complex shear-dependent viscosity effects in the fluid.

2.2.4. Non-Newtonian model assumptions

In this research, the non-Newtonian fluid is assumed to be a homogeneous continuum governed by a generalized power-law rheology. This macroscopic approach is widely adopted for simulating hyper-concentrated flows (Coussot, 2017). The continuum assumption is particularly appropriate for highly concentrated mudflows and fine-grained mixtures where the solid fraction is uniformly distributed, and particle–particle interactions can be effectively represented through an apparent viscosity (Ancey, 2007).

However, extending this modelling approach to real-world mudflows requires careful consideration. Natural debris flows are inherently multiphase systems characterized by a broad grain-size distribution, including coarse grains and clasts (Iverson, 1997). Consequently, complex fluid–granular interactions cannot be fully resolved by a single-phase SPH model. Processes such as phase segregation (inverse grading), granular collisions, and the evolution of dry granular fronts are often simplified or neglected in single-phase continuum formulations (Savage and Hutter, 1989). Additionally, the assumption of hydrostatic pressure distribution and laminar generalized-Newtonian behaviour limits the applicability of the model to flow regimes in which turbulence, inertial granular stresses, and non-hydrostatic effects are negligible compared to viscous forces (Wang et al., 2016).

2.3. Eulerian Depth Averaged Model (EDAM)

Neglecting the surface tension and the flow resistance due to the sidewalls, the dimensional depth-averaged momentum and mass conservation equations are (Hogg and Pritchard, 2004):

$$\frac{\partial Vh}{\partial t} + \beta \frac{\partial hV^2}{\partial x} + gh \frac{\partial h}{\partial x} - ghsin\,\vartheta + \frac{\tau_b}{\rho} = 0 \tag{2.66}$$

$$\frac{\partial h}{\partial t} + \frac{\partial (Vh)}{\partial x} = 0 \tag{2.67}$$

where,

- t is time
- x is the streamwise coordinate
- g is the gravitational acceleration
- ϑ is the bed slope
- V is the depth-averaged velocity
- h is the flow depth
- β is the momentum flux factor
- τ_b is the bottom shear stress

For a power-law fluid and laminar flow conditions, the momentum flux factor and the bottom shear stress are (Ng and Mei, 1994):

$$\beta = 2\frac{2n+1}{3n+2} \quad , \quad \tau_b = \kappa\left(\frac{2n+1}{n}\frac{V}{h}\right)^n \tag{2.68}$$

The EDAM numerical solution of the dam break problems has been found by solving (2.66)-(2.68) through a Finite Volume scheme which is second order accurate in both space and time. The Harten-Lax-Van Leer (HLL) scheme (Harten and Lax, 1983) has been employed for evaluating the numerical fluxes and the values of the conserved variables at the interfaces are estimated using a piecewise linear reconstruction scheme with a non-linear min-mod limiter (LeVeque, 2002). The time integration is performed through a second order two-step Runge–Kutta scheme (Gottlieb and Shu, 1998). Additional details about the numerical scheme can be found in Campomaggiore et al. (2016).

2.4. Eulerian Depth Resolved Model (EDRM)

In this work we use a VOF solver interFoam from the open-source CFD toolbox OpenFOAM (OpenCFD, 2016) to solve the EDRM.

The governing equations are the 2D Navier-Stokes equations for incompressible fluid which in their Eulerian formulation read:

$$\nabla \cdot \mathrm{u} = 0 \tag{2.69}$$

$$\rho \frac{\partial \mathrm{u}}{\partial \mathrm{t}} + \rho \, \nabla \cdot (\mathrm{u} \otimes \mathrm{u}) + \nabla \mathrm{p} + \rho \, \mathrm{g} \, \nabla \mathrm{z} = \nabla \cdot \mathrm{T} \tag{2.70}$$

where,

- u is velocity
- p is pressure
- T is the extra-stress tensor

which for power law model is:

$$T = \kappa \, \dot{\gamma}^{n-1} D \tag{2.71}$$

In which $\mathrm{D} = [\nabla \mathrm{u} + (\nabla \mathrm{u})^{\mathrm{T}}]$ and $\dot{\gamma}$ is the square root of one half of the second invariant of D.

The free surface problem has been handled using the VOF method (Berberović et al., 2009) and therefore solving an advection equation for the volume fraction of liquid (a) over the whole computational domain:

$$\frac{\partial \alpha}{\partial \mathrm{t}} + \nabla \cdot (\alpha \, \mathrm{u}) + \nabla \cdot [\alpha(1 - \alpha) \, \mathrm{u_r}] = 0 \tag{2.72}$$

where $\mathrm{u_r}$ denotes the liquid-air relative velocity. The last term allows the compression of the interface to a sharper region (Berberović et al., 2009).

3. Experimental campaign

An experimental campaign, carried out at Zaragoza University (Spain), has been conducted to investigate the behaviour of a dam-break flow of non-Newtonian fluids. This chapter includes descriptions of the experimental setup, fluid preparation (Carbopol-940 solution), and the usage of measurement techniques such as an RGB-D sensor for free surface detection and Particle Image Velocimetry (PIV) for free surface velocity measurements. The experimental data obtained provide information on the characteristics of wave propagation and impact and can be used to verify the performance of numerical models.

3.1. Experimental setup

The experimental setup consisted of a 2.25 m × 0.24 m × 0.30 m flume mounted on an aluminium structure which was capable of adjusting the longitudinal slope up to 15 degrees. At the upstream gate, an independent reservoir (75 cm × 24 cm) was placed. An aluminium gate with 2mm thickness was installed in front of the downstream reservoir, which could be opened by a pneumatical system. The reservoir was filled with a shear-thinning fluid with a known rheology. The effective reservoir length could be managed using a movable plate as same as flume width. The flume's downstream could be configured as either open-end or closed-end. Tests were conducted using two flume configurations: horizontal (*0.0^0)* and inclined (*4.65^0*) (see Figure 3.1).

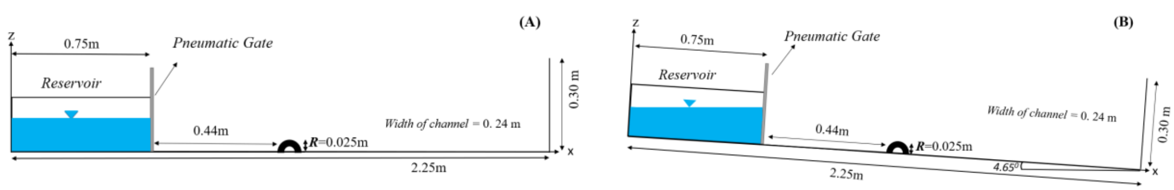

Figure 3. 1. Sketch of the experimental flume for non-Newtonian fluid tests: horizontal (A) and inclined (B)

The opening time of the gate was calibrated by varying the pressure in the pneumatic gate, with an approximate gate speed of 0.78 meters per second at 7.8 bar pressure in the pneumatic circuit (Figure 3.2). All experiments were conducted at 7.8 bar pressure, which means the gate removal speed was 0.78 m/s. The upstream reservoir and downstream flume were made of rigid plexiglass. The semi-cylindrical obstacle was made of stiff PVC that completely sealed on the bottom and side walls of flume. The bottom of the flume and the obstacle were covered with an adhesive PVC black film. 6 spatial reference points were marked on the downstream flume within the near region of both the gate and the obstacle. Once the gate opens, the viscoelastic fluid spreads across the flume and generates a highly transient shock wave. The region of interest was illuminated directly from above using a 100 W LED white-light source and recorded through multiple imaging techniques, including an RGB-D sensor, two CMOS cameras, and a lateral CMOS camera (Figure 3.3).

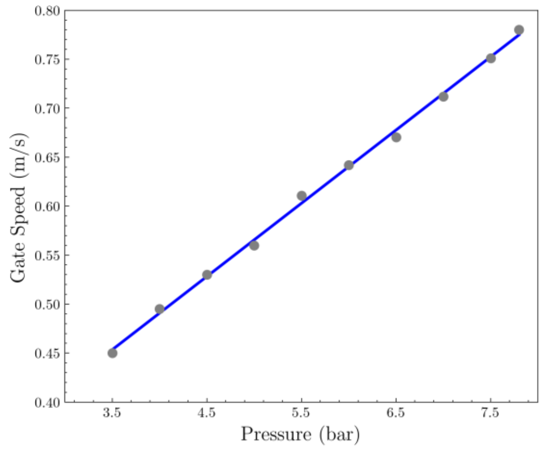

Figure 3. 2. Gate speed vs. Pressure

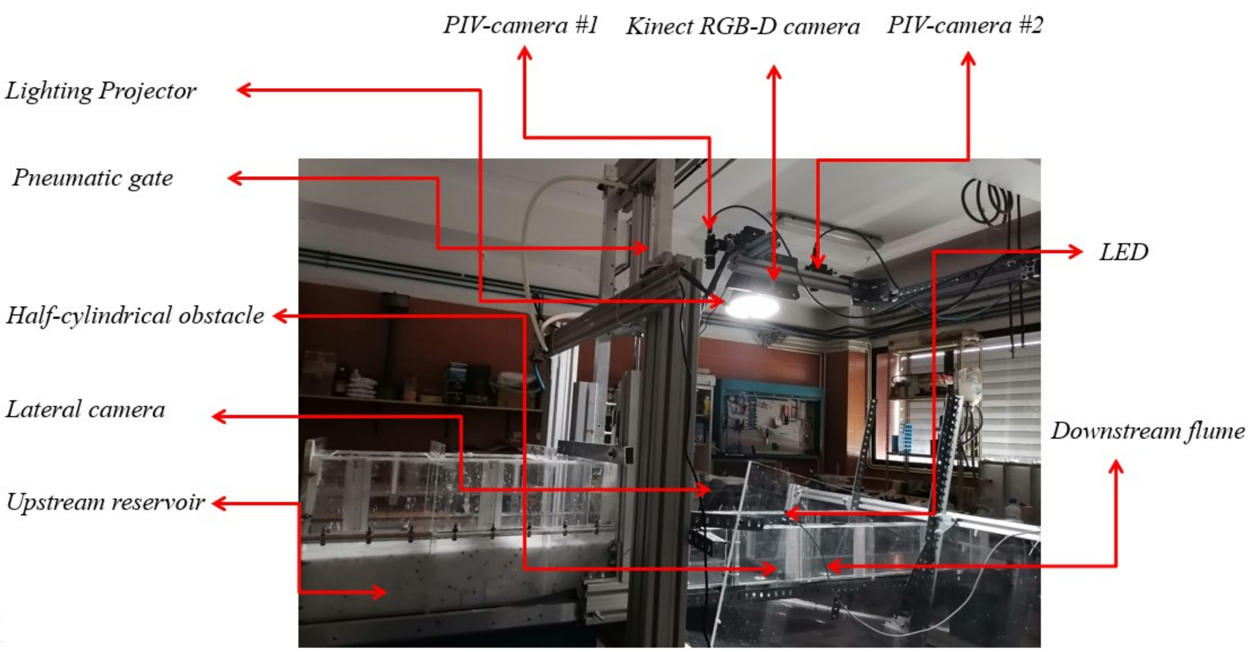

Figure 3. 3. The global view of the experimental setup

3.2. Fluid preparation

To conduct dam-break experiments in the laboratory with non-Newtonian fluid, it was necessary to select a fluid that could be easily prepared in the lab and effectively demonstrate shear-thinning behaviour. For this purpose, a mixture of Carbopol-940 solution in demineralized water was chosen. Initially, the Carbopol-940 powder was uniformly mixed with four-fifths of the total water mass. To achieve an opaque white fluid, 0.1% *w/w* of Titanium dioxide (TiO_2) powder was added, and the mixture was then allowed to rest for one day. To neutralize the prepared fluid, a 0.5% w/w sodium hydroxide (NaOH) solution was gradually added until the pH was adjusted to the range of 7.1 to 7.4. To facilitate tracking, dark-grey LDPE particles with an approximate diameter and density of 3 mm and 920−960 kg/m^3 were added (200 particles/kg). Finally, the remaining one-fifth of the water mass was added, and the solution was mixed homogeneously. The resulting fluid was an opaque white gel with non-Newtonian properties, exhibiting viscoplastic shear-thinning characteristics. The flow curve was characterized using a rotational viscometer (Haake Rotovisco RV20-M5) equipped with the MV2 Couette cell (Figure 3.4).

Figure 3. 4. mixture of the viscoplastic shear-thinning fluid (left), LDPE dark-grey particles used as tracers (center), and the Haake Rotovisco RV20-M5 rotational viscometer (right)

To measure viscosity, fluid samples were prepared with varying Carbopol-940 concentrations. Each sample was tested twice, with consistent repeatability, and the data were then averaged. The flow curves were well fitted to the Herschel-Bulkley (H-B) model, expressed as:

$$\tau = \tau_y + \mu \dot{\gamma}^{m} \tag{3.1}$$

where τ represents shear stress (Pa), $\dot{\gamma}$ is shear rate (s^{-1}), τ_y is yield strength (Pa), μ is the consistency coefficient (Pa.s^m), and *m* is the behaviour index. Figure 3.5 presents the τ vs. $\dot{\gamma}$ viscometer data and the fitting curves based on the Herschel-Bulkley model. The figure illustrates two rheological behaviours: the first corresponds to the original concentration, and the second one is obtained by decreasing the Carbopol-940 concentration by 10% through the addition of demineralized water. These results indicate a decrease in shear-thinning behaviour as the Carbopol concentration decreases, aligning with previously published rheological parameters for Carbopol solutions (COChARD, 2007; Divoux et al., 2010; Luu et al., 2015)

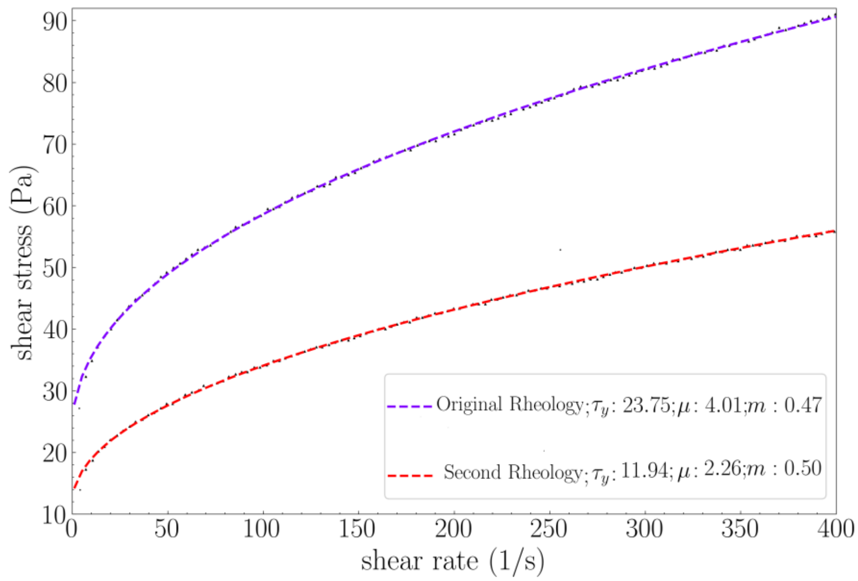

Figure 3. 5. Fitting curves for Carbopol-940 solution at two concentrations: Original and Second

3.3. Free surface measuring with RGB-D sensor

To measure the free surface profile in dam-break experiments, an imaging system called the RGB-D device (Kinect v1) is developed by Microsoft in 2010. The Kinect v1 is designed to capture both high-definition RGB images and depth (D) information at a 30 Hz acquisition rate, simultaneously. The RGB camera provides 640×480-pixel resolution at 8 bits per pixel (24-bit color depth), while the depth sensor, based on structured light technology, offers a 640×480-pixel resolution with 16-bit depth information. This configuration allows the Kinect v1 to create a 3D representation of the environment, making it suitable for applications such as motion tracking, gesture recognition, and spatial mapping [Kinect basis].

Titanium dioxide (TiO_2) powder was added to the non-Newtonian Carbopol-940 solution, allowing for better surface capture by the Kinect (Martínez). It was necessary to install the Kinect perpendicular to the flume at a distance of approximately 1 meter. This position enabled coverage of 0.8 meters of the flume length, which was the area of interest for the open-end, closed-end and obstacle tests. The depth image provided by the NIR sensor was reassembled to reconstruct a 3D point cloud of the transient flow free surface. Figure 3.6 shows the Kinect-v1 device, and the flowchart needed to obtain the structured grid interpolation.

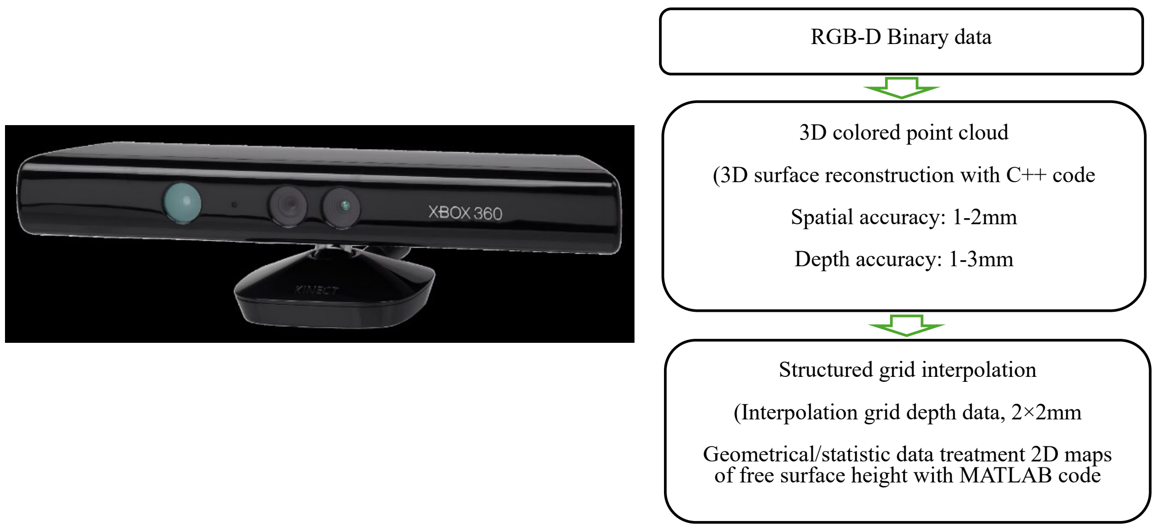

Figure 3. 6. RGB-D (Kinect v1) device (left), and schematic flowchart for acquiring free surface data

Figure 3.7 presents the raw RGB image and free surface which is reconstructed from point cloud in the experiment conducted with the obstacle, after opening the gate at the same time.

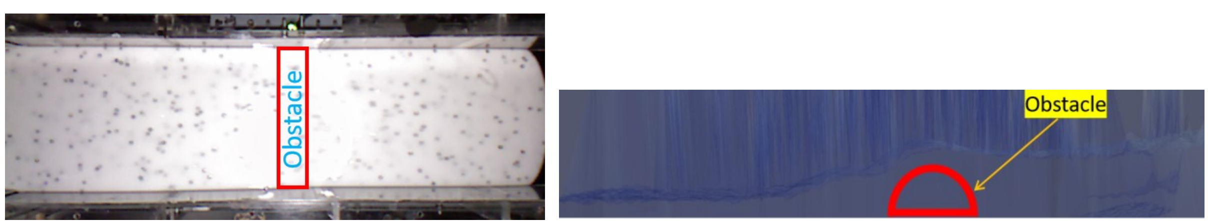

Figure 3. 7. Raw RGB image (right) and the free surface, which is reconstructed from the point cloud in the experiment conducted with the obstacle (left)

3.4. Velocity measurement with PIV camera

Particle Image Velocimetry (PIV) technique was invented as a useful tool in experimental fluid mechanics for measuring velocity fields. This technique was first applied by Adrian (1984), and PIV method has seen significant advancements in both spatial and temporal resolution, as well as improvements in accuracy (e.g., Westerweel, 1997; Hart, 2000).

In the experiments, the region of interest was recorded using two CMOS cameras (Triton 016S-CC 1.6Mpx, Lucid, 2019) installed 0.4 meters apart on a horizontal bar. Both cameras were equipped with 8 mm fixed-focal-length lenses and mounted approximately 1 meter above the flume, perpendicularly. To ensure high-quality PIV data, specific precautions were taken regarding illumination and exposure control. The region was illuminated using a LED (100 W) white-light source. A matte screen was positioned in front of the light to avoid specular reflections on the free surface, which could otherwise interfere with the particle tracking. This lighting setup was also fundamental to generate a homogeneous background on the opaque white fluid (enhanced by TiO_2), ensuring high contrast for the dark-grey LDPE tracer particles. The cameras provided high-resolution images (1440 px×1080 px) with an acquisition rate of 70 fps and an exposure time of 2.5 ms. Synchronization between the cameras and the free surface sensor (Kinect) was achieved using a green LED diode triggered by the gate opening (see figure 3.3).

Two different slope angles of the flume were used during the experiments: zero and 4.65 degrees. However, before data collection, the cameras were calibrated to establish the relationship between the distance above the flume and the corresponding millimetres per pixel (see Figure3.8).

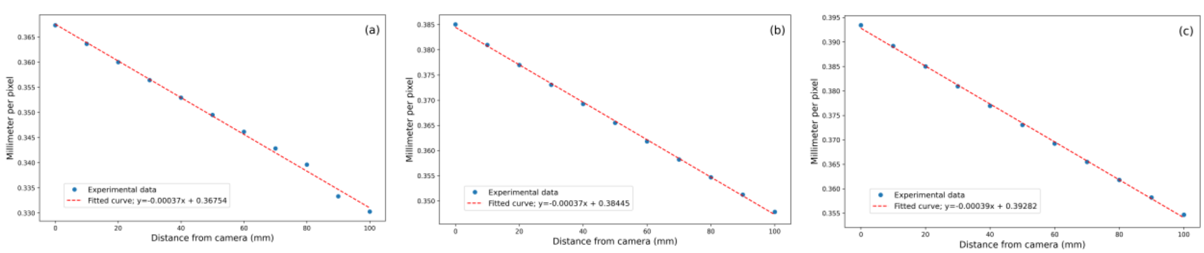

Figure 3. 8. Camera calibration: mm/px vs. distance; (a) zero degrees (Camera 1 & 2), (b) 4.65 degrees (Camera 1), (c) 4.65 degrees (Camera 2)

For post-processing the CMOS images, the MATLAB Toolbox (PIVlab) was used. The raw RGB images were first converted to grayscale and then transformed into inverted-intensity matrices, where the tracer particles were highlighted as light points against a black background. Using the toolbox, displacement vectors were extracted, with missing vectors filled in through interpolation. Additionally, a filtering process was applied by setting a low correlation coefficient threshold to improve the accuracy of the measurements (Figure 3.9).

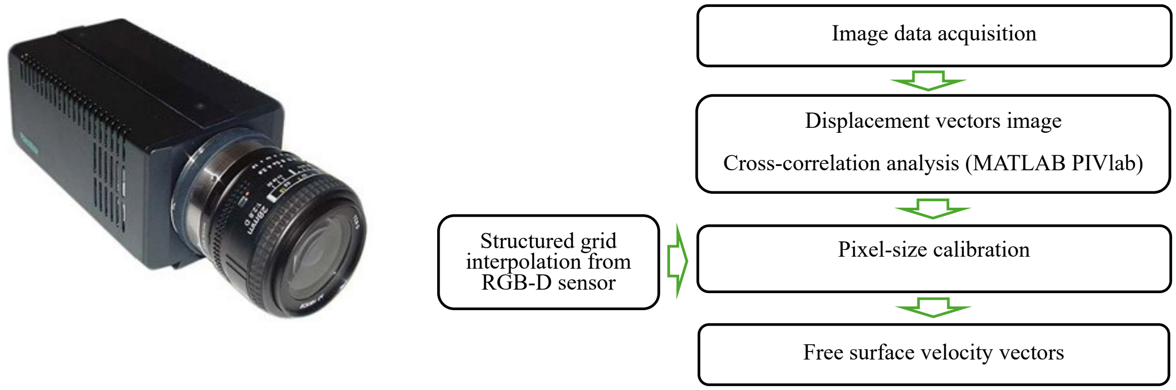

Figure 3. 9. CMOS cameras (left), and schematic flowchart for the free surface velocity measurement (right)

4. Results and Discussions

4.1. Model Validation

Before applying the particle-based smoothed particle hydrodynamics (SPH), it is crucial to conduct a comprehensive validation of the code. This chapter focuses on the validation PVSPH code for Newtonian and non-Newtonian fluid flows using literature experimental data and analytical solutions, across a wide range of test scenarios, including dry-bed and wet-bed dam-break flows with different bed configurations, as well as Poiseuille flows.

Model validation ensures that the model's parameters, coefficients and assumptions align with physical reality and can accurately simulate observed phenomena, so this process is important for confirming that the PVSPH code produces stable and reliable results under various conditions.

4.1.1. Water dam-break on dry-bed

The first test considers water dam-break on dry-bed conditions. For this purpose, the benchmark case no. 5 by the SPH European Research Interest Community (SPHERIC) (Janosi et al., 2004) is selected. A schematic scheme of the channel is provided in Figure 4.1. In this experiment, the flow depth upstream is set 0.15 m, and it has been assumed that the gate is removed at a constant speed of 1.5 m/s (Khayyer and Gotoh, 2010). A series of simulations were conducted to achieve optimal parameters for reliable and stable results, as presented in Table 4.1. Various parameters, including particle diameter, smoothing velocity coefficients, time integration scheme and boundary condition were examined to understand their effects on the model's accuracy.

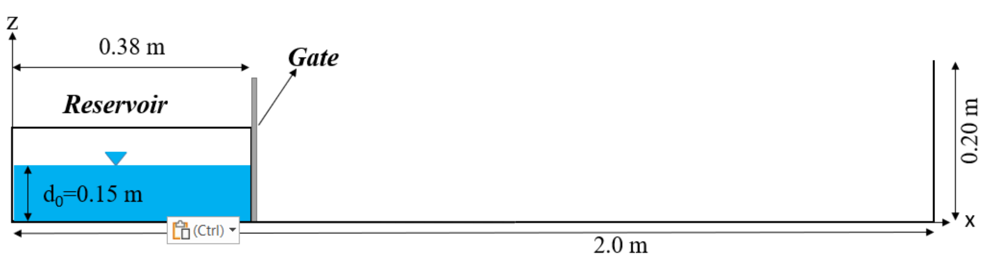

Figure 4. 1. Schematic geometric dimensions of dry-bed dam-break experiment

Table 4. 1. List of tests conducted in the dry-bed dam-break simulation

Test no.	Diameter	Smoothing Velocity	CFL	Time Integration Scheme	Boundary condition
1	0.02	0.1	0.6	Reversible	Slip
2	0.02	0.02	0.6	Reversible	Slip
3	0.02	0.015	0.6	Gallati	Slip
4	0.02	0.015	0.6	Gallati	No-Slip
5	0.02	0.015	0.6	Reversible	No-Slip
6	0.02	0.015	0.6	Reversible	Slip
7	0.02	0.01	0.6	Reversible	Slip
8	0.02	0	0.6	Reversible	Slip
9	0.01	0.015	0.6	Reversible	Slip
10	0.005	0.02	0.6	Reversible	Slip
11	0.005	0.02	0.5	Reversible	Slip
12	0.005	0.02	0.5	Gallati	Slip

After performing all the simulations listed in the table above, test case no. 11 was chosen as the optimal option based on the results. The acceptable outcome was achieved with the following parameters:

- CFL=0.5;
- Time Integration Scheme= Reversible;
- Boundary condition= Slip;

In Figure 4.2, and 4.3, the sequences of snapshots by PVSPH and benchmark SPHERIC test, at different times are presented. As shown in Figure 4.2, when fluid is released into a dry channel, the front characteristic shape develops rapidly, and the acceleration terminates within 0.3–0.5 seconds. Moreover, there are no visible signs of strong turbulence. However, in terms of the high Reynolds number (Re=3-5+E04) within the range of 0.1 to 0.5 seconds, a turbulent boundary layer is likely to form near the walls.

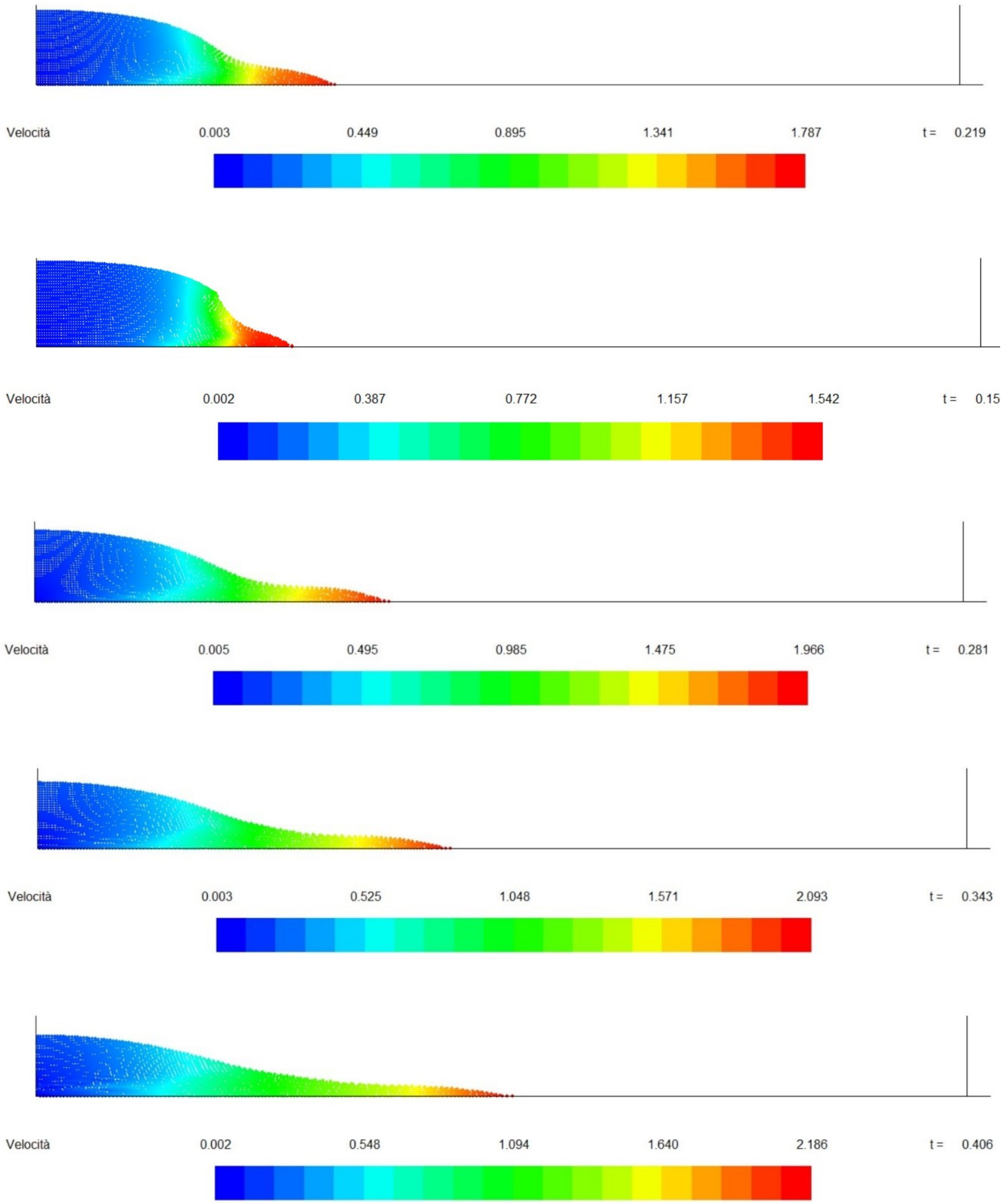

Figure 4. 2. Sequences of snapshots after releasing water from the gate in dam-break simulation by PVSPH for dry-bed, at different times

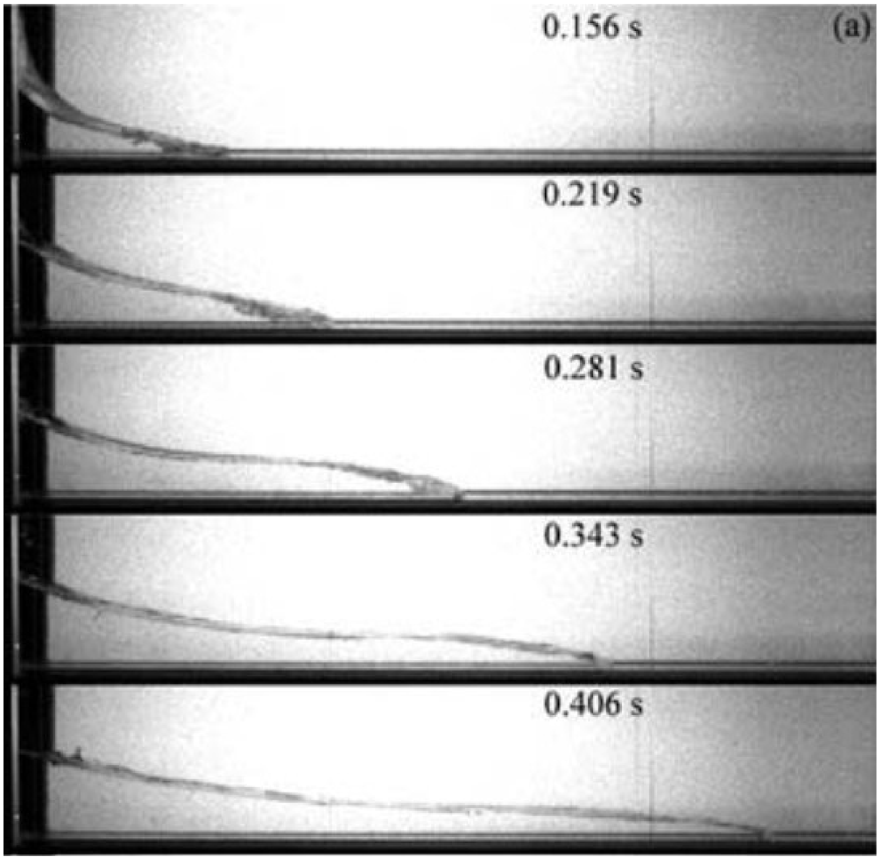

Figure 4. 3. Sequences of snapshots after releasing water from the gate in dam-break experiment for dry-bed, at different times (Janosi et al. 2004)

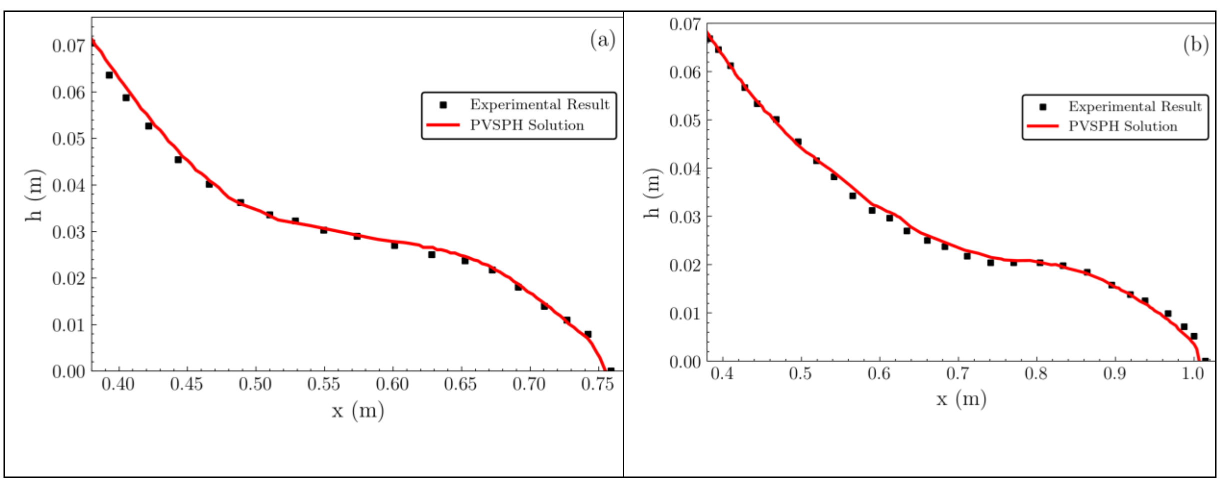

Figure 4. 4. Comparison between measured and simulated water surface profiles for dry-bed condition at t=0.281s (a) and t=0.406s (b)

Figure 4.4. shows the comparison between the PVSPH solution and experimental results at two different times, t=0.281s and t=0.406s, in dry-bed condition. The PVSPH results closely match the experimental

observations. In terms of RMSE, figure (a) and figure (b) have values of 1.71% and 1.26% (expressed as a percentage of the maximum water depth, respectively, which are very low. This indicates that the model is able to simulate the wave propagation with high accuracy. The errors in results may arise due to the presence of a very thin water layer near the bed downstream in the experiment, because it is very difficult to achieve a completely dry-bed in a laboratory.

4.1.2. Water dam-break on wet bottom

To validate the PVSPH code for wet-bed conditions, it is essential to repeat comparison by the SPHERIC benchmark tests case no.5. For the wet-bed tests, two different initial water depths at the downstream of the gate were considered: 18 mm and 38 mm.

4.1.2.1. Wet-bed Dam-break Case (d=0.018m)

The schematic setup of the channel is provided in Figure 4.5. For the wet-bed experiments, similar to the dry-bed test configuration, the flow depth upstream is 0.15 m, and the gate is removed at the same constant speed (1.5 m/s). However, a thin layer of water at downstream is present (d=0.018).

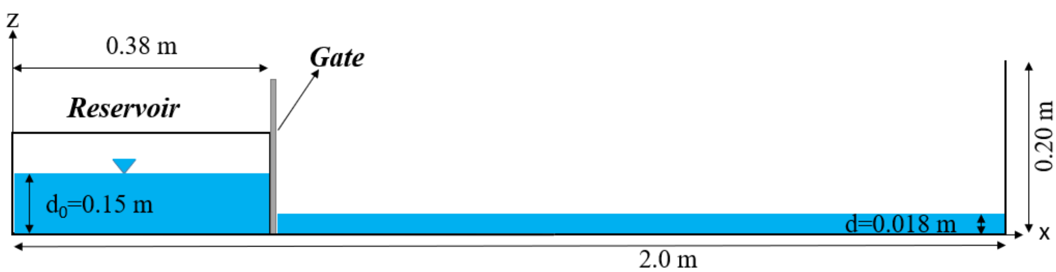

Figure 4. 5. Experimental setup of the SPHERIC reference dam-break case, wet-bed (d=0.018m)

To assess the optimal parameters, some tests were conducted (Table 4.2). Parameters such as particle diameter, smoothing velocity coefficients, time integration scheme, and boundary conditions, and finally the results of test case no. 11 were found to be satisfactory.

Table 4. 2. List of first trial tests conducted in wet-bed dam-break simulation (d=0.018m)

Test no.	Diameter	Smoothing Velocity	CFL	Time Integration Scheme	Boundary condition
1	0.02	0.015	0.6	Gallati	No-Slip
2	0.02	0.015	0.6	Gallati	Slip
3	0.005	0.10	0.6	Reversible	Slip

4	0.005	0.015	0.6	Gallati	Slip
5	0.005	0.015	0.6	Reversible	Slip
6	0.005	0.015	0.6	Reversible	Slip
7	0.005	0.015	0.6	XSPH	Slip
8	0.005	0.015	0.15	Reversible	Slip
9	0.005	0.015	0.15	Gallati	Slip
10	0.005	0.00	0.6	Reversible	Slip
11	0.005	0.015	0.6	Reversible	Slip

Then by keeping constant the slip boundary condition and at walls, and Reversible as a best time integration scheme, the second trial of tests were conducted (Table 4.3).

Table 4. 3. List of second trial tests conducted in wet-bed dam-break simulation (d=0.018m)

Test no.	Diameter	Smoothing Velocity	Artificial Viscosity	CFL	Modulus of elasticity	h/d
1	0.005	0.05	0	0.6	1.00E+06	1.5
2	0.004	0.1	0.01	0.6	1.00E+06	1.5
3	0.004	0.1	0	0.6	1.00E+06	1.5
4	0.003	0.055	0.01	0.5	1.00E+06	1.5
5	0.003	0.05	0.005	0.4	1.00E+06	1.5
6	0.003	0.05	0.0025	0.5	1.00E+06	1.5
7	0.003	0.05	0.0025	0.4	1.00E+06	1.5
8	0.003	0.03	0.005	0.5	3.60E+06	1.5
9	0.003	0.03	0.005	0.5	2.50E+06	1.7
10	0.003	0.03	0.005	0.5	2.50E+06	1.5
11	0.003	0.03	0.005	0.5	2.50E+06	1.3
12	0.003	0.03	0.005	0.5	1.00E+06	1.5
13	0.003	0.03	0.005	0.4	1.00E+06	1.5
14	0.003	0.03	0.004	0.5	1.00E+06	1.5
15	0.003	0.03	0.0025	0.5	1.00E+06	1.5
16	0.003	0.03	0.0025	0.4	1.00E+06	1.5
17	0.003	0.02	0.005	0.5	2.50E+06	1.5
18	0.003	0.02	0.005	0.5	1.00E+06	1.6
19	0.003	0.02	0.005	0.5	1.00E+06	1.5
20	0.003	0.02	0.005	0.5	3.60E+05	1.5
21	0.003	0.02	0.004	0.5	1.00E+06	1.5
22	0.003	0.015	0.005	0.5	1.00E+06	1.5
23	0.003	0.015	0.0025	0.5	1.00E+06	1.5
24	0.003	0.015	0.0025	0.4	1.00E+06	1.5

25	0.003	0.015	0	0.2	1.00E+06	1.5
26	0.002	0.05	0	0.3	1.00E+06	1.5
27	0.002	0.05	0	0.3	5.00E+05	1.5
28	0.002	0.03	0.005	0.5	2.50E+06	1.6
29	0.002	0.02	0.005	0.5	1.00E+06	1.5
30	0.002	0.018	0.006	0.5	1.00E+06	1.5
31	0.001	0.03	0.005	0.5	2.50E+06	1.4

After postprocessing the results, test case no. 29 was selected. While the Reversible scheme yielded the best results, the Gallati scheme provided similar stable outcomes. Figures 4.6 and 4.7 display snapshots at different times of the dam-break simulation after releasing water from the gate using PVSPH, as well as experimental results reported by Janosi et al. (2004).

In wet-bed conditions, as seen in the following snapshots, the behaviour of the fluid significantly differs from the dry-bed conditions. After removing the gate, the static downstream layer resists a quick replacement; therefore, a propagating bore spreads immediately. Unlike the dry-bed where a horizontal jet forms after releasing the column of water, in wet-bed, a vertical and mushroom-like jet appears in both directions. The mushroom-like jet was initially observed by (Stansby et al., 1998).

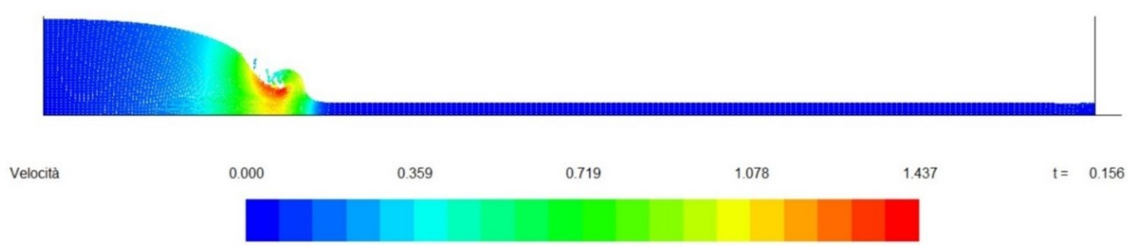

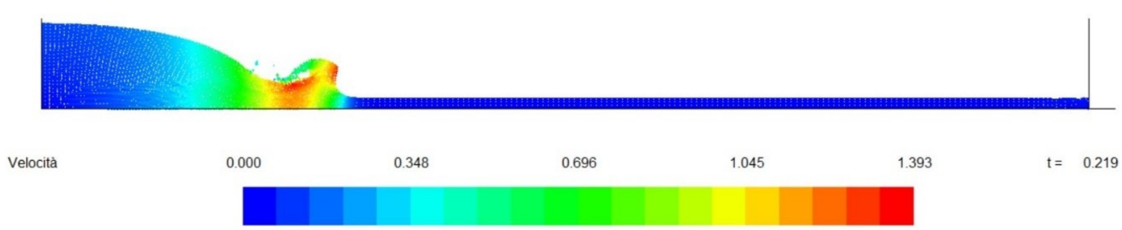

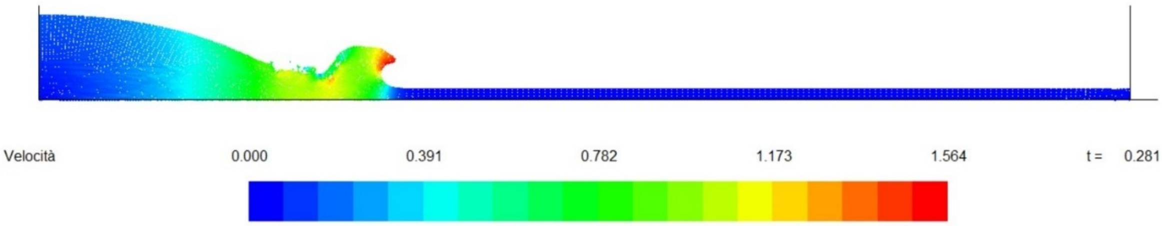
Velocità
0.000
0.391
0.782
1.173
1.564
t = 0.281

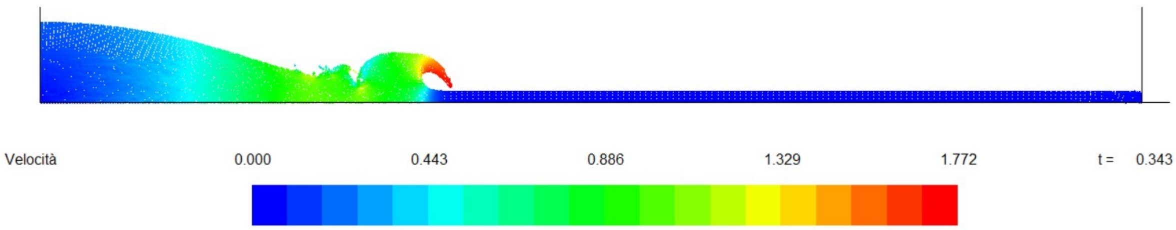
Velocità
0.000
0.443
0.886
1.329
1.772
t = 0.343

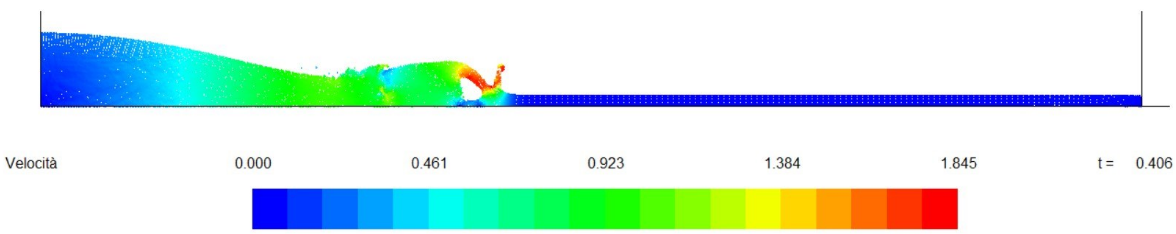
Velocità
0.000
0.461
0.923
1.384
1.845
t = 0.406

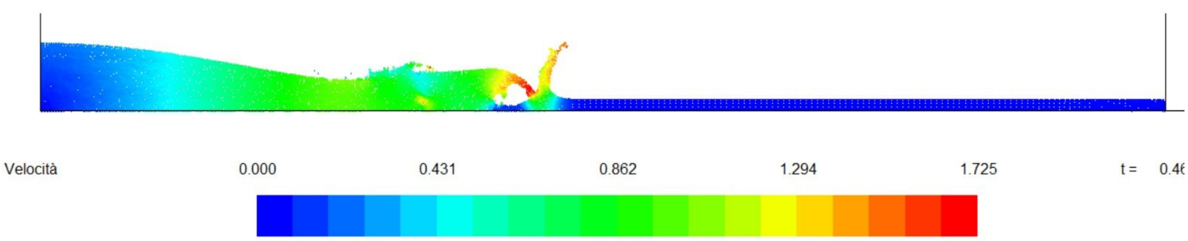
Velocità
0.000
0.431
0.862
1.294
1.725
t = 0.46

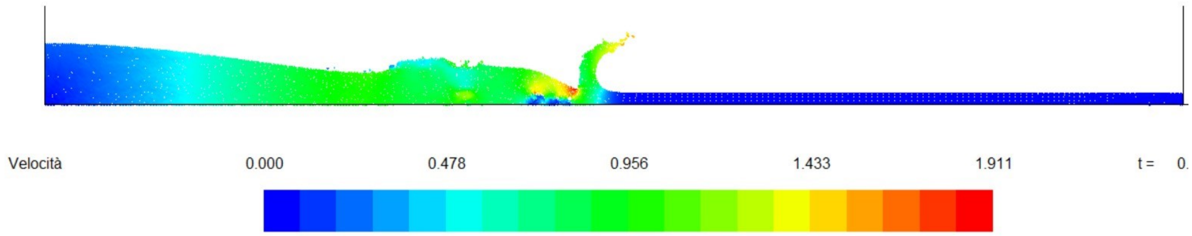

Figure 4. 6. Sequences of snapshots after releasing water from the gate in dam-break simulation by PVSPH for wet-bed, d=0.018m at different times

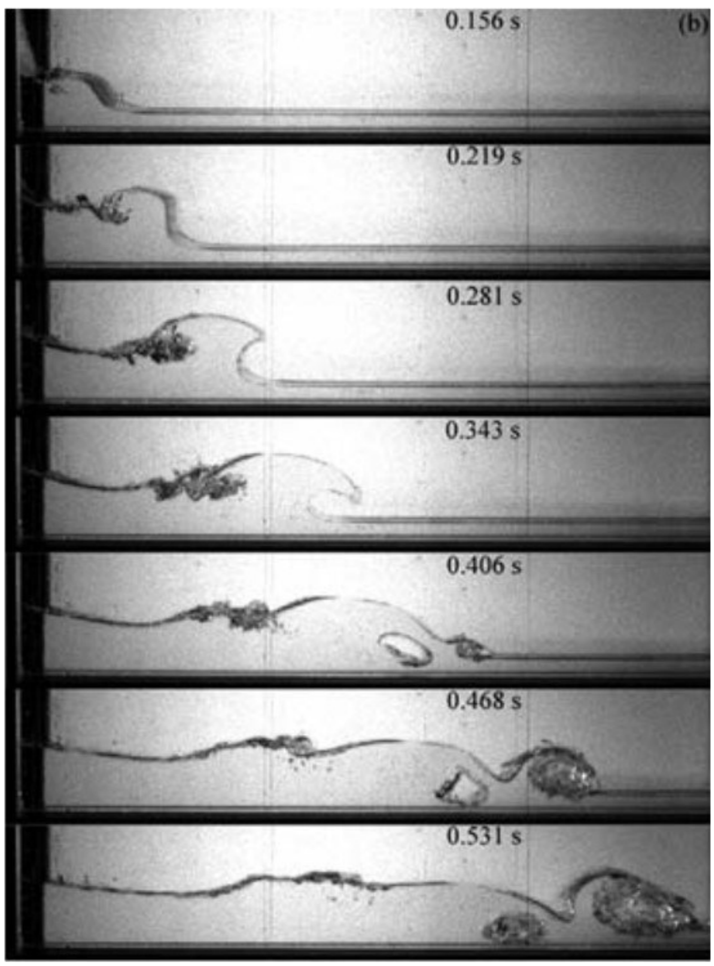

Figure 4. 7. Sequences of snapshots after releasing water from the gate in dam-break experiment for wet-bed, d=0.018m at different times (Janosi et al. 2004)

Figure 4.8 shows the comparison of the water surface profiles at t=0.281s (a) and t=0.406s (b) with PVSPH results. A good agreement is observed in terms of front position and of shape of the wave, as confirmed by the comparison of the water surface profiles at the same times (Fig. 3). The PVSPH results tend to underestimate the amplitude of the wave by a non-negligible amount (7.5% for t1 and 11.0% for t2). Apart from this difference, which can be ascribed to an uncertainty in the exact opening dynamics of the upstream gate, the simulation correctly reproduces dimension and position of the air bubble formed by wave plunging and the overall shape of the propagating bore, demonstrating an overall ability in simulating the key phenomena of a turbulent, Newtonian dam-break flow.

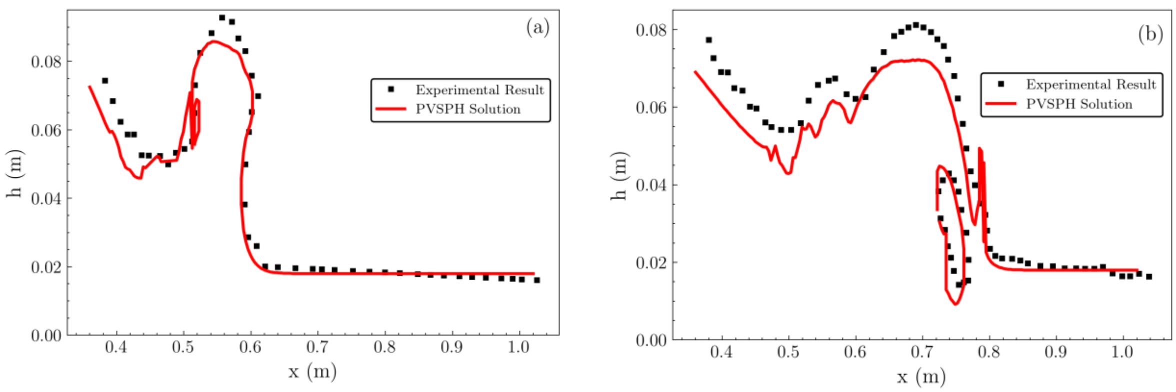

Figure 4. 8. Comparison between measured and simulated water surface profiles for wet-bed condition (d_0=0.018m) at t=0.281s (a) and t=0.406s (b)

4.1.2.2. Wet-bed Dam-break Case (d=0.038m)

The schematic setup of the channel is provided in Figure 4.9. For the wet-bed experiments, similar to the dry-bed test configuration, the flow depths upstream and downstream are 0.15m and 0.038m, respectively.

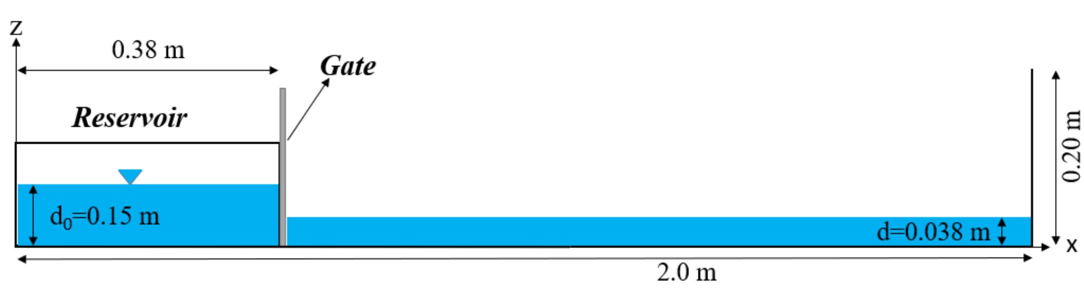

Figure 4. 9. Experimental setup of the SPHERIC reference dam-break case, wet-bed (d=0.038m)

After postprocessing the results, test case no. 7 was selected among the tests conducted (Table 4.4). All the tests were carried out using the same slip boundary condition, Reversible time integration scheme, and a modulus of elasticity equal to 1.00E+06. Sequential snapshots at different times, along with corresponding experimental snapshots for the same time, are shown in Figures 4.10 and 4.11, respectively.

Table 4. 4. List of second trial tests conducted in wet-bed dam-break simulation (d=0.038m)

Test no.	Diameter	Smoothing Velocity	Artificial Viscosity	CFL
1	0.003	0.1	0.01	0.6
2	0.003	0.06	0.01	0.6
3	0.003	0.015	0	0.6
4	0.003	0.055	0.01	0.6
5	0.003	0.015	0	0.4
6	0.004	0.015	0.01	0.2
7	0.002	0.02	0.005	0.5

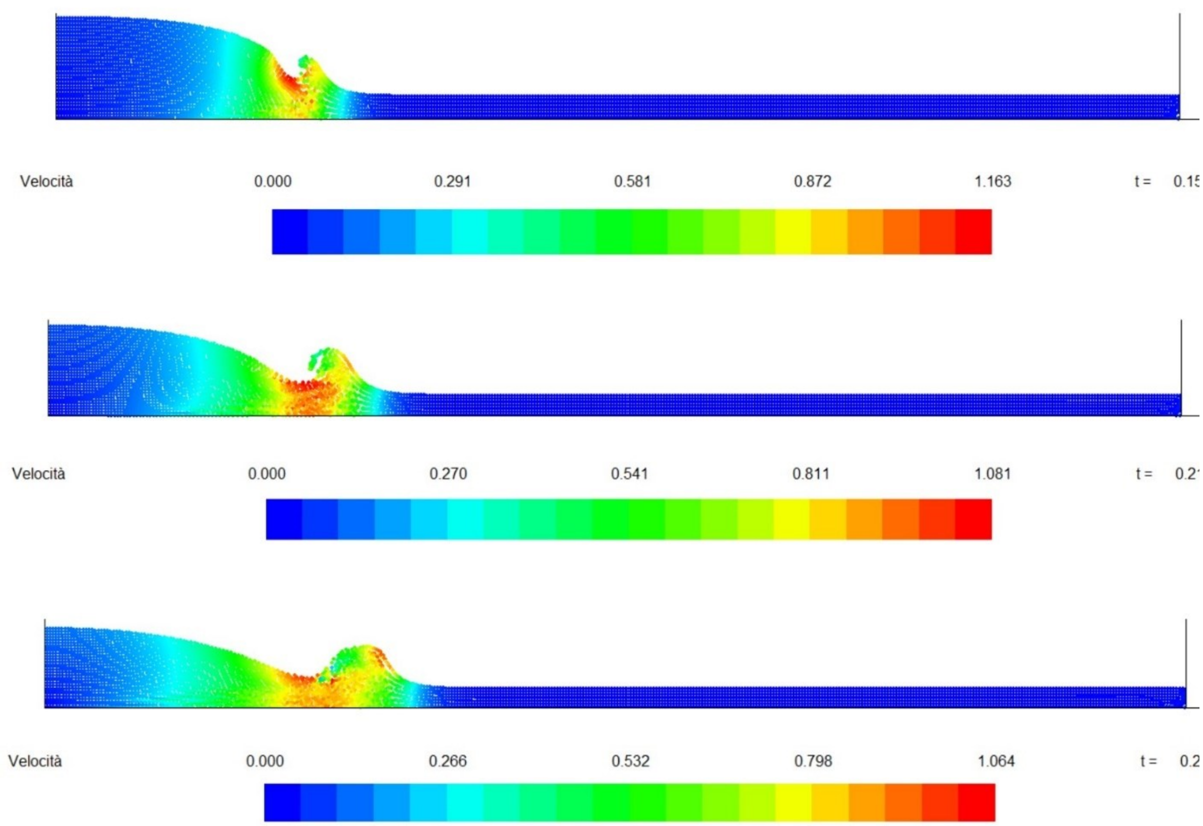

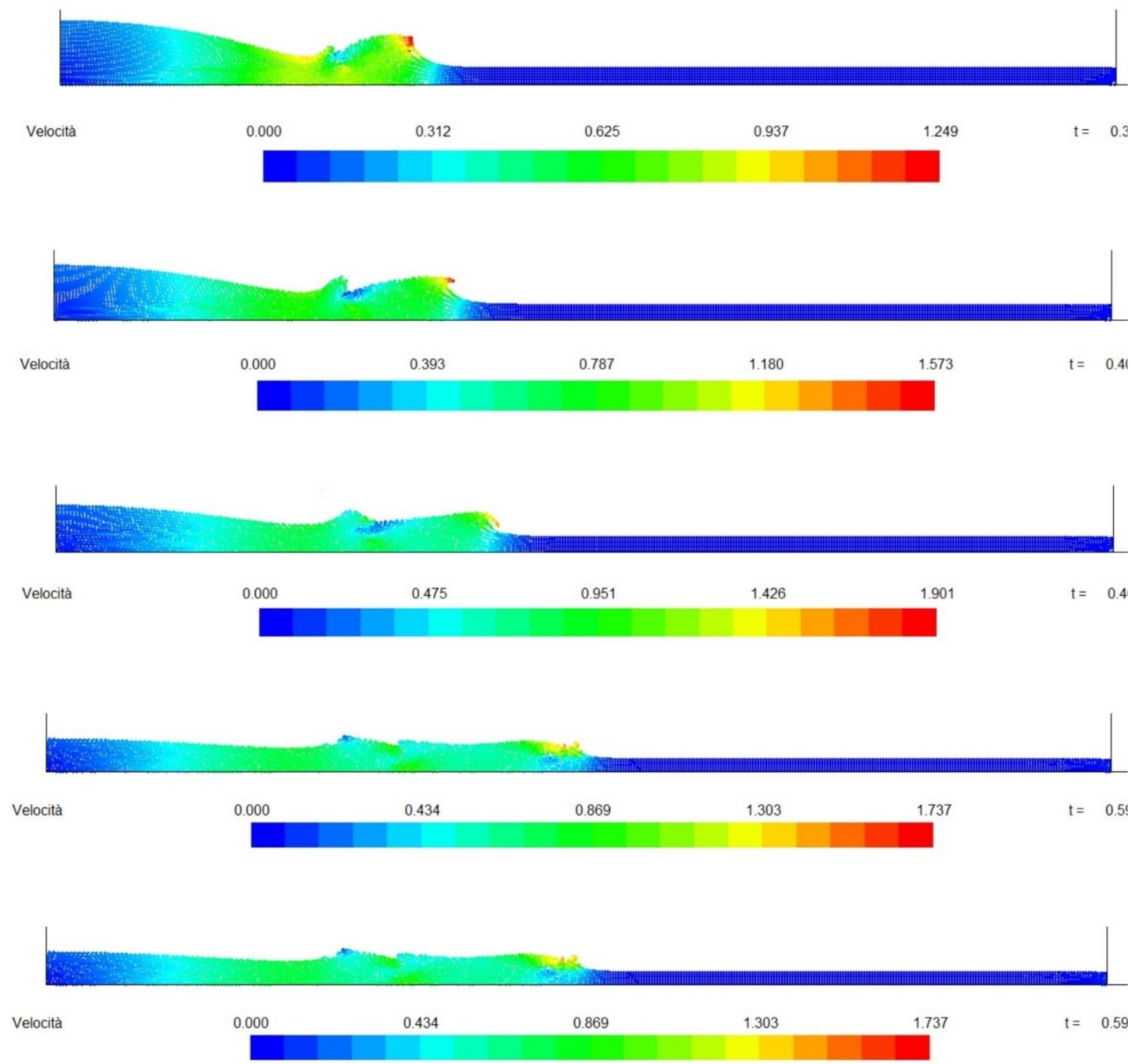

Figure 4. 10. Sequences of snapshots after releasing water from the gate in dam-break simulation by PVSPH for wet-bed, *d*=0.038m at different times

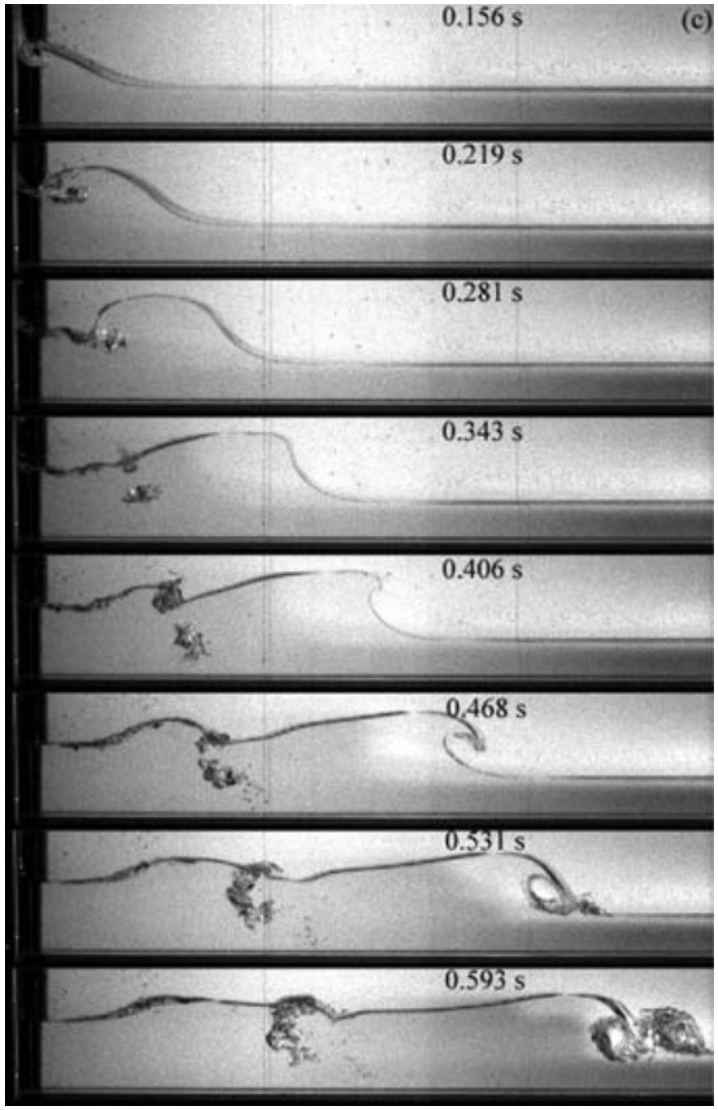

Figure 4. 11. Sequences of snapshots after releasing water from the gate in dam-break experiment for wet-bed, *d*=0.038m at different times (Janosi et al. 2004)

In the comparison between the PVSPH and the experimental results water surface profiles (Figure 4.12), there is acceptable agreement in both the front position and the wave development. At t=0.281s (Figure 4.12a), the RMSE is 13.33%, and at t=0.406s (Figure 4.12b), the RMSE increases to 20.31%. Although there is an increase, the model still indicates reasonable accuracy in representing the position and shape of waves. Overall, in wet-bed conditions with varying thin layers downstream, the PVSPH model works well in simulating dam-break flow for Newtonian fluids.

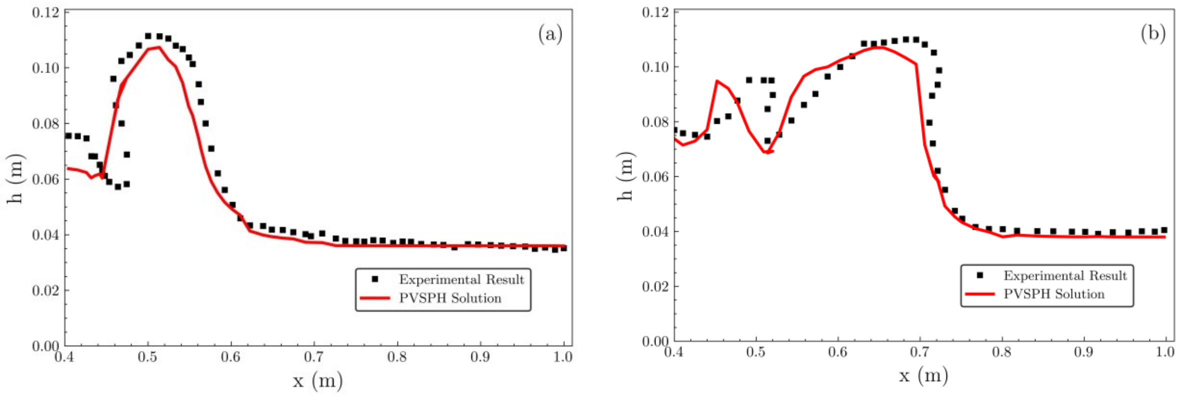

Figure 4. 12. Comparison between measured and simulated water surface profiles for wet-bed condition (d=0.038m) at t=0.281s (a) and t=0.406s (b)

4.1.3. Impact of gate opening on dam-break simulation

As mentioned before, in all dam-break experiments the gate is removed with constant speed of 1.5 m/s, therefore this setup requires simulating dam-break evolution by considering the gate movement. A question arises, what would happen if the gate disappeared instantaneously?

To explore this, the following scenarios are presented:

- Gate presence: The gate is present at the beginning and is removed by constant upward speed (in this case, 1.5 m/s).
- Gate absence: The gate is not physically modeled, and instead, it disappears instantly at the start of the simulation.

So, dam-break tests using PVSPH code with gate presence and gate absence are performed under wet-bed conditions, with upstream and downstream water elevations of 0.15 m and 0.0018 m, respectively. Figure 4.13 indicates the water level profiles at the presence or absence of the gate at different times (0.2, 0.5, 1.0, and 2.0 s). As shown, the presence of the gate causes a slight delay in flow propagation; however, the same general flow trend is observed when the gate is absent. Additionally, the flow peak in the gate presence scenario is slightly higher (around 5% greater) at the initial time (t=0.2s). However, this difference decreases over time, indicating that the gate's effect becomes less pronounced when time progresses. Also, some snapshots for velocity magnitude fields for different times related to the presence and absence of the gate are illustrated in Figure 4.14 and 4.15.

In general, it is obvious that the presence of the gate with upward constant speed in numerical simulation has a meaningful impact on the flow behaviour, particularly at the initial time.

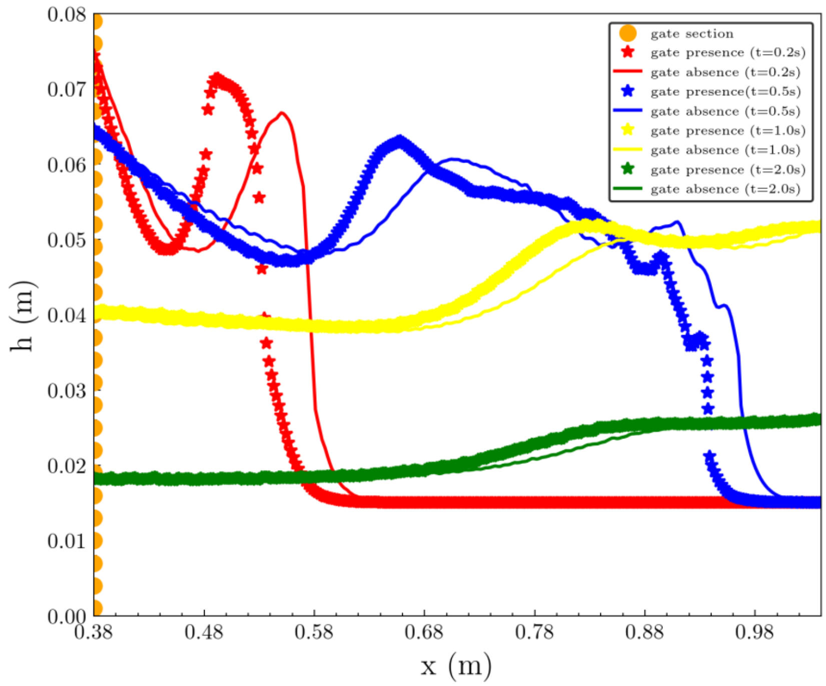

Figure 4. 13. Water level profiles at various times (t=0.2s, t=0.5s, t=1.0s, and t=2.0s) for both gate presence and gate absence situations

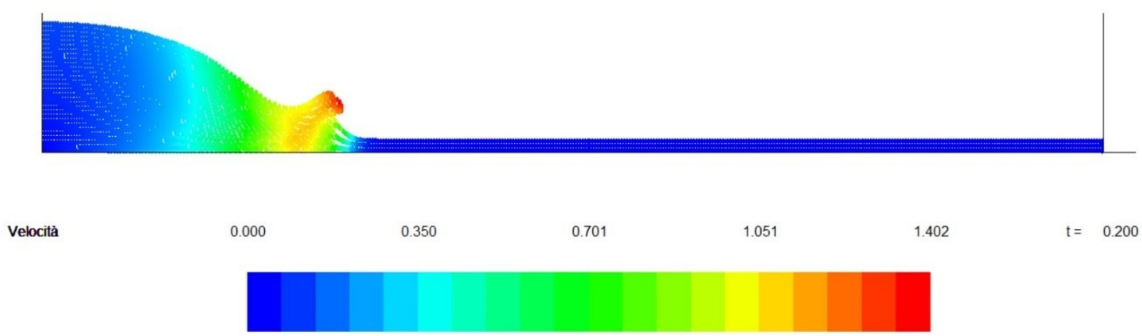

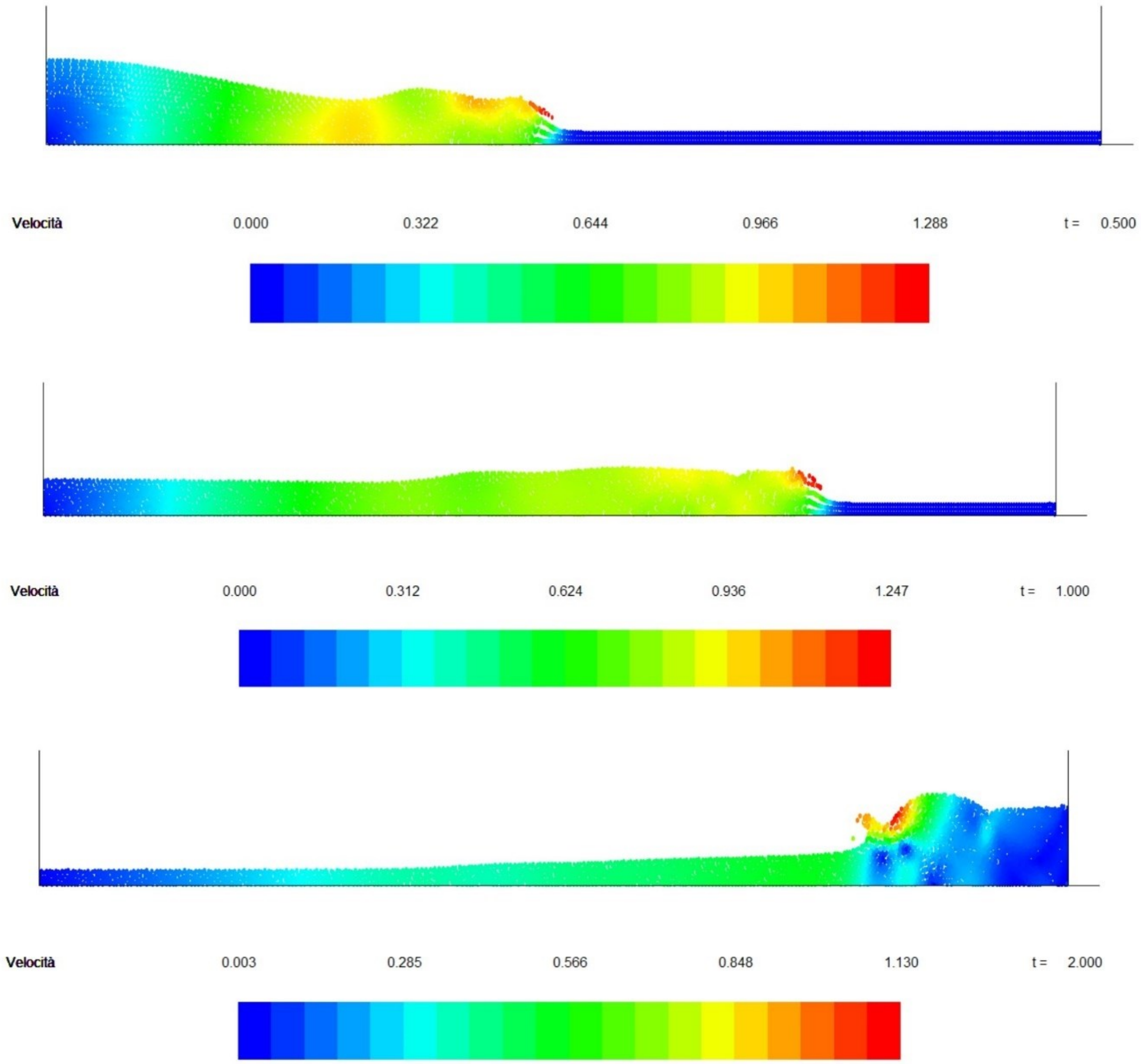

Figure 4. 14. The velocity magnitude fields at different times (t=0.5s to t=2.0s) for gate absence situation.

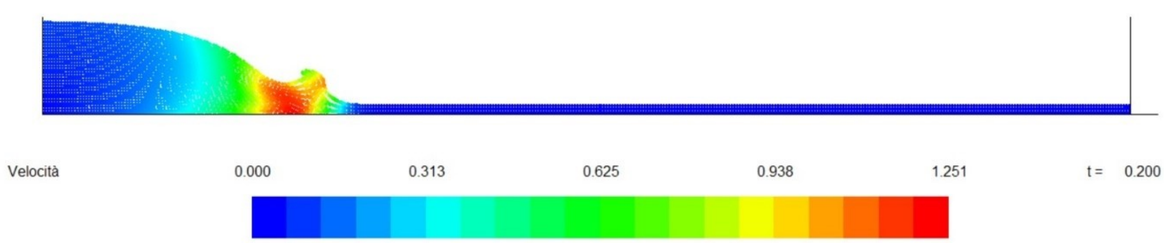

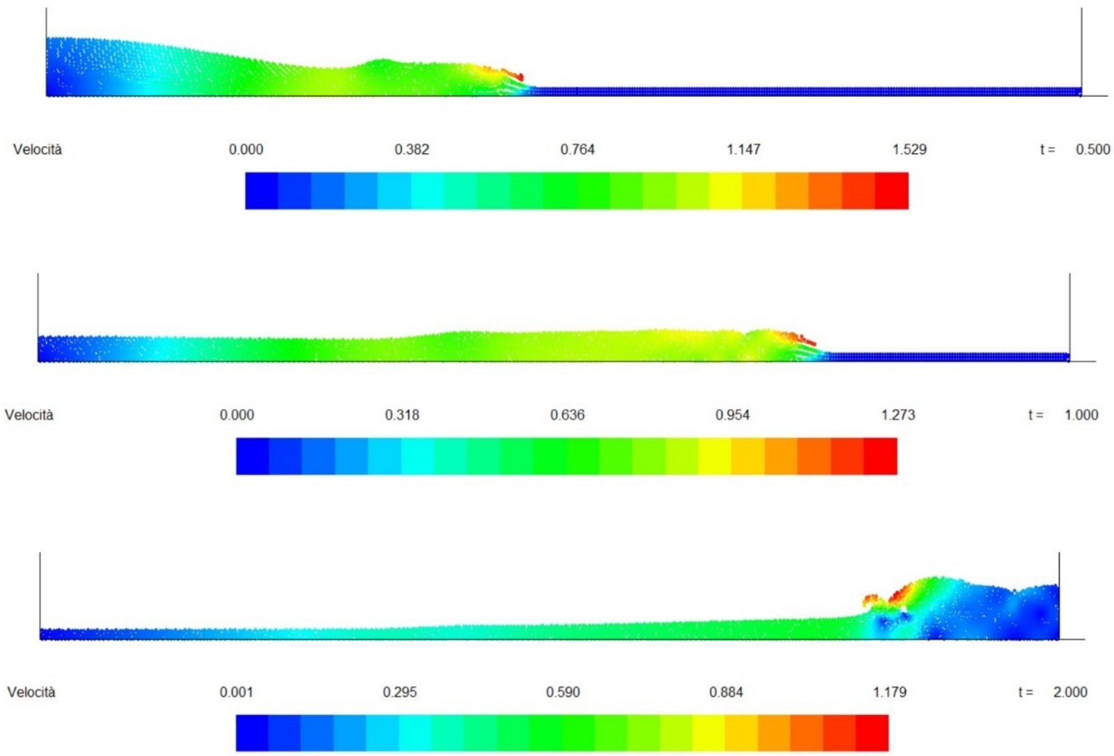

Figure 4. 15. The velocity magnitude fields at different times (t=0.5s to t=2.0s) for gate presence situation

4.1.4. Non-Newtonian Fluid: Plane Poiseuille Flow

To assess the accuracy and performance of SPH simulations for non-Newtonian fluid flows, many researchers (Pan et al., 2013; Xenakis et al., 2015; Xu et al., 2013; Zhou and Sun, 2021) have relied on closed-channel plane Poiseuille flows as a benchmark problem, as they provide well-defined and analytically solvable benchmarks. The performances of the PVSPH model in simulating non- Newtonian fluids flows is performed comparing the results with the known analytical solution for plane Poiseuille flow, enabling its application to more complex and practical fluid dynamics problems.

The non-Newtonian fluid rheology is modelled adopting the Power Law model. As physical and rheological quantities in SPH are directly related to each computational particle, the implementation of the Power Law model in PVSPH is straightforward and allows the application to a wide range of problems.

In Figure 4.16 the channel geometry and flow setup are depicted. To minimize inlet effects, an upstream chamber was introduced in the model as a flow stabilizer, linked through a streamlined convergent to two downstream parallel plates (y= ±H/2), where the Poiseuille flow is evaluated. The flow is driven by a constant pressure gradient in the streamwise direction, resulting in a unidirectional velocity profile in the transverse direction at steady state, as described by following equation. Moreover, no-slip boundary conditions were applied on the upper and lower walls, while periodic boundary conditions were adopted on the inlet and outlet boundaries. Below, the formulas for calculating the analytical solution are presented (Eqs. 4.1, 4.2, and 4.3):

$$u = \frac{n}{n+1}\left[-\frac{1}{\mu_0}\frac{\partial p}{\partial x}\right]^{\frac{1}{n}} \left[\left[\frac{H}{2}\right]^{1+\frac{1}{n}} - |y|^{\left(1+\frac{1}{n}\right)}\right] \tag{4.1}$$

And the maximum velocity

$$u_{max} = \frac{n}{n+1}\left[-\frac{1}{\mu_0}\frac{\partial p}{\partial x}\right]^{\frac{1}{n}} \left[\left[\frac{H}{2}\right]^{1+\frac{1}{n}}\right] \tag{4.2}$$

So, finally

$$\frac{u}{u_{max}} = 1 - (2\left|\frac{y}{H}\right|^{\left(1+\frac{1}{n}\right)}) \tag{4.3}$$

where:

- u is the local velocity at y
- u_{max} is the maximum velocity at the centerline
- y is the transverse distance from the centerline
- H is the distance between the parallel plates
- n is the flow behaviour index for the power-law flow
- $\frac{\partial p}{\partial x}$ is the pressure gradient

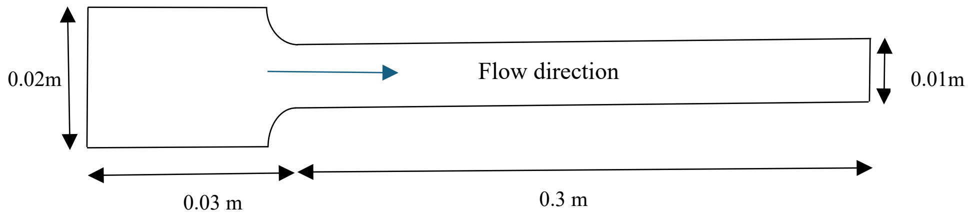

Figure 4. 16. Configuration of Poiseuille flow computational domain

The set-up of reliable simulations required a large number of trials with different values of the appropriate parameters such as velocity smoothing coefficient, density smoothing coefficient, CFL number, Modulus of elasticity, as well as different choices of Kernel functions, and of time integration schemes across various power law exponents. These input parameters are listed in Table 4.5, and also in Figure 4.17 illustrate how different parameters such as CFL number, velocity smoothing coefficient, pressure smoothing coefficient, and Modulus of elasticity can impact on the code accuracy which is represented by R-squared for a specific non-Newtonian fluid (*n*=0.36).

Table 4. 5. List of tests conducted in the Plane Poiseuille flow simulation

Test no.	Diameter	CFL	Smoothing Velocity	Smoothing Density	Type of Viscous Stress	Time Integration Scheme	Rheological Index	Modulus of elasticity
1	0.0005	0.4	0.015	0.2	diretti sistema	Reversible	1	5.00E+05
2	0.0005	0.4	0.015	0.3	diretti sistema	Reversible	1	5.00E+05
3	0.0005	0.35	0.015	0.3	diretti sistema	Reversible	1	5.00E+05
4	0.0005	0.3	0.015	0.3	diretti sistema	Reversible	1	5.00E+05
5	0.0005	0.3	0.015	0.4	diretti sistema	Reversible	1	5.00E+05
6	0.0005	0.35	0.015	0.4	diretti kernel	Reversible	1	5.00E+05
7	0.0005	0.2	0.015	0.4	diretti kernel	Reversible	1	5.00E+05
8	0.0005	0.35	0.03	0.5	diretti kernel	Reversible	1	5.00E+05
9	0.0005	0.3	0.03	0.6	diretti sistema	Reversible	1	5.00E+05
10	0.0005	0.35	0.05	0.3	diretti sistema	Reversible	1	5.00E+05
11	0.0005	0.3	0.05	0.3	diretti sistema	XSPH	1	5.00E+05
12	0.0005	0.3	0.05	0.3	diretti sistema	Gallati	1	5.00E+05
13	0.0005	0.3	0.05	0.3	diretti sistema	XSPH-2	1	5.00E+05
14	0.0005	0.4	0.03	0.3	diretti sistema	Reversible	1	5.00E+05
15	0.0005	0.4	0.02	0.3	diretti sistema	Reversible	1	5.00E+05
16	0.001	0.4	0.05	0.1	morris	Reversible	1	5.00E+05
17	0.005	0.4	0.05	0.1	morris	Reversible	1	5.00E+05
18	0.002	0.3	0.03	0.1	morris	Reversible	1	5.00E+05
19	0.0005	0.4	0.05	0.1	morris	Reversible	1	5.00E+05
20	0.002	0.4	0.05	0.1	morris	Reversible	2	5.00E+05
21	0.002	0.3	0.02	0.1	morris	Reversible	2	5.00E+05
22	0.001	0.4	0.05	0.1	morris	Reversible	0.36	5.00E+05
23	0.001	0.35	0.05	0.1	morris	Reversible	0.36	5.00E+05

24	0.001	0.3	0.05	0.1	morris	Reversible	0.36	5.00E+05
25	0.001	0.4	0.05	0.2	morris	Reversible	0.36	5.00E+05
26	0.001	0.4	0.05	0.05	morris	Reversible	0.36	5.00E+05
27	0.001	0.4	0.05	0	morris	Reversible	0.36	5.00E+05
28	0.001	0.3	0.05	0.05	morris	Reversible	0.36	5.00E+05
29	0.001	0.3	0.02	0.1	morris	Reversible	0.36	5.00E+05
30	0.001	0.3	0.05	0.025	morris	Reversible	0.36	5.00E+05
31	0.001	0.3	0.05	0.1	morris	Reversible	0.36	1.00E+06
32	0.001	0.3	0.05	0.1	morris	Reversible	0.25	5.00E+05
33	0.001	0.3	0.05	0.1	morris	Reversible	2	5.00E+05
34	0.001	0.3	0.05	0.1	morris	Reversible	0.2	5.00E+05
35	0.001	0.3	0.05	0.1	morris	Reversible	0.5	5.00E+05
36	0.0005	0.3	0.05	0.1	morris	Reversible	0.36	5.00E+05
37	0.001	0.3	0.05	0.1	morris	Reversible	1	5.00E+05
38	0.001	0.2	0.05	0.1	morris	Reversible	0.36	5.00E+05
39	0.001	0.3	0.015	0.1	morris	Reversible	0.36	5.00E+05
40	0.001	0.3	0.03	0.1	morris	Reversible	0.36	5.00E+05
41	0.001	0.3	0.07	0.1	morris	Reversible	0.36	5.00E+05
42	0.001	0.3	0.05	0.2	morris	Reversible	0.36	5.00E+05
43	0.001	0.3	0.05	0.05	morris	Reversible	0.36	5.00E+05
44	0.001	0.3	0.05	0.1	morris	Reversible	0.36	2.50E+05
45	0.001	0.4	0.07	0.2	morris	Reversible	0.36	1.00E+06
46	0.001	0.5	0.05	0.1	morris	Reversible	0.36	5.00E+05
47	0.001	0.3	0.1	0.1	morris	Reversible	0.36	5.00E+05
48	0.001	0.3	0.05	0.15	morris	Reversible	0.36	5.00E+05

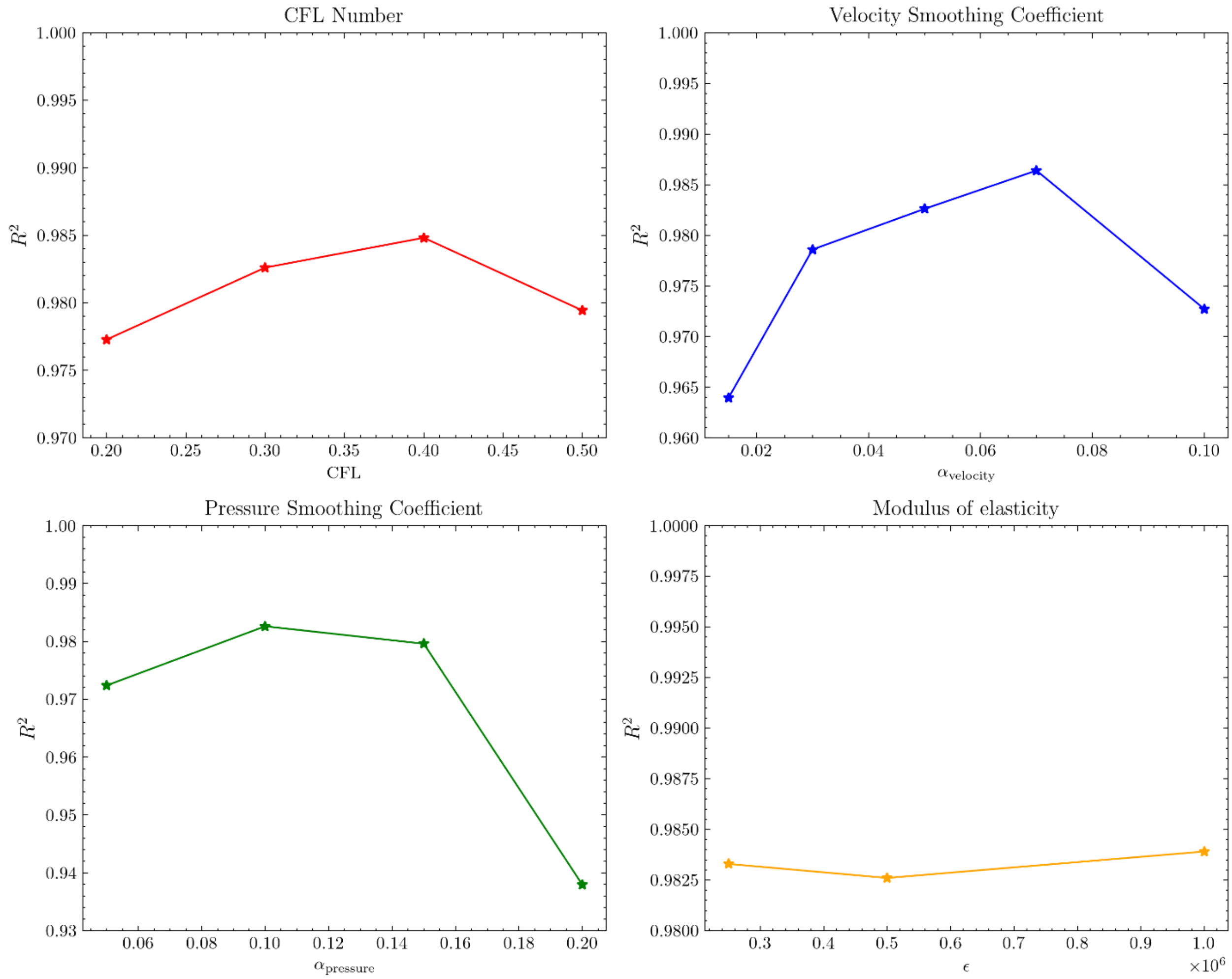

Figure 4. 17. Investigation impact of CFL number, velocity smoothing, pressure smoothing, and Modulus of elasticity on the R-squared for a specific non-Newtonian fluid

After that, from the sensitivity analysis (Figure 4.16), the PVSPH code is tuned by the following parameters:

- Particle parameter: 0.005m
- CFL number: 0.3-0.4
- Smoothing velocity coefficient: 0.02-0.04
- Smoothing density coefficient: 0.1-0.15
- Type of Viscous Stress: Morris
- Time Integration Scheme: Reversible (Both the Reversible and Gallati schemes yielded similar stable results)
- Modulus of elasticity: 5.00E+05 (its impact on the model's accuracy appears to be minimal)

For the validation of the code, by using the proper parameters and according to the Power law equation, all the different fluid types (n=1 for Newtonian fluid, n <1 for a non-Newtonian shear-thinning fluid, and n >1 for a non-Newtonian shear-thickening fluid) were tested and, hence, the following values of n are selected: 0.25, 0.36, 0.5, 1.0, and 2.0. As an example, the results of the SPH model for Newtonian fluid are compared with the analytical solution, as shown in Table 4.6.

Table 4. 6. The result of the Plane Poiseuille Flow test for Newtonian fluid

			Analytical	PVSPH
n	*y*	*y/H*	*U/Umax*	*U/Umax*
1	0.0005	-0.45	0.19	0.197119
1	0.001	-0.4	0.36	0.376595
1	0.0015	-0.35	0.51	0.532596
1	0.002	-0.3	0.64	0.661603
1	0.0025	-0.25	0.75	0.769398
1	0.003	-0.2	0.84	0.854316
1	0.0035	-0.15	0.91	0.919508
1	0.004	-0.1	0.96	0.964314
1	0.0045	-0.05	0.99	0.990949
1	0.005	0	1	1
1	0.0055	0.05	0.99	0.991667
1	0.006	0.1	0.96	0.96562
1	0.0065	0.15	0.91	0.920993
1	0.007	0.2	0.84	0.855582
1	0.0075	0.25	0.75	0.770036
1	0.008	0.3	0.64	0.661613
1	0.0085	0.35	0.51	0.532147
1	0.009	0.4	0.36	0.375977
1	0.0095	0.45	0.19	0.196691

The following Figure 4.18 depicts the results obtained for different values of the exponents n=0.25, 0.36, 0.5, 1.0, and 2.0, with the solid lines represent the simulation results, while the scattered points denote analytical solutions.

Figure 4.19 depicts some snapshots for the velocity magnitude fields at different times for non-Newtonian fluid (n=0.36) by PVSPH code.

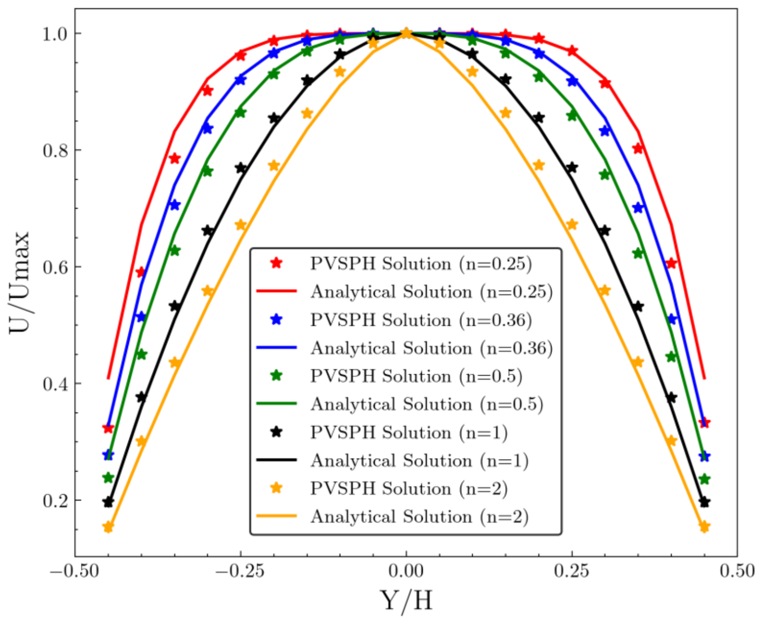

Figure 4. 18. The results of different methods for non-Newtonian power law flows (Analytical and PVSPH solution)

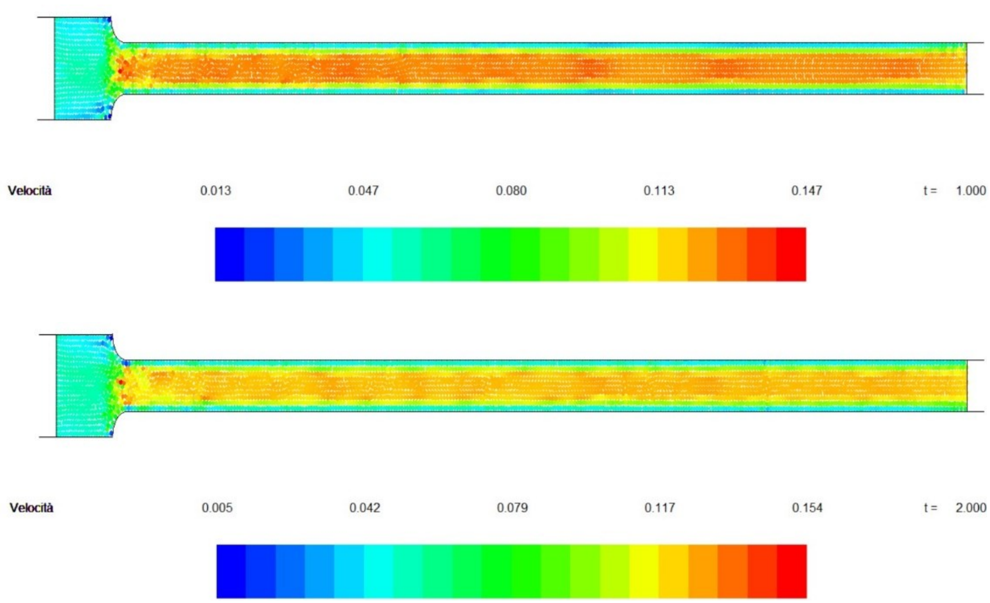

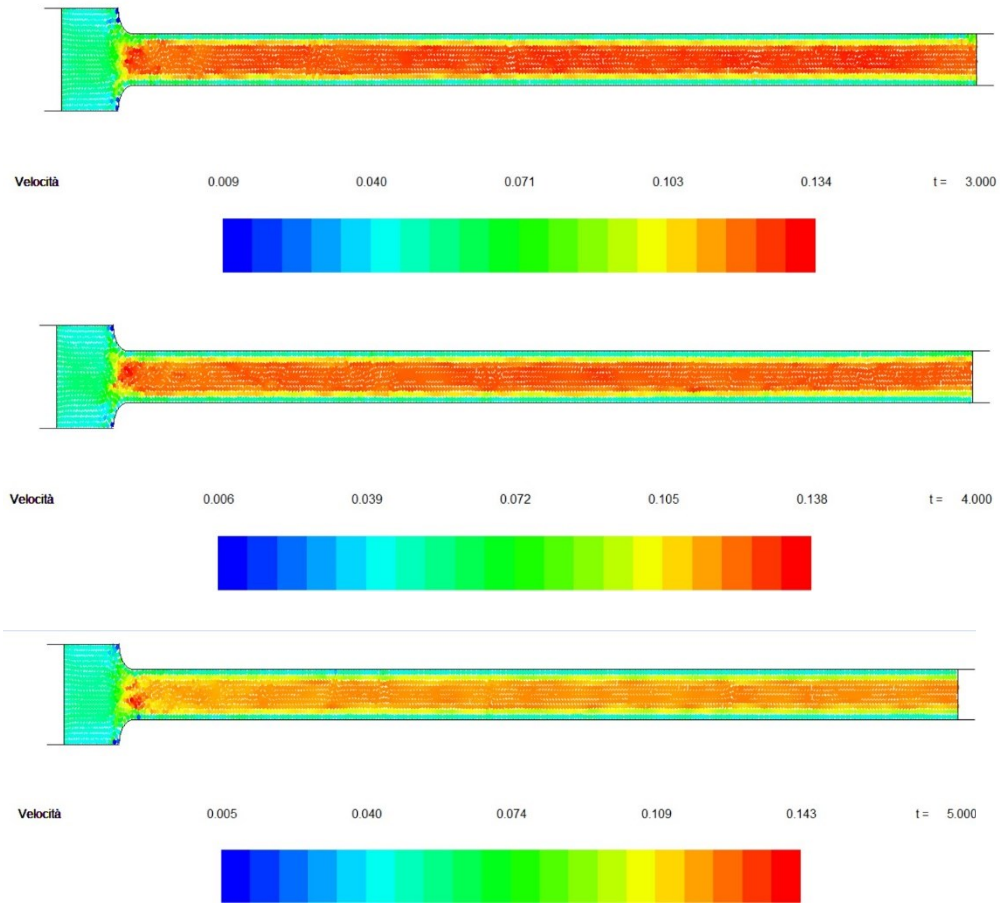

Figure 4. 19. Snapshots for the velocity magnitude fields at different times for non-Newtonian fluid by PVSPH code, *n*=0.36

The comparison demonstrates the PVSPH model capability to accurately reproduce velocity profiles with highly acceptable results. The correlation coefficient between the theoretical velocity and the simulated values ranges from 0.958 to 0.997 for the different considered rheological indices (Table 4.7) and shows the good accuracy of the SPH method in predicting fluid behaviour across a range of rheological indices.

Table 4. 7. R-squared and RMSE (%) for SPH and analytical solutions across different rheological indices

Rheological index (*n*)	R-squared	RMSE (%)
0.25	0.958	4.40%
0.36	0.983	3.48%
0.5	0.992	2.81%
1	0.997	2.09%
2	0.994	3.36%

Figure 4.20 shows the velocity profile at a distance of 0.2m from inlet for different time steps. It can be seen that as the simulation time increases, the velocity profile becomes more developed. Initially, the profile shows a steep slope, however, it becomes smoother, near the walls the velocity is about zero and the maximum velocity is at the center. This behaviour indicates the flow stabilization and reaching a steadier state.

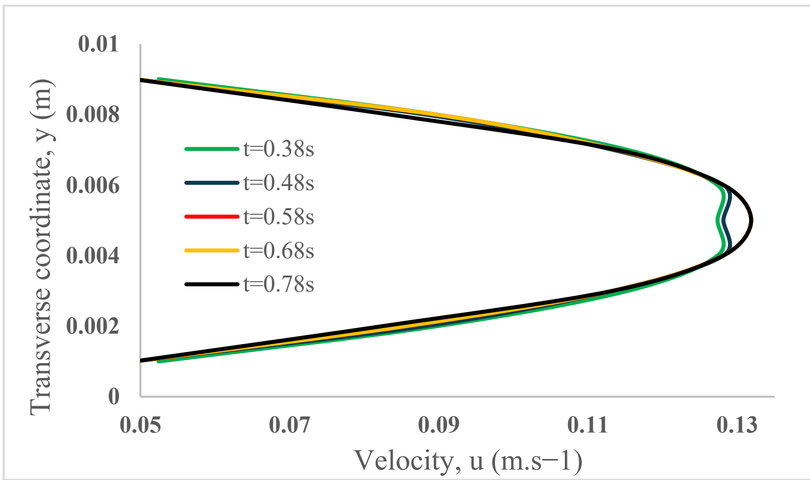

Figure 4. 20. Velocity profile in various times for non-Newtonian fluid (*n*=0.36) at *x*=0.2m

4.1.5. One-phase vs two-phase models

In this part of our research, a set of simulations was conducted, focusing on both one-phase (water) and two-phase (air and water) scenarios. The dam-break flow tests conducted by Andrea et al. (2024) at the Hydraulic Laboratory of the University of Naples Federico II were used for comparison and validation. The scheme of the experimental closed-end flume is reported in Figure 4.21, which presents a partial elevation of bottom downstream the gate. Dry-bed conditions are assumed. Three different upstream water elevations were tested: 0.16m, 0.20m, and 0.24m; however, the subsequent tests focused specifically on the 0.20 m case. The experimental test considered has been reproduced using the PVSPH with both one phase and two-phase configurations.

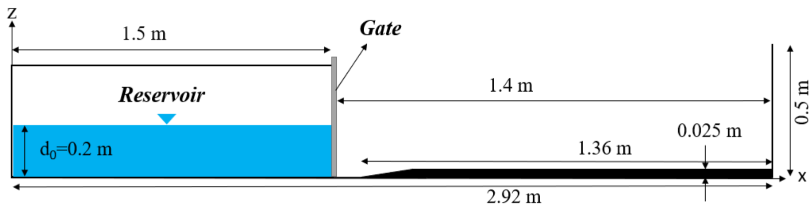

Figure 4. 21. Schematic of the flume setup used in the Naples University tests

A sequence of simulations was carried out by the one phase PVSPH to determine the optimal parameters for obtaining stable results, as shown in Table 4.8. Different parameters, such as smoothing velocity and density coefficients, artificial viscosity, and time integration methods, were analyzed to assess their impact on the accuracy of the model. It is worth noting that all the tests were performed under the slip condition, with a CFL number of 0.5, and a particle diameter of 0.005m.

Through post-processing, test No. 18 presented the best solution. For this case, the comparison between the experimental and PVSPH free surface profiles at different time intervals (t = 1s, t = 2s, and t = 3s) after opening the gate is presented in Figures 4.22, 4.23, and 4.24, respectively. It is important to note that the location of the gate was at the starting point of the coordinate axes in these plots. Also, Figures 4.25 presents snapshots of the velocity magnitude fields at various time intervals. As can be seen from the figures, the numerical model was able to simulate the laboratory conditions with the lowest error, with an RMSE percentage of 8.17% at t = 1s, 12.50% at t = 2s, and 10.44% at t = 3s.

Table 4. 8. Tests conducted in dam-break simulation with downstream elevation

Test no.	Smoothing Velocity	Smoothing Density	Artificial Viscosity	Time Integration Scheme
1	0.02	0.1	0.005	Reversible
2	0.03	0.1	0.005	Reversible
3	0.04	0.1	0.005	Reversible
4	0.05	0.1	0.005	Reversible
5	0.02	0.1	0.01	Reversible
6	0.03	0.1	0.01	Reversible
7	0.04	0.1	0.01	Reversible
8	0.05	0.1	0.01	Reversible
9	0.02	0.1	0.005	XSPH-2
10	0.03	0.1	0.005	XSPH-2
11	0.04	0.1	0.005	XSPH-2

12	0.05	0.1	0.005	XSPH-2
13	0.02	0.1	0.005	XSPH
14	0.03	0.1	0.005	XSPH
15	0.04	0.1	0.005	XSPH
16	0.05	0.1	0.005	XSPH
17	0.02	0.2	0.005	XSPH
18	0.03	0.2	0.005	XSPH
19	0.04	0.2	0.005	XSPH
20	0.05	0.2	0.005	XSPH
21	0.03	0.1	0.005	Gallati
22	0.03	0.15	0.005	Gallati
23	0.03	0.2	0.005	Gallati

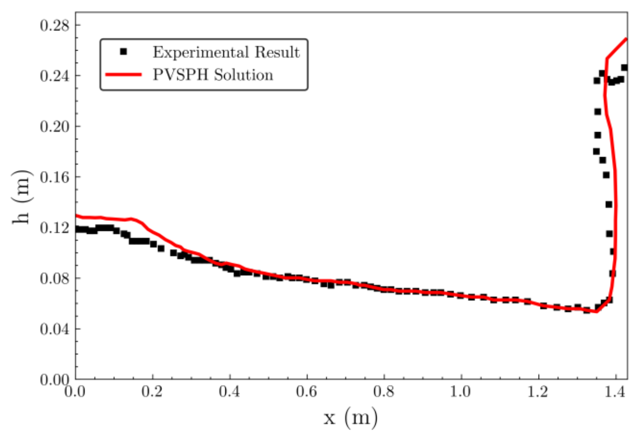

Figure 4. 22. Comparison between measured and simulated water surface profiles at t = 1s (experimental test conducted at the University of Naples)

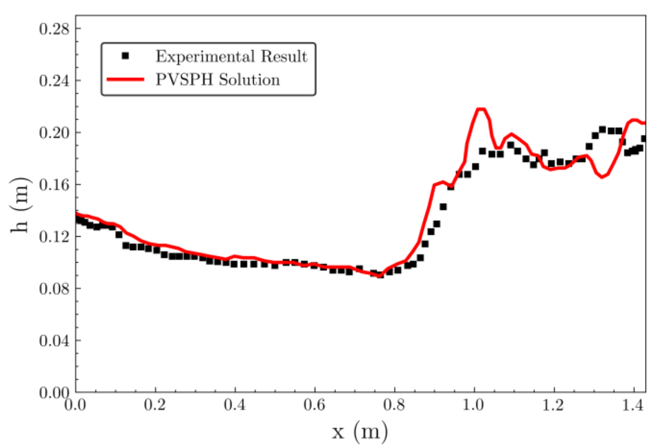

Figure 4. 23. Comparison between measured and simulated water surface profiles at t = 2s (experimental test conducted at the University of Naples)

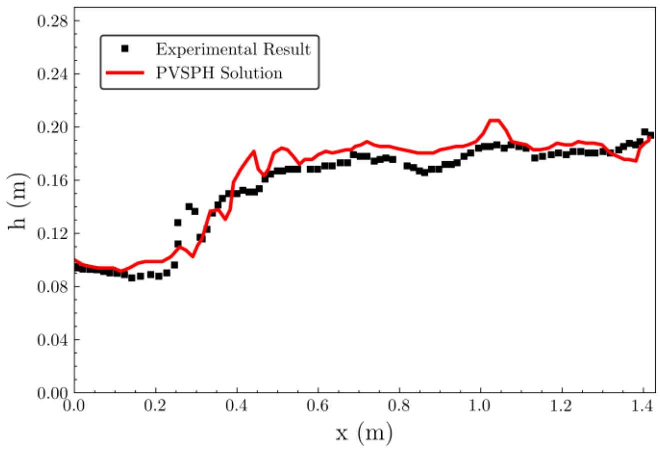

Figure 4. 24. Comparison between measured and simulated water surface profiles at t = 3s (experimental test conducted at the University of Naples)

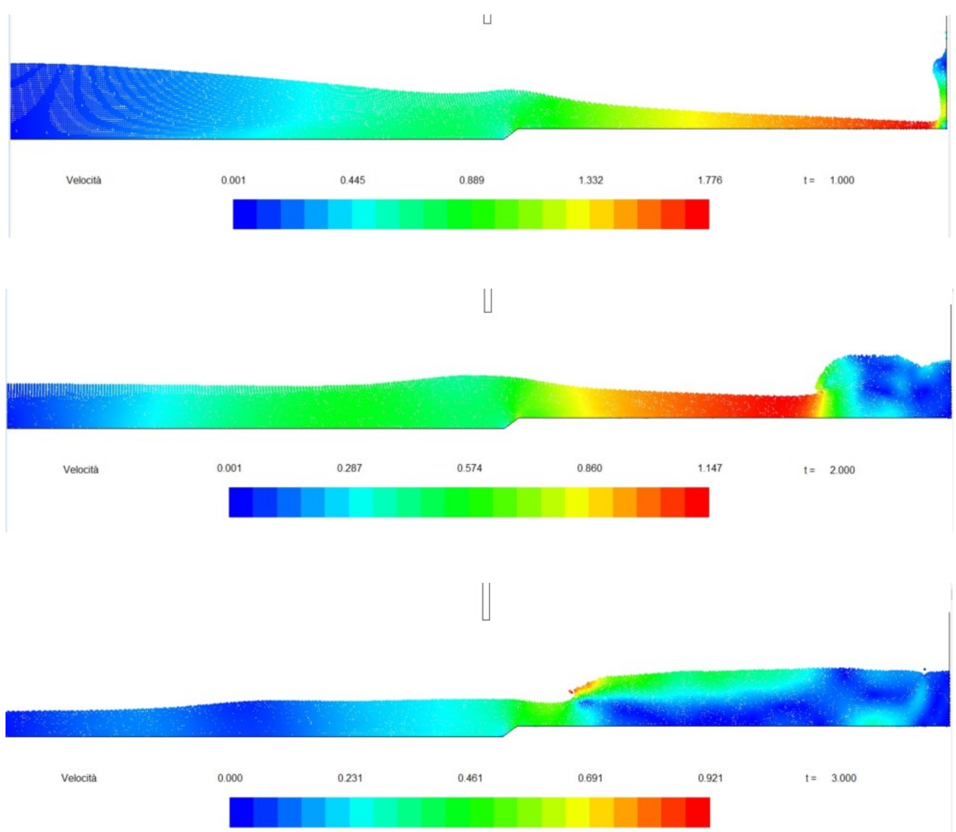

Figure 4. 25. The velocity magnitude fields at different time intervals (t = 1s, t = 2s, and t = 3s) for the one-phase model simulations

The one-phase model has been effective for water-only simulations while incorporating air may provide better results. So, the two-phase model can be used to evaluate the interaction between air and water particles during the dam-break simulation. Multiphase flow simulations, due to the large density differences (e.g., water and air), are computationally expensive as they require very small particles to accurately capture the interface. Moreover, the SPH methods can suffer from numerical instabilities at these interfaces (Chen et al., 2015; Hu and Adams, 2007). In real-world scenarios, such as fluid dynamics involving free surface flows, the coupling between two phases (water and air) can significantly affect the accuracy of the simulation. Therefore, adopting the two-phase model in SPH simulations allows for a more realistic representation of these interactions. Previous studies have demonstrated the importance of the two-phase SPH model in simulating multiphase flows, particularly in situations involving rapid water displacement, such as dam-breaks and coastal flooding (e.g., Liu and Liu, 2015; Monaghan and Kocharyan, 1995).

The dam-break simulation can be performed in two-phase models for some reasons such as being closer to reality, higher accuracy, and taking into account the pressure variations. Therefore, the dam-break test has been also simulated with the two-phase configuration with the same diameter of air and water particles equal to 0.02m.

Figures 4.26, 4.27, and 4.28 present the comparison between experimental measurements and the simulated free surface profile using the two-phase model at different time intervals (t = 1s, t = 2s, and t = 3s). Although the results show that the numerical model has a higher RMSE percentage (11.08% at t = 1s, 14.65% at t = 2s, and 16.53% at t = 3s) compared to the single-phase model, the two-phase model was still able to simulate the shape and position of the backwater wave from end of the flume correctly. However, further experiments are required in the future to improve the accuracy of the results and make them closer to the real-world complexities of flow dynamics induced by dam-break. Snapshots of velocity magnitude fields for different time intervals are shown in Figure 4.29. According to the snapshot of the results obtained from one-phase and two-phase, it can be seen that the results for both simulations were acceptable, although the one-phase results were closer to the laboratory results.

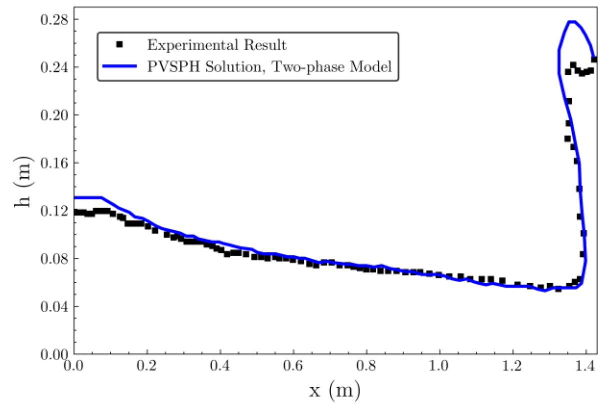

Figure 4. 26. Comparison of measured and simulated water surface profiles using the two-phase model at t = 1s (experimental measurements conducted at the University of Naples)

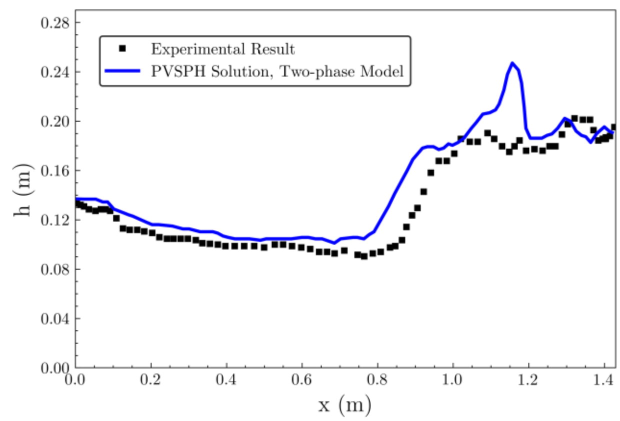

Figure 4. 27. Comparison of measured and simulated water surface profiles using the two-phase model at t = 2s (experimental measurements conducted at the University of Naples)

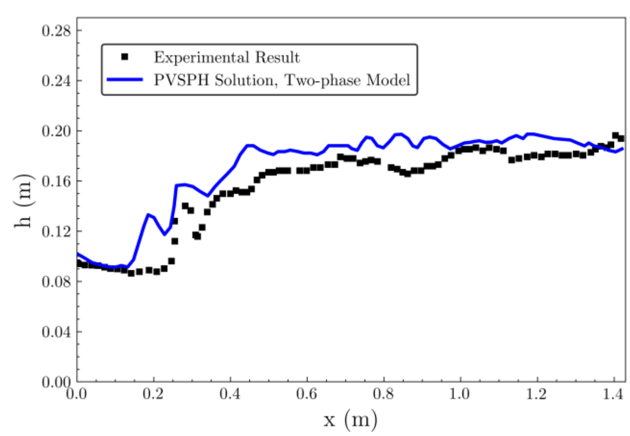

Figure 4. 28. Comparison of measured and simulated water surface profiles using the two-phase model at t = 3s (experimental measurements conducted at the University of Naples)

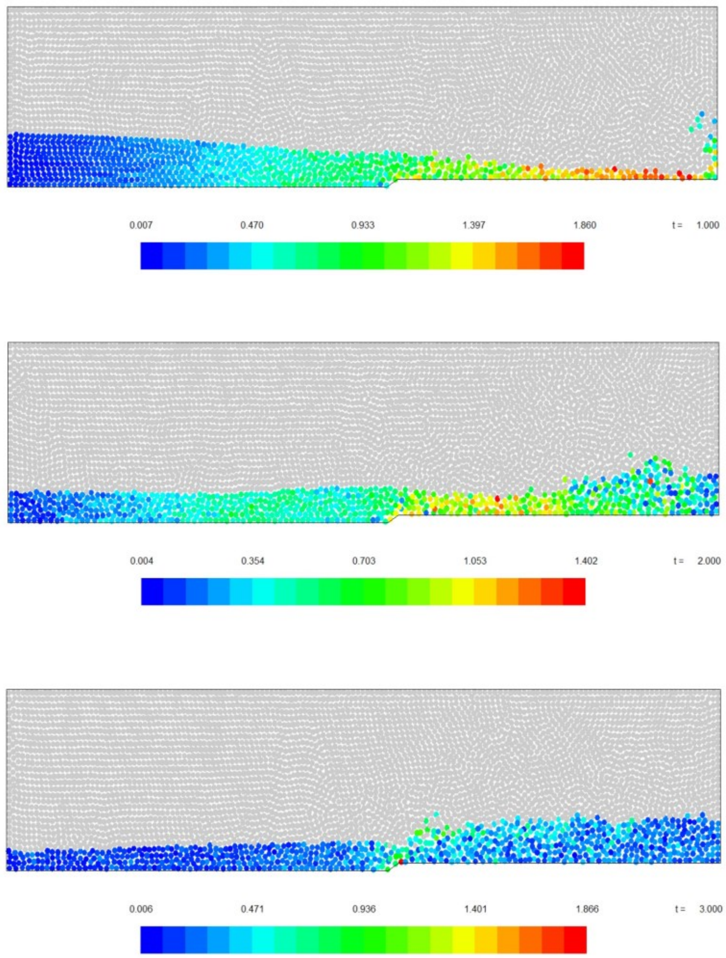

Figure 4. 29. The velocity magnitude fields at different time intervals (t = 1s, t = 2s, and t = 3s) for the two-phase model simulations

4.2. Results: Newtonian and non-Newtonian dam-break simulations

Dam-break simulations have been performed, considering both turbulent water flow and non-Newtonian fluids with a power-law rheology. The considered non-Newtonian fluids correspond to a kaolinite suspension represented by fine sands in water at a specific concentration, used to describe mudflows. The performances of the PVSPH model are compared with the output of the Eulerian Depth Averaged Model (EDAM) and the Eulerian Depth Resolved Model (EDRM), describe in chapter 2. In the following some information about EDAM and EDRM simulations are furnished.

- Eulerian and EDRM simulations

The capability of presented EDAM of reproducing the dam-break of a power-law fluid has been previously verified in (Di Cristo et al., 2022), through the comparison between the numerical and experimental temporal propagation of the front position. The numerical simulations performed with the EDAM herein presented have been carried out adopting a spatial discretization step Δx =0.0093m and a temporal time step Δt =0.0002s. Sensitivity to the discretization has been checked by halving the Δx and Δt under constant CFL, obtaining differences on the estimated peak force smaller than 1%. In the EDAM simulation the instantaneous opening of the gate is assumed.

The Eulerian Depth Resolved Model (EDRM) presented for dam-break simulations has been validated using the open-source CFD solver interFoam, part of the OpenFOAM toolkit (OpenCFD, 2016). The numerical simulations are based on the 2D Navier-Stokes equations for incompressible fluids and utilize the Volume of Fluid (VOF) method to track the free surface. Simulations were carried out with a mesh obtained by the superposition of five layers defined with proper offset of the bottom surface. The layers are non-conformal along the streamwise direction, whereas the normal-to-the bottom resolution increases within each layer approaching the solid wall. For the lowest layer, the discretization is characterised by Δx = 0.003m, Δy = 0.0025m. A time step Δt = 0.0002s was used to maintain a constant CFL=0.5 condition. A sensitivity analysis was performed by refining Δx, Δy and Δt, demonstrating that the differences in the peak force estimates were less than 5%.

4.2.1. Water dam-break simulations

The performances of the PVSPH model are preliminary tested respect the experimental data. Water dam-break simulations reproduce laboratory experiments conducted at the University of Pavia performed by (Manciola et al., 1994). Different geometrical configurations are considered, as indicated in the schemes shown in Fig. 4.30. The flume is rectangular, 9.296m long and 0.487m wide with a fixed flat bottom. In scheme (a) (Fig. 4.30a) the bottom is horizontal, while in scheme (b) downstream the gate, at x=5.170m from the beginning of the channel, the bed has an inverse slope (Fig. 4.30b). In the scheme (b) the channel is closed downstream with a fixed wall at the downstream end, while for the configuration (a) both open-end and close-end configurations are considered. In all cases the dry-bed condition is present after the gate. The initial water depth upstream the gate is equal to 0.35m in the scheme A (Fig 4.29a), while it is 0.3m for the inverse slope channel (Fig 4.29b). For all tests, the gate was removed at a constant velocity of 5m/s.

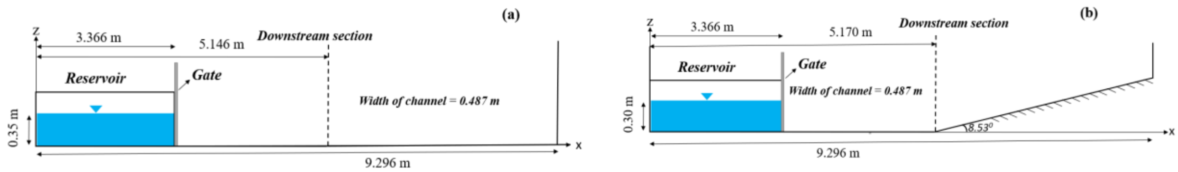

Figure 4. 30. Experimental setup of the reference dam-break case (University of Pavia): (a) closed-end and open-end flume, and (b) inverse slope flume. The x-axis originates at the beginning of the channel

4.2.1.1. PVSPH preliminary tests

In the water dam-break laboratory experiment, the gate lifting speed is 5m/s. To evaluate the influence of the opening time on the flow rate and wave formation three numerical tests were performed with the PVSPH model, reducing the speed up to 1.3m/s. Figure 4.31 shows the time evolution of the discharge at the gate section, indicating that a speed exceeding 3m/s does not substantially influence the results. For this reason, the velocity of 5m/s is assumed in all simulations.

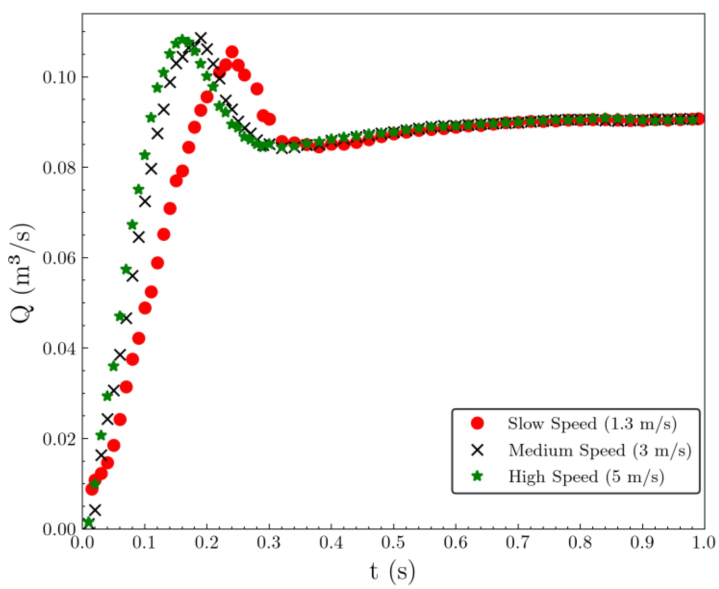

Figure 4. 31. Time evolution of the flow rate in the gate section for a Newtonian fluid with different gate lifting speed

To assess the independence of the PVSPH results from the particle size resolution, three different simulations were performed setting different particle diameters: 0.01m, 0.005m or 0.002m. Fig. 4.32

reports the discharge hydrograph at the gate section, showing that a reduction of the particle diameter below 0.005m does not influence the results. For this reason, the *d*=0.005m is assumed in all simulations.

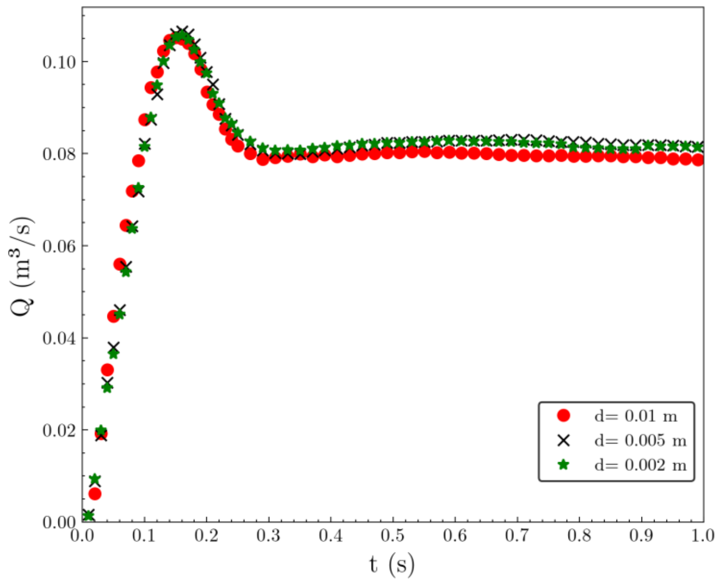

Figure 4. 32. Time evolution of the flow rate in the gate section for a non-Newtonian fluid (*n*=0.1) for different particle diameters

4.2.1.2. Water dam-break: horizontal bed open-end configuration

The method of characteristics for modelling dam-break in a dry-bed was first introduced by Ritter in 1892. The dam-break can be represented by the abrupt removal of a vertical gate. Ritter observed after removal of the gate, a negative wave moves to upstream, whereas a dam-break wave propagates in the downstream direction. Additionally, in the characteristic method, hydrostatic pressure distribution is assumed, and the vertical acceleration generated after the gate removal is neglected (Chanson, 2004).

Before discussing the comparison of the wave profiles, it is important to first understand the foundational calculations related to dam-break simulations using Ritter's analytical solution Eqs. 4.4 to 4.8. Ritter's solution provides a framework for estimating the water surface profile, propagation speed, velocity, and discharge in the context of a dam-break flow. The Ritter's solution with the initial depth in the reservoir $h_0 = 0.35\ m$ furnishes the following outputs:

- At the origin, gate (*x*=0), the constant water depth is:

$$y = \frac{4}{9} * h_0 = 0.1556m \tag{4.4}$$

- The propagation speed of the dam-break wave front is:

$$U = 2 * c_0 = 2\sqrt{gh_0} = 3.706 \ \frac{m}{s} \tag{4.5}$$

- The velocity at the origin (x=0):

$$V(x = 0) = \frac{2}{3}\sqrt{gh_0} = 1.2.35 \ \frac{m}{s} \tag{4.6}$$

- The discharge at the origin (x=0) per unit channel width is:

$$q(x = 0) = \frac{2}{3}\sqrt{gh_0} * y = \frac{4}{9}h_0 * \frac{2}{3}\sqrt{gh_0} = \frac{8}{27} * 0.5 * \sqrt{9.8 * 0.5} = 0.1922 \ \frac{m^2}{s} \tag{4.7}$$

- The water evaluation profile in time is given by:

$$h = \frac{4}{9}h_0 + \frac{x^2}{9gt^2} - \frac{4x}{9gt} * \sqrt{gh_0} \rightarrow h = \frac{x^2}{9gt^2} - \frac{4\sqrt{h_0}x}{9\sqrt{g}t} + \frac{4}{9}h_0 \tag{4.8}$$

Figure 4.33 presents the comparison of the water surface profile at t=1.0s, obtained from the PVSPH simulations, with the analytical Ritter solution. Based on the comparison of numerical and analytical results, it can be concluded that the model predicts well the depth at the gate section. The slight differences can be attributed to the well-known simplifying assumptions of Ritter's theory, such as the absence of resistance and instantaneous opening of the gate.

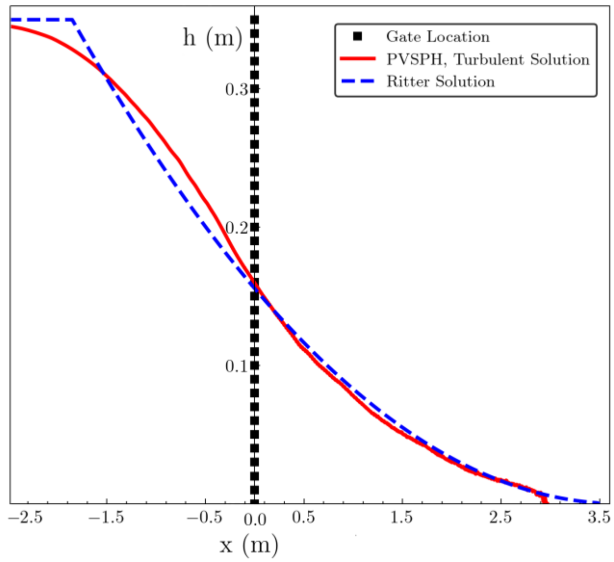

Figure 4. 33. Comparison of water surface profile for analytical solution and PVSPH Turbulent solution (water) at t =1.0 s

Figure 4.34 compares the water surface profiles at t =1.5s of the PVSPH simulations to the analytical Ritter solution. The water surface level at the gate section for the analytical solution is 0.1556m, while for Newtonian turbulent fluid, it is equal to 0.1576m, indicating that the model accurately represents the phenomenon. Furthermore, the water surface profiles for the range from t = 0.1s to t = 1.5s are shown in Figure 4.35.

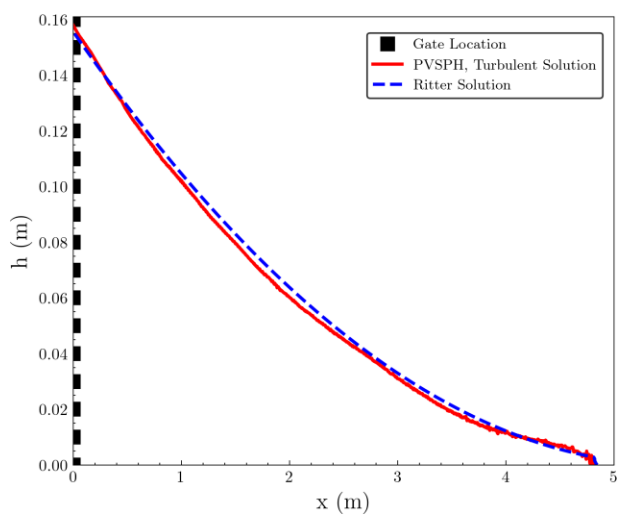

Figure 4. 34. Comparison of water surface profile for analytical solution and PVSPH water turbulent solution at t=1.5s

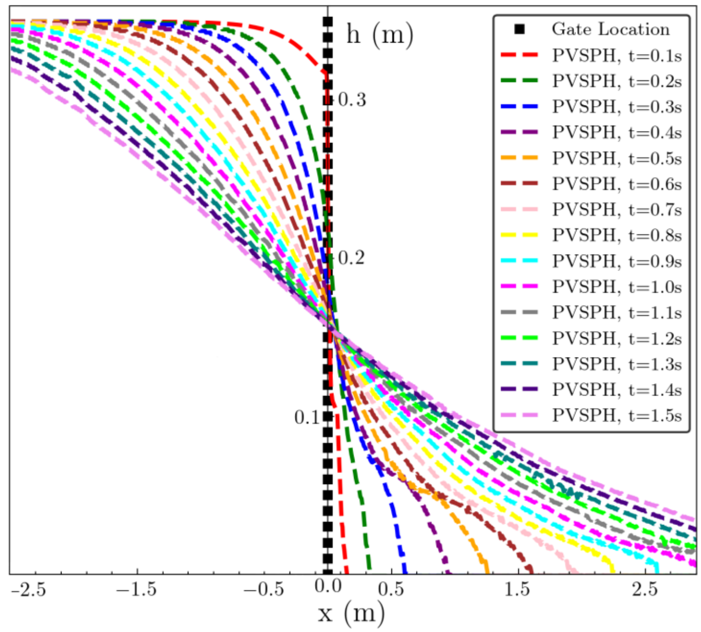

Figure 4. 35. Water surface profile for PVSPH water turbulent solution at various instants (0.1 s to 1.5 s)

Figure 4.36 shows the time evolution of the discharge at the gate section, simulated with the PVSPH and EDAM models, compared with the Ritter's solution and the experimental values for the initial period (t < 2s). The result of EDAM is identical to the Ritter solution, because in both cases an instantaneous opening of the gate is assumed. The PVSPH result exhibits a similar pattern with respect to the experimental data, with a peak at t = 0.17s and a tendency to reach a constant discharge for t >1s, which tends to the analytical solution. However, both the maximum and asymptotic values appear to be slightly lower than the experimental measurements, as indicated by the RMSE value of 14.11%.

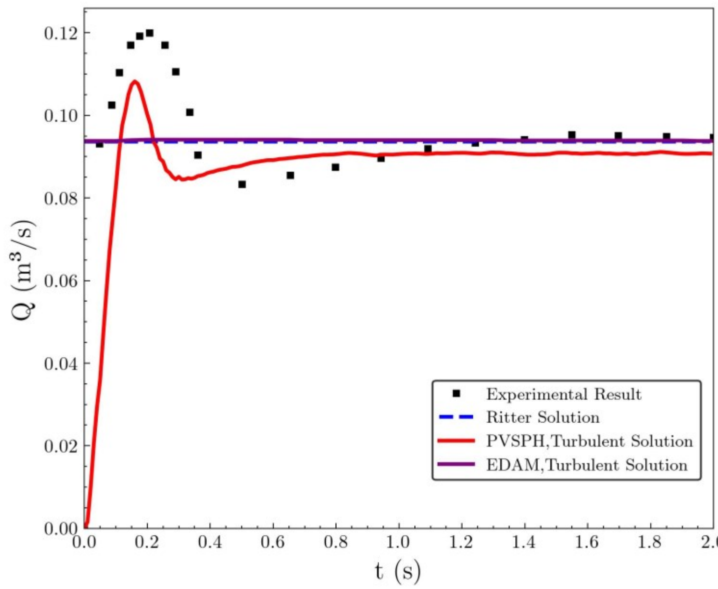

Figure 4. 36. Time evolution of the flow rate at the gate section: experimental data, analytical Ritter solution, PVSPH solution, and EDAM solution

Figure 4.37 reports the time evolution of the discharge at section x=5.146m, obtained with the PVSPH and EDAM model compared with the Ritter's solution and the experimental data. The PVSPH model exhibits a similar trend to the experimental results, with a slight delay and an underestimation of the discharge values for t >1s. The discrepancy in the discharge for t >1s is reflected in the RMSE value of 15.35%, showing a reasonable but noticeable deviation from experimental measurements. The discrepancy in the discharge for numerical PVSPH results is quantified by the mean RMSE value of 17.01%, showing a reasonable but noticeable deviation from the analytical solution. Moreover, the result of EDAM model is closer to analytical solution.

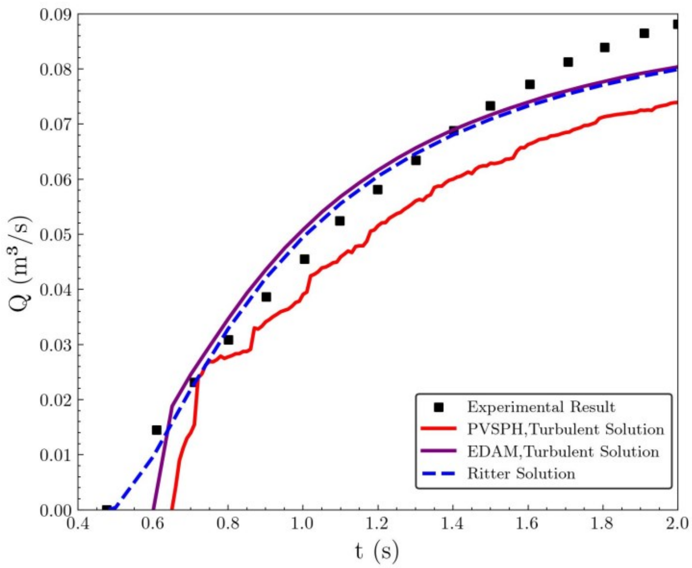

Figure 4. 37. Time evolution of the flow rate at the downstream section x = 5.146m: comparison between experimental data and PVSPH results

Figure 4.38 illustrates the temporal evolution of water depth at x =5.35m, x =6.44m, and x =9.05m, as simulated by the PVSPH model and compared with the corresponding experimental data. The results show satisfactory agreement; however, the PVSPH model slightly underestimated the maximum water depth, with RMSE percentages of 14.8% at x =5.35m, 10.48% at x =6.44m, and 25.88% at x =9.05m.

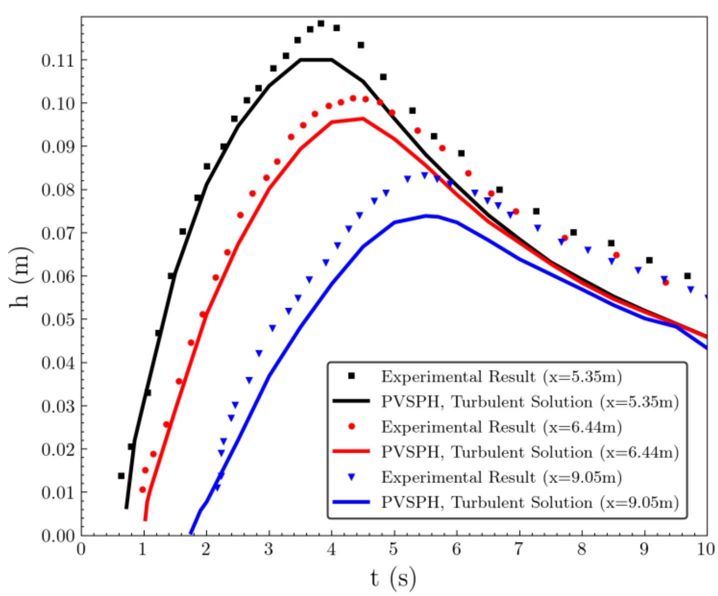

Figure 4. 38. Time evolution of the water depth at the various downstream sections: comparison between experimental data and PVSPH results

Figure 4.39 shows the water depth hydrograph at the gate section, generated using the PVSPH and EDAM models, and compared with both the Ritter solution and experimental results. The model output closely aligns with the EDAM solution and experimental data, showing a mean percentage error of 7.83%. The difference after 3 seconds is due to the assumption of an infinite reservoir in the analytical method. Figure 4.40 presents snapshots of the velocity magnitude fields at different time intervals, also displaying the removal gate.

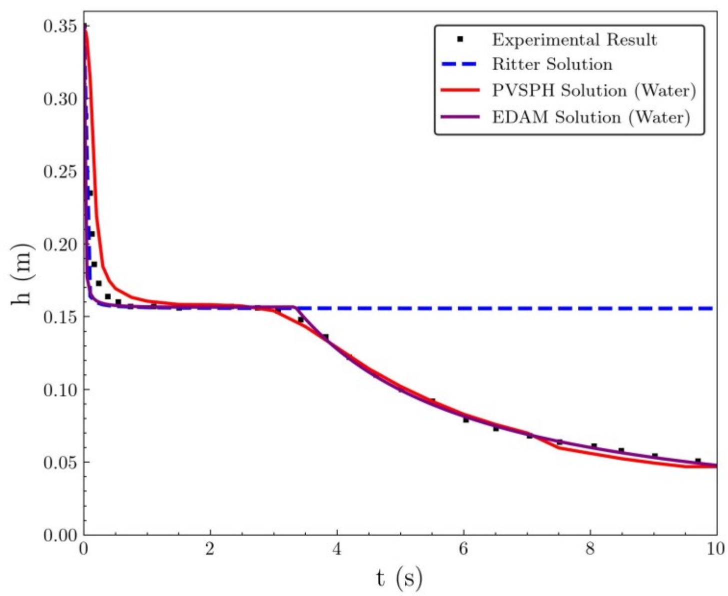

Figure 4. 39. Time evolution of the water depth at gate section (open-end): comparison between experimental results and PVSPH, EDAM and Ritter solutions

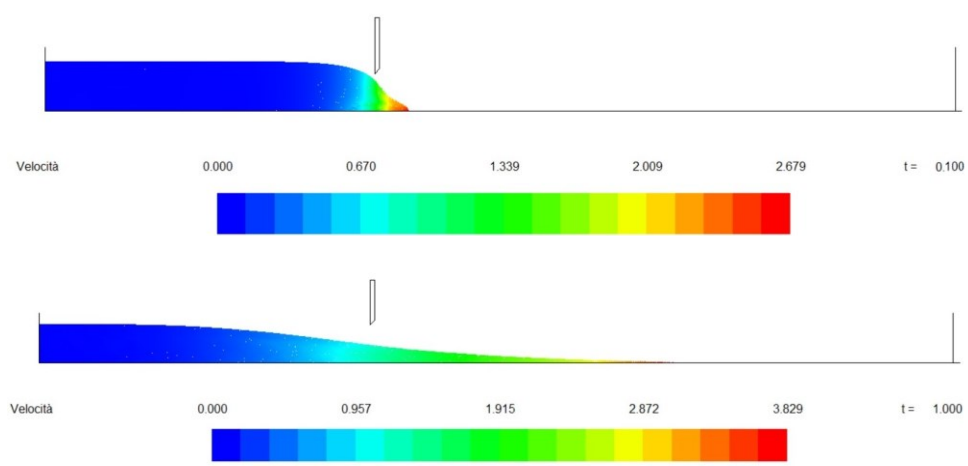

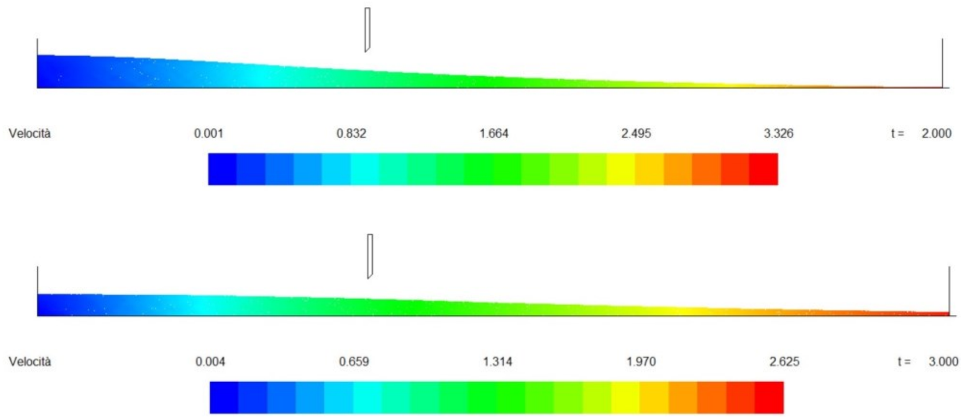

Figure 4. 40. The velocity magnitude fields for water at different time intervals (t = 0.1s, t = 1s, t = 2s, and t = 3s) (open-end)

4.2.1.3. Water dam-break: horizontal bed closed-end configuration

To study the reflection of the dam-break wave against the wall, the closed-end flume configuration is employed (Figure 4.30a). Figure 4.41 shows the temporal evolution of the water depth, obtained at the gate section with the PVSPH model, compared with the EDAM, EDRAM solutions, and available experimental data. In general, there is very good agreement between the models. The wave reflection for the experimental data and EDRAM occurs after 8.7s, whereas for PVSPH and EDAM, it occurs with a slight delay, around 9s. Moreover, the PVSPH model underestimates the maximum water depth by approximately 7.5%, which is lower than the other models. Overall, a good agreement between the experimental and PVSPH results is observed, with a mean percentage error of 12.96%.

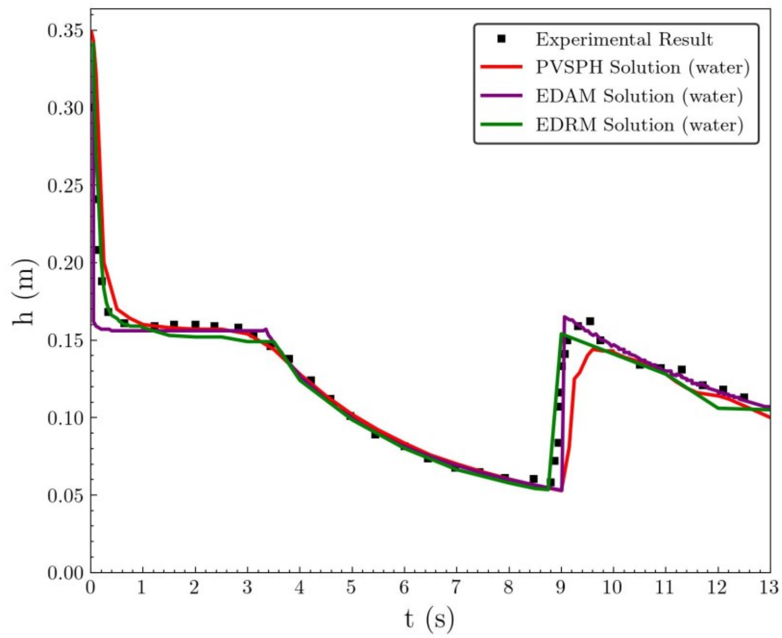

Figure 4. 41. Time evolution of the water depth at gate section (closed-end): comparison between experimental results and PVSPH, EDAM and EDRM solutions

4.2.1.4. Water dam-break: horizontal bed inverse slope configuration

To assess the impact of a reverse slope bed in a dam-break, the scheme in Fig. 4.30b is considered. Figure 4.42 reports the time evolution of the water depths at the channel slope change section for the Newtonian model, superimposed on the experimental results. The simulated water depth clearly captures the advancing front and the first reflection due to the reverse slope. At t = 3.8s, a rapid increase in water depth is observed, caused by the wave reflected from the counter slope. The model represents the experimental behavior, with an overall RMSE = 12.8% (expressed as a percentage of the maximum water depth). However, the most critical feature-the maximum water depth-is predicted with excellent precision. The maximum water depth estimated by the SPH model nearly matches the experimental observation, with a relative percentage error between the peaks of only 0.05%, although showing a delay of about 0.6 s. To better visualize the propagation of the reflected wave from inverse slope, Figure 4.43 illustrates the magnitude velocity fields for water at different time intervals.

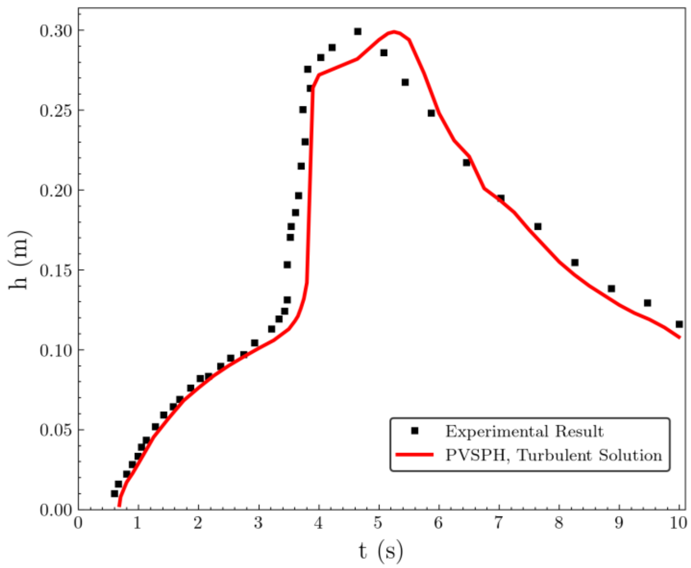

Figure 4. 42. Time evolution of water depth at changing slope section (inverse slope): comparison between experimental data and PVSPH results

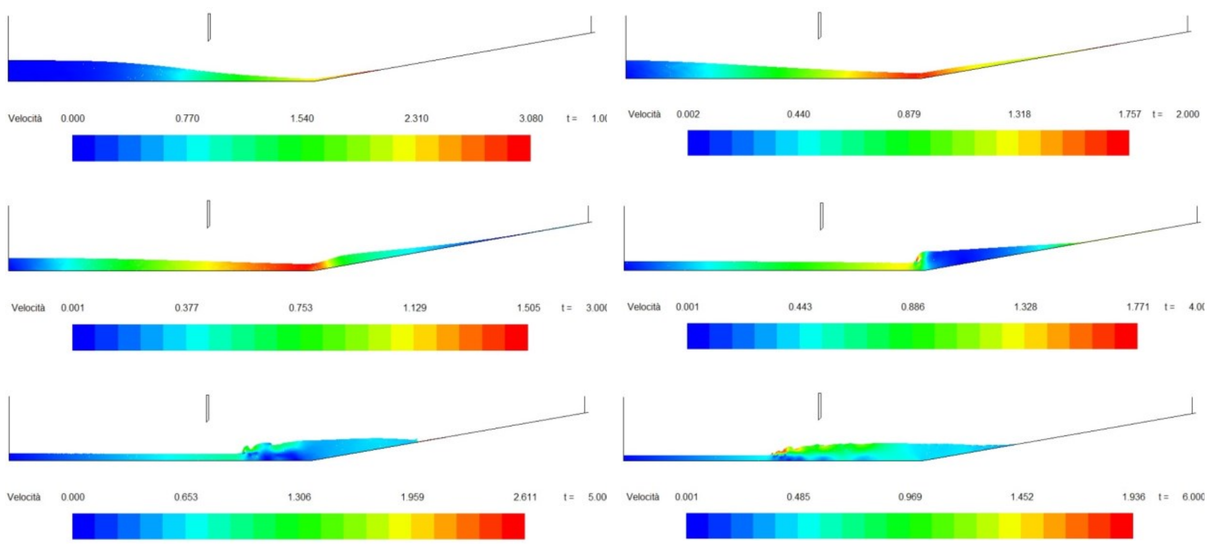

Figure 4. 43. The velocity magnitude fields for the water at different time intervals (t = 1s to t = 6s) (inverse slope)

4.2.2. Mudflow dam-break simulations

This section evaluates the performance and accuracy of the PVSPH model for non-Newtonian fluids, comparing its results with EDAM and EDRM solutions.

The non- Newtonian fluid is assumed to follow the rheological model proposed by Ng and Mei (1994), in which the rheological parameters, consistency κ and the rheological index n, are related to the solid fraction concentration through the following relationships valid for kaolinite suspensions:

$$\kappa = 1.86*10^{-5}C_v^{4.45} \tag{4.9}$$

$$n = 5.86\ C_v^{-1.34} \tag{4.10}$$

$$\rho = \left(1 - \frac{C_v}{100}\right)\rho_l + \frac{C_v}{100} * \rho_s \tag{4.11}$$

where κ is expressed in $Pa.s^n$ and C_v the solid fraction concentration in percentage. The mixture density has been calculated from eq. 4.11, with the density of the liquid and solid fraction ρ_l=1000 kg/m^3 and ρ_s=2620 kg/m^3, respectively. Table 4.9 reports rheological parameter for different solid volume concentration Cv. Non-Newtonian dam-break tests were conducted using three shear-thinning kaolinite suspensions at different volume concentrations: 20.9%, 12.4%, and 7.41%, corresponding to n =0.1, 0.2 and 0.4.

Table 4. 9. Parameters of the power-law kaolinite suspensions (Ng and Mei, 1994)

n	C_v (%)	ρ (Kg/m3)	κ ($Pa.s^{n-2}$)	Re_c
0.05	34.99	1566.40	138.10	413.99
0.1	20.9	1337.66	13.82	435.23
0.2	12.4	1201.29	1.38	461.83
0.3	9.19	1148.74	0.36	479.14
0.4	7.41	1119.99	0.14	491.78
0.5	6.27	1101.59	0.066	501.52

To determine the flow regime in a power-law fluid, the following Reynolds number can be calculated (Darby, 1988):

$$Re = \frac{\rho\, u^{2-n} h^n}{\kappa} \tag{4.12}$$

where u is the average flow velocity and h the water depth. To guarantee laminar conditions, the Reynolds number needs to remain below a critical Reynolds number, which is given by (Ng and Mei, 1994):

$$\mathrm{Re_c} = 0.125\left(\frac{1+3n}{2n}\right)^n [2100+875(1\text{-}n)] \tag{4.13}$$

Before simulating the dam-break with different rheological indices, it is essential to determine the flow regime by calculating the Reynolds number. In Fig. 4.44, the evolution of Reynolds numbers at the gate section are presented for the initial instants after the gate removal for the three considered non-Newtonian fluids and compared with the critical value (Eq. 4.13). As observed, the Reynolds number reaches its peak value shortly after the gate removal, around 1.0s, indicating a sudden increase in velocity. The Reynolds number remains relatively constant thereafter, following a linear trend in the simulation. Notably, for n =0.4, representing a relatively low viscosity, the highest Reynolds number is observed, while the most viscous fluid (n =0.1) exhibits the lowest Reynolds number. For n =0.2, the flow oscillates between laminar and turbulent, showing transitional behaviour, within the time range of 0.15 to 4.0s. This suggests that the results for n =0.2 should be treated with more suspicion. Additionally, for the higher rheological index (n =0.4), the flow remains completely turbulent and, since no specific modelling for turbulent flow was adopted in the SPH model, it is not considered.

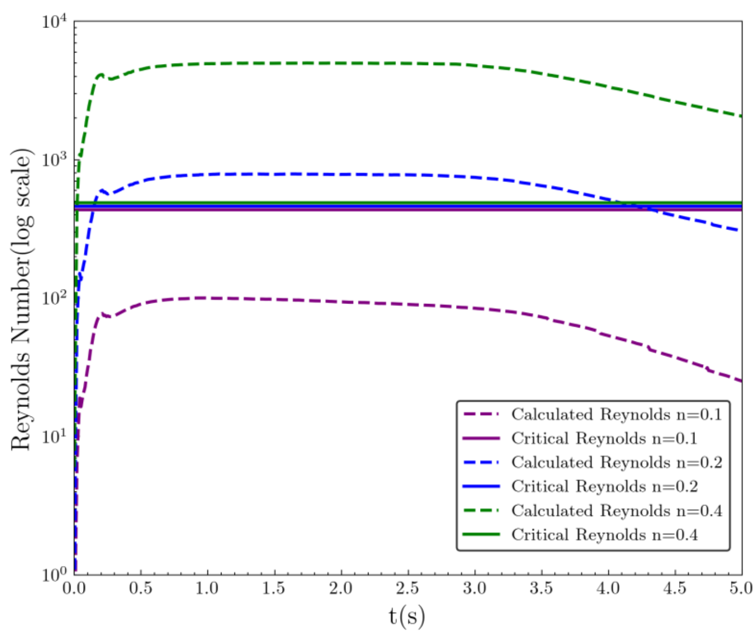

Figure 4. 44. Time evolution of the Reynolds number for non-Newtonian fluid with various values of the rheological index, compared with the related critical Reynolds number value (logarithmic scale)

4.2.2.1. Mudflow dam-break: horizontal bed open-end configuration

Figure 4.45 illustrates the fluid surface profile at t =1.5s obtained with the PVSPH model for water and the two considered non-Newtonian fluids. At the gate section, the water surface level for water is 0.1576 m, while for non-Newtonian shear-thinning fluids (n = 0.1, 0.2), the water depth ranges between 0.1580 and 0.1583 m, consistently being slightly higher than the Newtonian case (Figure 4.45). The non-Newtonian fluids with higher rheological indice (n =0.2) exhibit greater wave propagation speeds. The higher viscosity in the bulk flow dominates the non-Newtonian flow, although the fluid viscosity decreases in the near-wall boundary layer owing to the shear-thinning rheological behaviour.

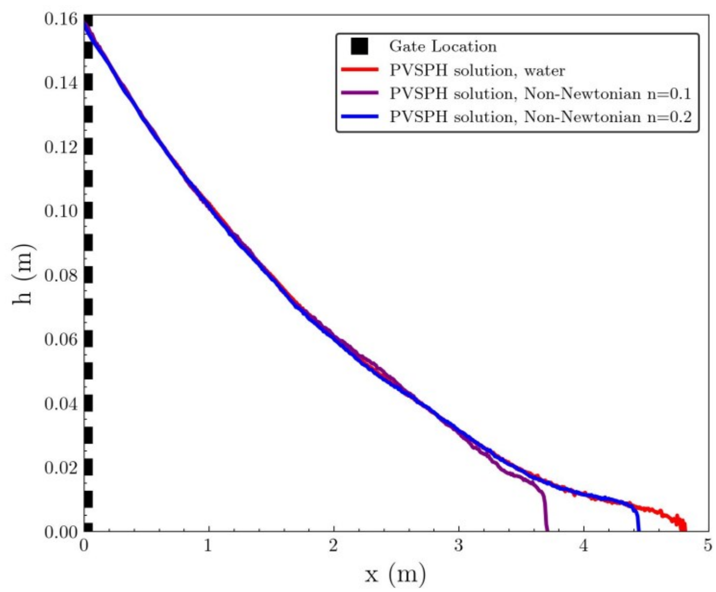

Figure 4.45. Fluid surface profile at t =1.5s from the PVSPH for water and the two considered non-Newtonian fluids

In Fig. 4.46 and 4.47 reports the discharge hydrograph obtained with the PVSPH model for water and the two considered kaolinite suspensions at the gate section and at x = 5.146m, respectively. Shear-thinning fluids behave similarly to water, even if the fluid n =0.1 exhibits smaller flow rate. The reduction in the dam-break wave propagation celerity is also evident in the downstream section (Fig. 4.50): the wave reaches the section at much later times compared to the water case.

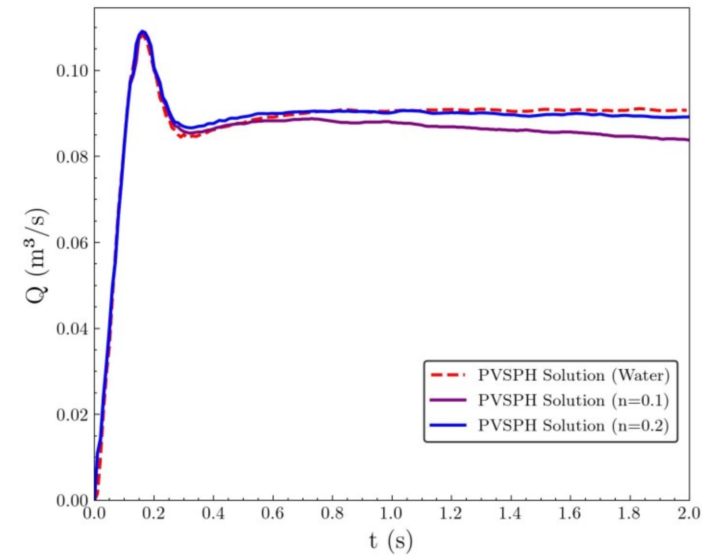

Figure 4. 46. Time evolution of the flow rate at the gate section from the PVSPH for water and the two considered non-Newtonian fluids

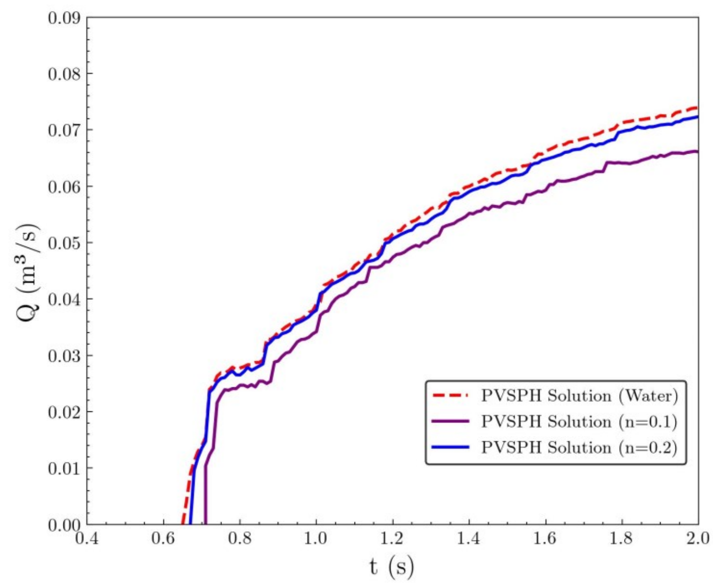

Figure 4. 47. Time evolution of the flow rate at the downstream section (x = 5.146m) from the PVSPH for water and the two considered non-Newtonian fluids

Figure 4.48 shows the time evolution of the water depth at the gate section for power-law fluids with n =0.1 (a) and n =0.2 (b), reproduced using the PVSPH and EDAM models, in comparison to the PVSPH water results. The shear-thinning fluids with the lower n value (Fig. 4.48a) exhibit a smooth wave, with the predicted depth values from PVSPH, EDAM, and the Newtonian case (water) aligning closely. Specifically, PVSPH predicts a slightly higher water depth than the EDAM model, with a mean percentage error of 7.02%. However, for the lower-viscosity fluid (Fig. 48b), the PVSPH solution closely matches the EDAM results with a very low mean percentage error of 2.02%.

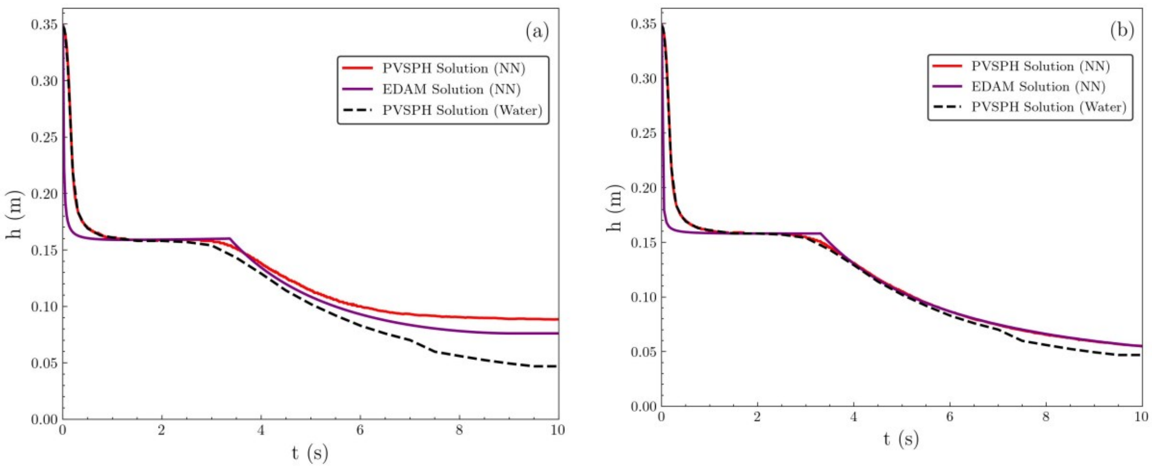

Figure 4. 48. Time evolution of the fluid depth at the gate section from PVSPH and EDAM, compared with PVSPH water results. n =0.1 (a); n =0.2 (b)

To visualize the fluid motion at different times after the gate removal, snapshots of the velocity magnitude field for the non-Newtonian fluid with n =0.1 are presented in Fig. 4.49.

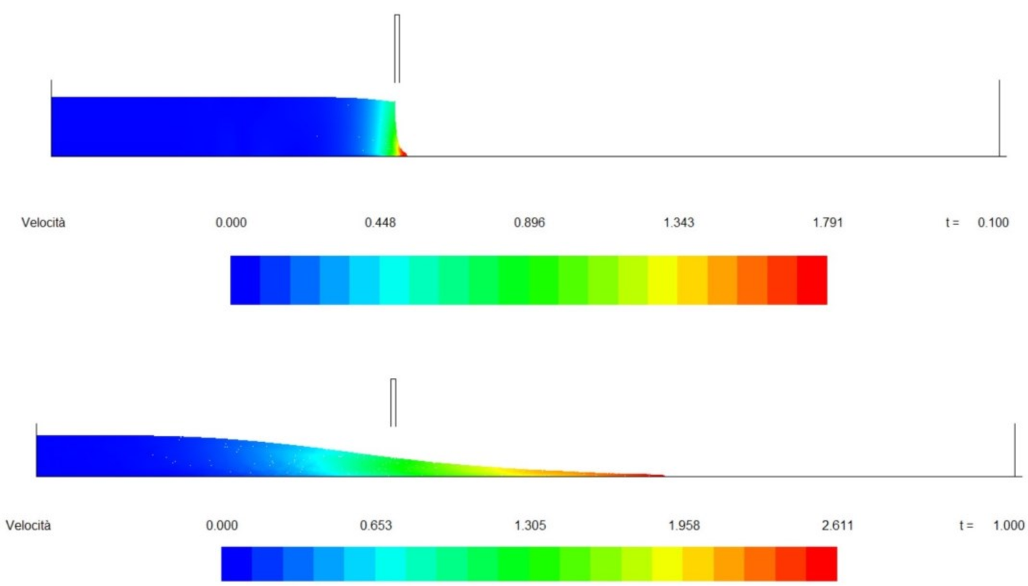

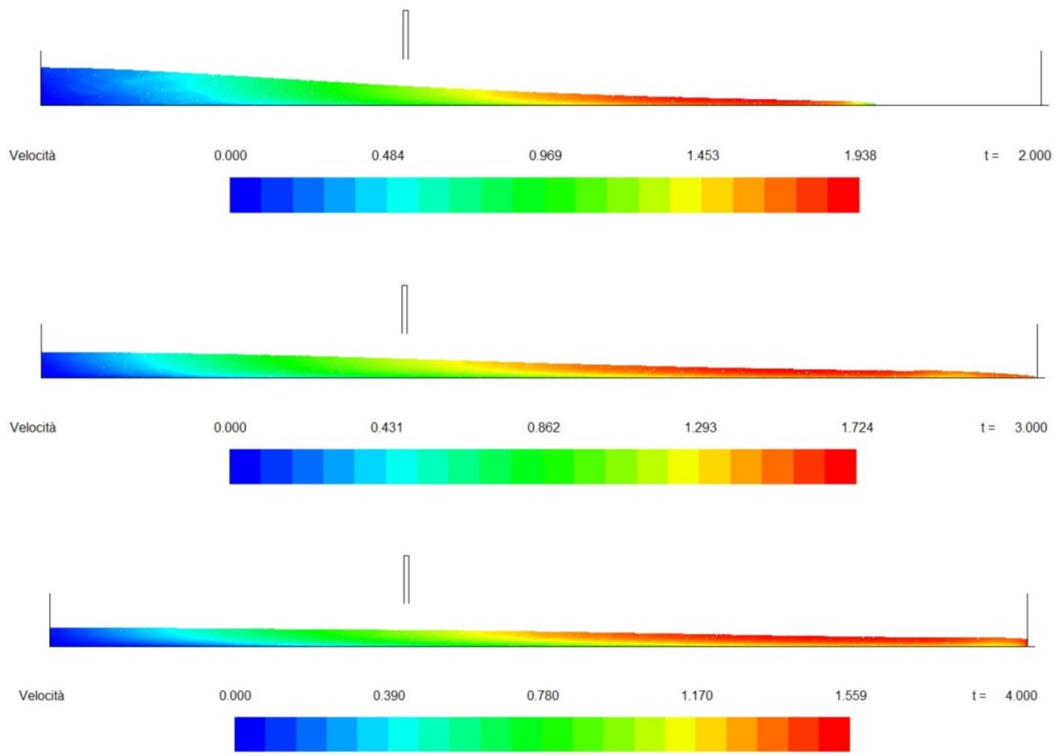

Figure 4. 49. The velocity magnitude fields for non-Newtonian fluid (n =0.1) at different time intervals (t = 0.1s, t = 1s, t = 2s, t = 3s, and t = 4s) (open-end)

4.2.2.2. Mudflow dam-break: horizontal bed closed-end configuration

For horizontal bed configuration, Fig. 4.50 shows the time evolution of the fluid depth at the gate section for the power-law fluids with n = 0.1 (Fig. 4.50a) and n = 0.2 (Fig. 4.50b), reproduced with PVSPH, EDAM and EDRM models. For the sake of comparison, in the same figures the results of PVSPH with water (in turbulent conditions) are also reported. The arrival time of the reflected wave for the n = 0.1 fluid is higher compared to water. Moreover, it is slightly lower for the EDAM (9.11 s), with respect to PVSPH (9.5 s) and EDRM (9.4 s), for which it is quite similar (Fig. 4.50a). The height of the reflected wave is similar to the one of the water case and the numerical solutions of PVSPH, EDAM, and EDRM models exhibit a similar trend. For the power-law fluid with n = 0.2, the predicted peak depth is higher compared to n = 0.1 case, while the reflected wave arrives earlier with an arrival time similar to the one of water. In particular, the PVSPH predicts the arrival at 9.2 s, later respect to EDAM (9.04 s) and EDRM (8.8 s). So, the results highlight the influence of fluid rheology on both the peak water height and the reflected wave's arrival time. Overall, despite these minor differences between the models, the agreement between the methods yields satisfactory results.

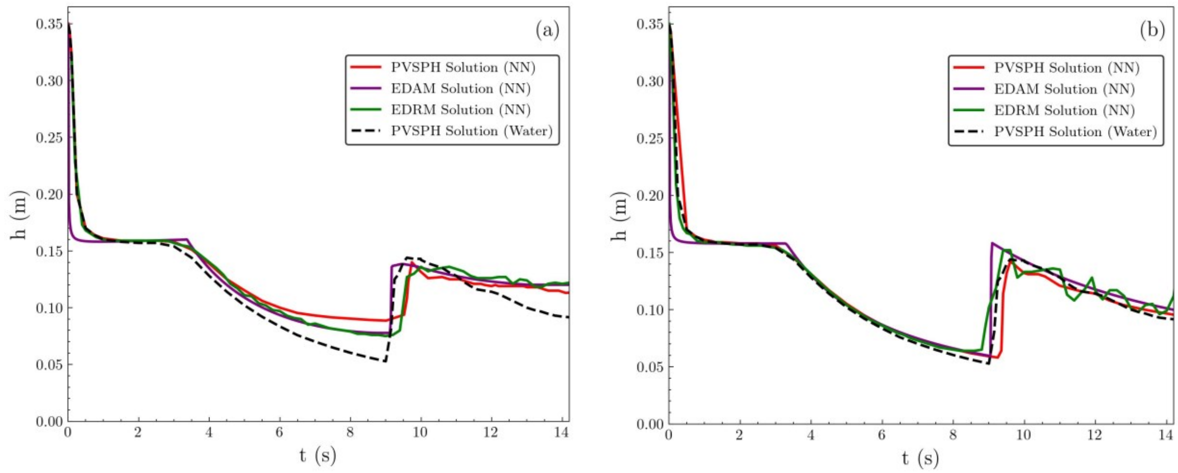

Figure 4. 50. Time evolution of the fluid depth at the gate section from PVSPH, EDAM, and EDRM and the PVSPH water results. n = 0.1 (a); n = 0.2 (b)

Figure 4.51 presents the time evolution of the fluid depth for power-law fluids with n = 0.1 (Fig. 4.51a) and n = 0.2 (Fig. 4.51b) at x = 5.146 m, simulated using the three considered models, alongside the turbulent Newtonian water case reproduced with the PVSPH model as reference. It can be observed that the return-wave height for n = 0.2 is significantly higher (over 20%) than that obtained for the n = 0.1 fluid across all models. In both cases, the time taken for the reflected fluid to reach the considered section, located 1.78 m downstream of the gate, is approximately 8 seconds. Moreover, the trends predicted by all three models (PVSPH, EDAM, and EDRM) for the fluid behavior up until that section are very close. However, after this time, when the reflected wave causes a rise of the water depth at that section, the models begin to show different behaviors. For the n = 0.2 fluid, the dynamic behavior appears noticeably closer to that of the Newtonian fluid. In this case, the EDRM and EDAM model exhibit a higher peak value compared to the PVSPH models. The larger differences observed for the fluid with n = 0.2 could be attributed to its more transient and oscillatory behavior. Despite these minor differences, there is a general agreement among the models in yielding satisfactorily consistent results.

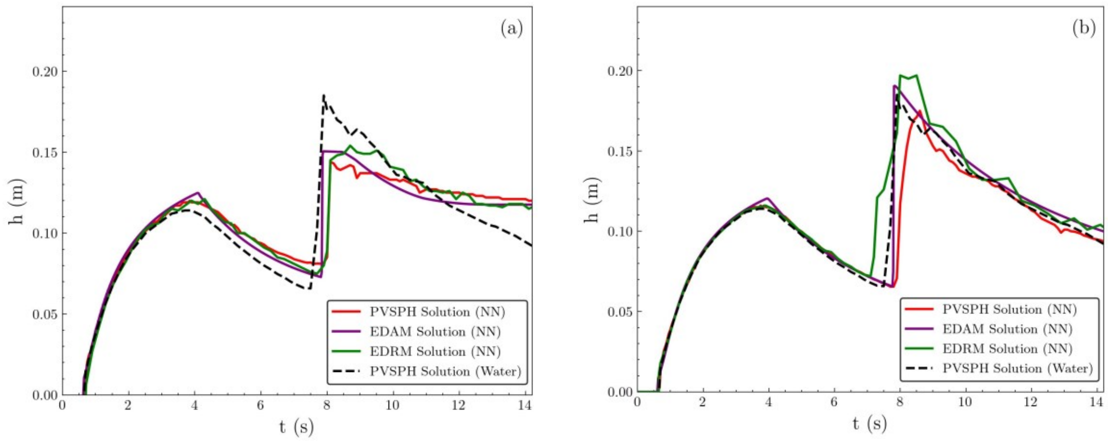

Figure 4. 51. Time evolution of the fluid depth at x = 5.146m from PVSPH, EDAM, and EDRM and the PVSPH water results. n = 0.1 (a); n = 0.2 (b)

4.2.2.3. Mudflow dam-break: horizontal bed inverse slope configuration

Considering the inverse slope scheme (Fig. 4.30b), Figure 4.52 reports the temporal evolution of the fluid depth for n = 0.1 and n = 0.2, obtained at the gate section using the EDAM, EDRM, and PVSPH models, as well as the SPH results for water. For the power-law fluids, the reflected wave occurs earlier compared to the water case in both figures. For the power-law fluid with n =0.1, the trends in the simulations across the EDAM, EDRM, and PVSPH models are quite similar. The peak values of the flow depth predicted by these models do not show significant differences, with the maximum difference being around 6%, primarily attributed to the EDAM model. For the less viscous fluid case (n = 0.2), the differences between the models become noticeable. However, the peak flow-depth values predicted by the models remain similar.

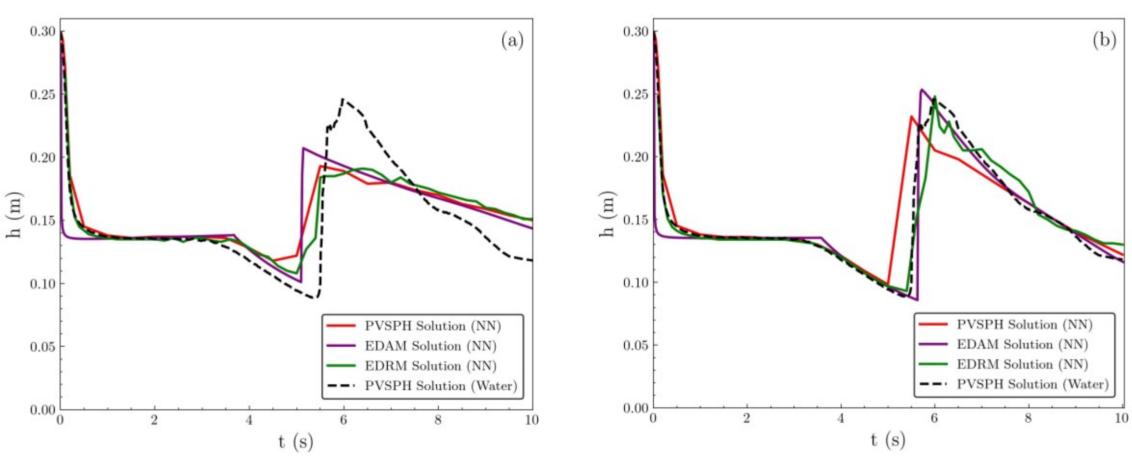

Figure 4. 52. Time evolution of the fluid depth at gate section from PVSPH, EDAM, and EDRM and the PVSPH water results (n = 0.1 (a); n = 0.2 (b))

Figure 4.53 reports the temporal evolution of the fluid depth for the case n = 0.1 (Fig. 4.53a) and n = 0.2 (Fig. 4.53b), obtained at the slope change section using the EDAM, EDRM, and PVSPH models, along with the PVSPH results for water. For both fluids, all models successfully reproduce the increase in depth at 3.2 s and 4 s for n = 0.1 and n = 0.2, respectively. For power-law fluids with n = 0.1, the reflected wave arrives earlier compared to the water case. All the models predict similar peak values of about 0.26 m, with a maximum percentage difference of 3.3% between the EDAM and PVSPH models. For the n = 0.2 fluid, the arrival time of the reflected wave is undistinguishable from the corresponding clear-water case. Additionally, the EDRM model exhibits slight fluctuations, and the EDAM model shows a higher peak compared to the other models. The differences in the peak values of the flow depth are relatively small, as well: difference between EDAM and PVSPH is 10.35%, while the value predicted by EDRM differs from the corresponding of PVSPH for 2.93%.

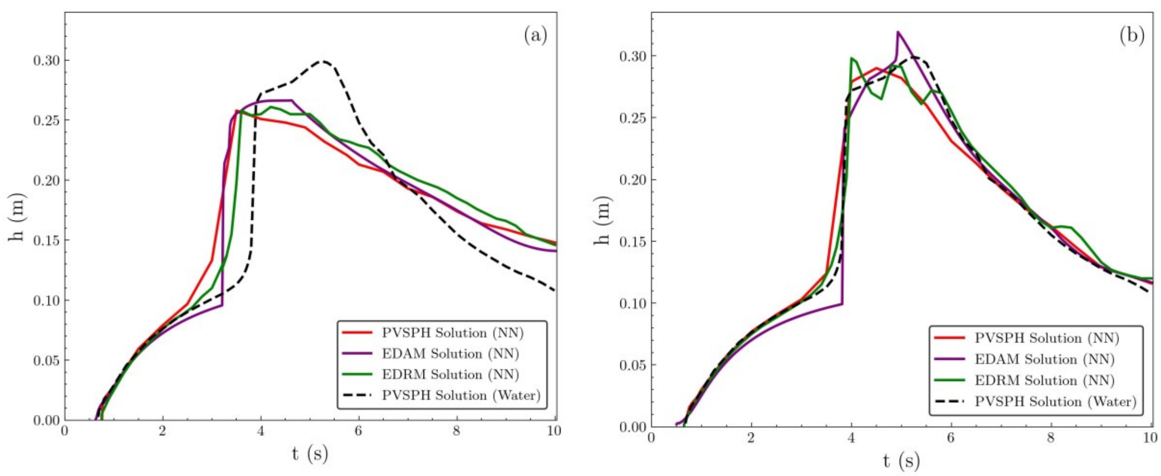

Figure 4. 53. Time evolution of the fluid depth at changing slope section from PVSPH, EDAM, and EDRM and the PVSPH water results (n =0.1 (a); n =0.2 (b))

Figure 4.54 presents the fluid depth profile at t= 3.8 s after gate opening for a power-law fluid n=0.1, comparing the results from the PVSPH, EDAM, and EDRM models with the water. The figure shows that all models follow similar trends, with a reflected wave occurring at x=4.71m after the gate. However, the reflected wave from the slope for the water case occurs near the changing slope section. The EDAM model underestimates the maximum wave height by approximately 20% compared to the PVSPH and EDRM models.

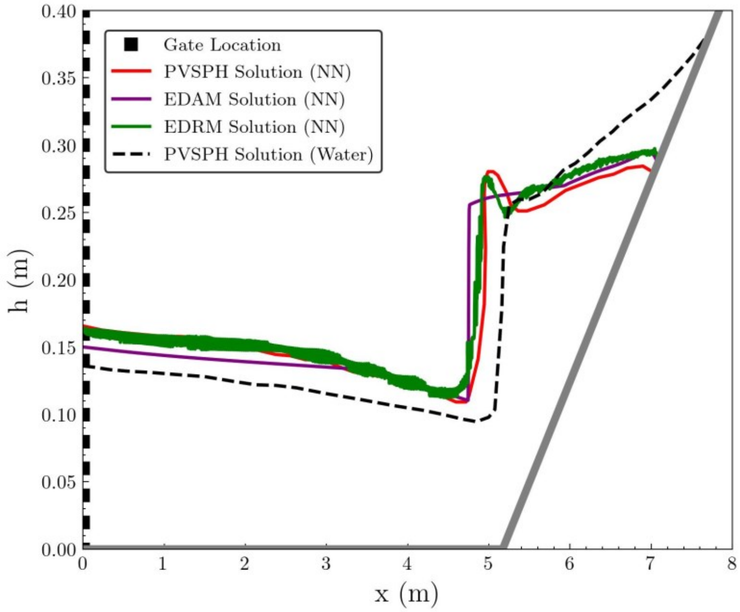

Figure 4. 54. Fluid depth profile at t = 3.8s after gate opening for a power-law fluid (n = 0.1) (inverse slope): comparison between PVSPH, EDAM, EDRM and water

4.3. Experimental study

A comprehensive set of dam-break flow experiments was conducted at the Mechanics Laboratory of the University of Zaragoza, Spain. The experimental setup consisted of a flume with two different slopes (0° and 4.65°). The experiments were performed using water and two non-Newtonian fluids, characterized by the Herschel-Bulkley rheology (Eq.3.1). Table 4.10 presents a summary of the characteristics of the non-Newtonian fluids.

Table 4. 10. Properties and rheology of the shear-thinning fluid

	τ_y*(Pa)*	μ *(Pa · s*^{m}*)*	*m*	*ρ (kg/m*^{3}*)*	*PH*
Original rheology	23.75	4.01	0.47	~1000	7.2
Second rheology	11.94	2.26	0.5	~1000	7.2

where, ρ is the fluid density (kg/m^3) and PH represents the potential of hydrogen (dimensionless), indicating the acidity or alkalinity of the solution.

The testing conditions included both dry-bed and wet-bed scenarios, with downstream depths of 0.01 and 0.018 m, under both open-end and closed-end configurations. Additional trials were performed with a semi-cylindrical obstacle installed on the middle of the flume bed. Five upstream reservoir depths were tested: 0.08 m, 0.10 m, 0.12 m, 0.14 m, and 0.16 m. Furthermore, the reservoir volume was adjusted using a dividing plate, allowing experiments to be carried out with either the full capacity or two-thirds of the volume. In total, 56 distinct tests were conducted, and the complete experimental details are provided in Table 4.11.

Table 4. 11. Overview of experimental parameters

Test number	Flume slope	Fluid	Reservoir volume	Upstream depth (m)	Test description
1	Horizontal	Original Rheology	Entire reservoir	0.08	Dry-bed & Open-end
2	Horizontal	Original Rheology	Entire reservoir	0.1	Dry-bed & Open-end
3	Horizontal	Original Rheology	Entire reservoir	0.12	Dry-bed & Open-end
4	Horizontal	Original Rheology	Entire reservoir	0.14	Dry-bed & Open-end
5	Horizontal	Original Rheology	Entire reservoir	0.14	Wet-bed (0.018m) & Open-end
6	Horizontal	Second Rheology	Entire reservoir	0.08	Dry-bed & Open-end
7	Horizontal	Second Rheology	Entire reservoir	0.1	Dry-bed & Open-end
8	Horizontal	Second Rheology	Entire reservoir	0.12	Dry-bed & Open-end
9	Horizontal	Second Rheology	Entire reservoir	0.12	Wet-bed (0.018m) & Open-end
10	Horizontal	Second Rheology	Entire reservoir	0.12	Dry-bed & Open-end & Obstacle
11	Horizontal	Second Rheology	Entire reservoir	0.12	Wet-bed (0.018m) & Open-end & Obstacle
12	Horizontal	Second Rheology	Entire reservoir	0.14	Dry-bed & Open-end
13	Horizontal	Second Rheology	Two-thirds of the reservoir	0.08	Dry-bed & Open-end
14	Horizontal	Second Rheology	Two-thirds of the reservoir	0.1	Dry-bed & Open-end
15	Horizontal	Second Rheology	Two-thirds of the reservoir	0.1	Dry-bed & Closed-end
16	Horizontal	Second Rheology	Two-thirds of the reservoir	0.1	Dry-bed & Open-end & Obstacle
17	Horizontal	Second Rheology	Two-thirds of the reservoir	0.1	Wet-bed (0.01m) & Open-end
18	Horizontal	Second Rheology	Two-thirds of the reservoir	0.12	Dry-bed & Open-end
19	Horizontal	Second Rheology	Two-thirds of the reservoir	0.12	Dry-bed & Closed-end
20	Horizontal	Second Rheology	Two-thirds of the reservoir	0.12	Wet-bed (0.01m) & Open-end
21	Horizontal	Second Rheology	Two-thirds of the reservoir	0.12	Wet-bed (0.018m) & Open-end
22	Horizontal	Second Rheology	Two-thirds of the reservoir	0.12	Dry-bed & Open-end & Obstacle
23	Horizontal	Second Rheology	Two-thirds of the reservoir	0.14	Dry-bed & Open-end
24	Horizontal	Second Rheology	Two-thirds of the reservoir	0.14	Dry-bed & Closed-end
25	Horizontal	Second Rheology	Two-thirds of the reservoir	0.14	Wet-bed (0.01m) & Open-end
26	Horizontal	Second Rheology	Two-thirds of the reservoir	0.14	Dry-bed & Open-end & Obstacle
27	Horizontal	Second Rheology	Two-thirds of the reservoir	0.16	Dry-bed & Open-end
28	Horizontal	Second Rheology	Two-thirds of the reservoir	0.16	Dry-bed & Closed-end
29	Horizontal	Second Rheology	Two-thirds of the reservoir	0.16	Wet-bed (0.01m) & Open-end
30	Horizontal	Second Rheology	Two-thirds of the reservoir	0.16	Dry-bed & Open-end & Obstacle
31	Horizontal	Water	Entire reservoir	0.12	Dry-bed& Open-end

32	Horizontal	Water	Entire reservoir	0.12	Dry-bed& Closed-end
33	Horizontal	Water	Entire reservoir	0.12	Wet-bed (0.01m) & Open-end
34	Horizontal	Water	Entire reservoir	0.12	Wet-bed (0.018m) & Open-end
35	Horizontal	Water	Entire reservoir	0.12	Dry-bed& Open-end & Obstacle
36	Horizontal	Water	Entire reservoir	0.16	Dry-bed& Open-end
37	Inclined	Second Rheology	Entire reservoir	0.08	Dry-bed& Open-end
38	Inclined	Second Rheology	Entire reservoir	0.1	Dry-bed& Open-end
39	Inclined	Second Rheology	Entire reservoir	0.12	Dry-bed& Open-end
40	Inclined	Second Rheology	Entire reservoir	0.12	Dry-bed& Open-end & Obstacle
41	Inclined	Second Rheology	Entire reservoir	0.14	Dry-bed& Open-end
42	Inclined	Second Rheology	Entire reservoir	0.16	Dry-bed& Open-end
43	Inclined	Second Rheology	Two-thirds of the reservoir	0.08	Dry-bed& Open-end
44	Inclined	Second Rheology	Two-thirds of the reservoir	0.1	Dry-bed& Open-end
45	Inclined	Second Rheology	Two-thirds of the reservoir	0.1	Dry-bed& Closed-end
46	Inclined	Second Rheology	Two-thirds of the reservoir	0.1	Dry-bed& Open-end&Obstacle
47	Inclined	Second Rheology	Two-thirds of the reservoir	0.12	Dry-bed& Open-end
48	Inclined	Second Rheology	Two-thirds of the reservoir	0.12	Dry-bed& Closed-end
49	Inclined	Second Rheology	Two-thirds of the reservoir	0.12	Dry-bed& Open-end&Obstacle
50	Inclined	Second Rheology	Two-thirds of the reservoir	0.14	Dry-bed& Open-end
51	Inclined	Second Rheology	Two-thirds of the reservoir	0.14	Dry-bed& Closed-end
52	Inclined	Second Rheology	Two-thirds of the reservoir	0.14	Dry-bed& Open-end&Obstacle
53	Inclined	Second Rheology	Two-thirds of the reservoir	0.16	Dry-bed& Open-end
54	Inclined	Second Rheology	Two-thirds of the reservoir	0.16	Dry-bed& Closed-end
55	Inclined	Second Rheology	Two-thirds of the reservoir	0.16	Dry-bed& Open-end&Obstacle
56	Inclined	Water	Two-thirds of the reservoir	0.12	Dry-bed& Open-end

4.3.1. Gate Opening Time Assessment

To ensure comparability of the experimental results with analytical and numerical solutions assuming instantaneous gate removal, the gate must open rapidly enough to avoid disturbing the initial wave formation. This requirement is evaluated using the criterion proposed by Lauber and Hager (1998), which expresses that the gate opening time must remain below the characteristic wave propagation time t_c:

$$t_{op} < t_c = \sqrt{\frac{2h_{0.}}{g.cos\theta}} \qquad (4.14)$$

For the initial upstream depth of h_0= 0.12 m, the threshold value is: t_c=0.1564s

Based on the measured maximum gate removal velocity in the laboratory, 0.78 m/s (see Figure 3.2), the resulting opening time is approximately: t_{op}=0.154s.

Since t_{op}<t_c, the gate motion satisfies the Lauber–Hager criterion, confirming that the opening process has a negligible influence on the initial flow evolution for all tests conducted at this removal speed.

4.3.2. Flow regime calculation

To characterize the flow regime of the non-Newtonian fluid, the generalized Reynolds number is calculated using the formulation provided by Darby (1988) (Eq. 4.12). Although this formulation was originally derived for Power-law fluids, it serves as a robust approximation for the Herschel–Bulkley fluid used in this study. Because the yield stress in the Herschel–Bulkley model increases the apparent viscosity relative to a pure Power-law model (thereby decreasing the Reynolds number), the value obtained from the Power-law formulation represents a conservative upper bound. To verify the flow regime prior to the experimental measurements, a representative calculation is performed for a characteristic upstream depth. Calculations are performed for the Second Rheology fluid (see Table 4.10), considering an initial upstream reservoir depth of $h_0 = 0.12$ m. The relevant parameters are determined as follows:

- Maximum velocity: The maximum flow velocity is estimated using Ritter's (1892) analytical solution (Eq. 4.2), yielding $V_{max} = 0.723$ m/s.

- Critical Reynolds number: The stability threshold is computed according to the criterion proposed by Ng and Mei (1994) (Eq. 4.13), resulting in a critical Reynolds number of $Re_c = 501$.

- Apparent viscosity: The apparent viscosity is evaluated using the Herschel–Bulkley constitutive law defined in Eq. (2.63), which accounts for both the yield stress and the consistency index. This results in an apparent viscosity of $\mu_{eff} = 2.903$ Pa.s.

- Calculated Reynolds number: Substituting the derived values into Darby's formulation (Eq. 4.12), the generalized Reynolds number under the experimental conditions is found to be approximately Re ≈ 73.37.

Since the calculated Reynolds number is significantly lower than the critical threshold, the flow is confirmed to remain strictly within the laminar regime, even under this conservative approximation.

4.3.3. Data Analysis and Image Processing Methodology

4.3.3.1. Free-Surface Profile Reconstruction and Depth Analysis

The spatio-temporal evolution of the flow depth was quantified using a high-resolution RGB-D sensing approach. The raw data acquired by the Microsoft Kinect v1 sensor were processed through a post-processing workflow to convert the infrared depth maps into a structured physical representation of the free surface. This workflow was carried out in two primary phases: data pre-processing and synchronization using Python, followed by surface reconstruction and depth calculation using a specialized MATLAB algorithm.

1. Data Pre-processing and Temporal Synchronization

The initial phase involved preparing the raw binary data streams for analysis. A custom Python script was used to decode the Kinect recordings and convert the depth frames into accessible image formats. Precise alignment of the data with the physical initiation of the experiment was essential. The temporal origin (t=0) was established by identifying the exact frame corresponding to the gate-opening mechanism. This was achieved through manual visual inspection of a synchronization LED located within the sensor's field of view. The frame index corresponding to the LED illumination was recorded and used as the reference point for the subsequent depth series.

2. Depth Calculation Algorithm (Offset Method)

The core computation of the flow depth relied on a differential measurement strategy implemented in a custom MATLAB code (developed by S. Martínez-Aranda). Since the Kinect sensor measures the distance from the lens to the nearest surface, the fluid depth could not be obtained directly but was derived through a background-subtraction procedure.

Offset Extraction (Dry-Bed Reference)

Before the flow event, a reference depth map of the empty channel was recorded. This dataset, referred to as the Offset, defined the baseline geometry of the channel bed relative to the sensor.

Point-Cloud Processing

During the flow event, the opacity of the fluid ensured robust reflection of the structured infrared light. The MATLAB algorithm processed the instantaneous point clouds, filtering out scattering noise and outliers.

Surface Reconstruction

The local flow depth at any coordinate was calculated by subtracting the instantaneous distance to the fluid surface from the reference distance to the channel bed. The resulting scattered data points were interpolated onto a structured grid to generate a continuous 3D surface profile, enabling the analysis of wavefront evolution and cross-sectional depth variations (Figure 4.55, test case no. 3).

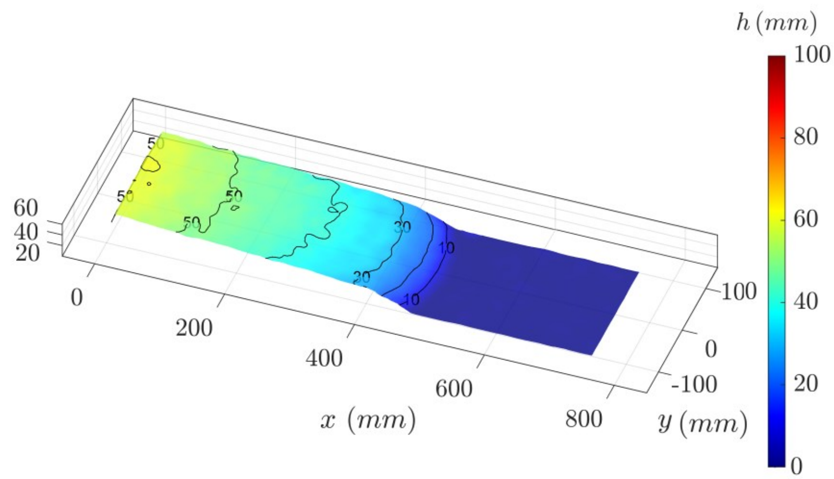

Figure 4. 55. Reconstructed 3D free-surface profile of the non-Newtonian flow

To provide a comprehensive characterization of the non-Newtonian dam-break flow, the experimental campaign analysed the free-surface evolution under varying boundary conditions, bed configurations, and channel inclinations. Longitudinal profiles were extracted along the channel centerline for an initial reservoir depth of 0.12 m.

Figure 4.56 depicts the longitudinal flow-height profiles for the fluid with the original rheology and the second rheology (test case no. 3 and 8). It is observed that both flows exhibit smooth free-surface profiles without the formation of surface instabilities. The lower-viscosity fluid attains a higher velocity and reaches the end of the channel significantly earlier than the more viscous fluid.

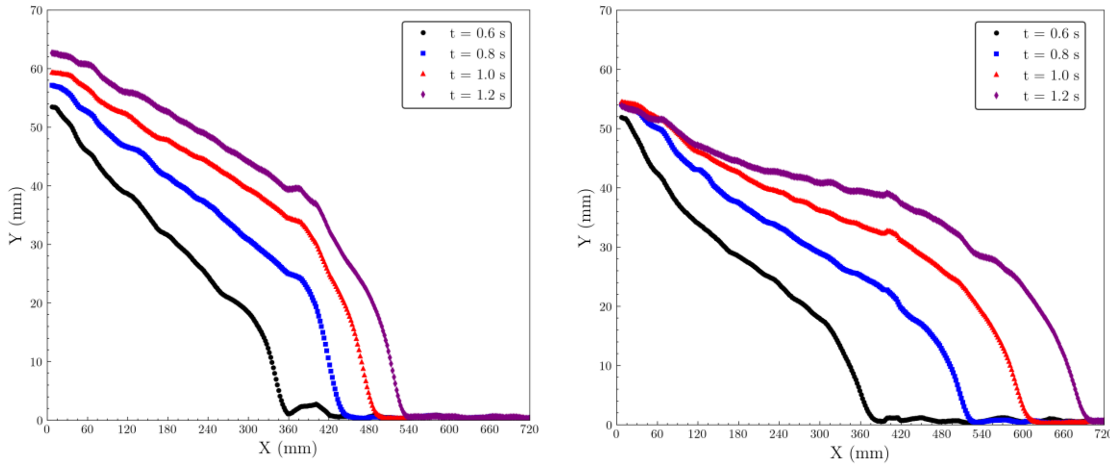

Figure 4. 56. Longitudinal flow-height profiles for the fluid with the original rheology (left) and the second rheology (right)

Figure 4.57 shows the longitudinal flow-height profiles for the wet-bed condition with two downstream depths (test cases no. 8 and 9). Unlike a Newtonian fluid, which develops a rapidly spreading bore and forms a mushroom-like jet in both directions immediately after the gate is opened, this phenomenon is not observed in the non-Newtonian fluid.

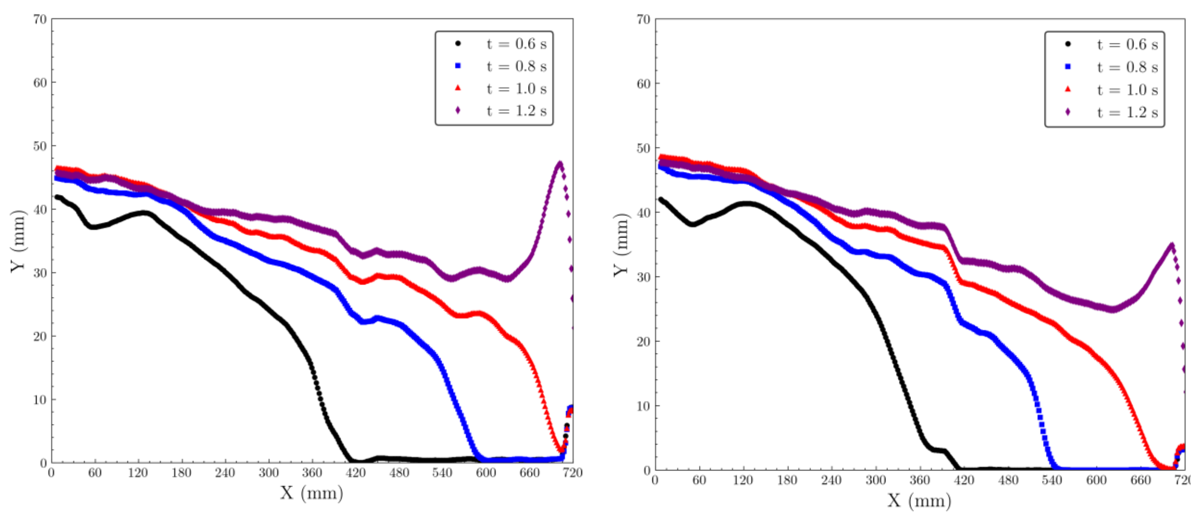

Figure 4. 57. longitudinal flow-height profile fluid for wet-bed condition: 1cm (left), and 1.8 cm (right)

Figure 4.58 illustrates the effect of a semi-cylindrical obstacle placed on the channel bed on the non-Newtonian fluid flow, comparing two different channel inclinations: 0° and 4.65° (test cases no. 22 and 40). The interaction is characterized by the formation of a stable jump upstream of the obstacle as the fluid accumulates against it. The fluid climbs the upstream face of the obstacle and then passes over it, creating a distinct wake region immediately downstream. The effect of the inclination is evident in the flow behavior. For the steeper 4.65° channel, the height of the fluid immediately after the obstacle is significantly higher compared to the 0° case at similar time steps.

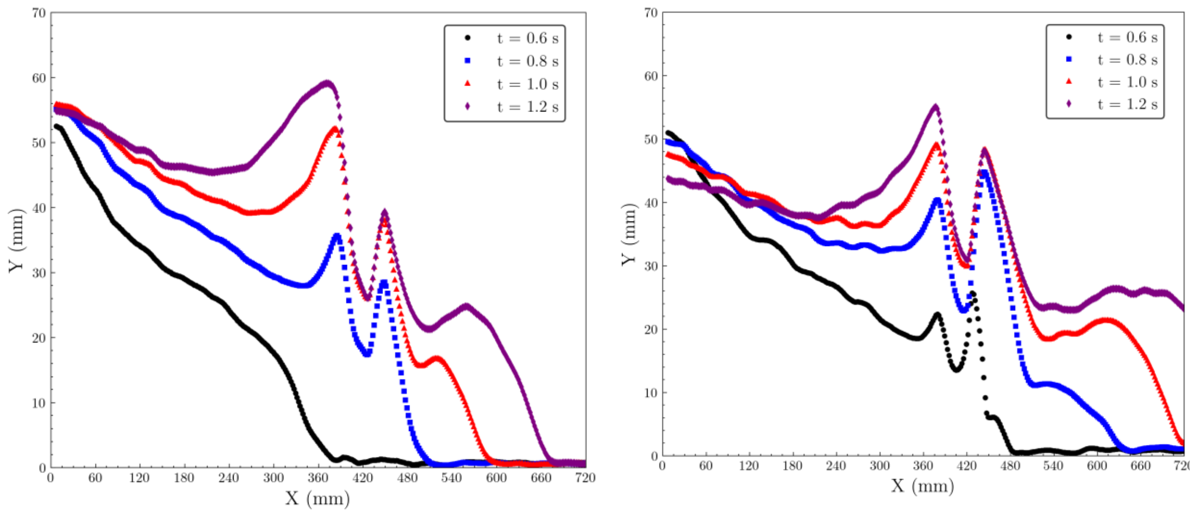

Figure 4. 58. Longitudinal flow-height profiles of the fluid over a bottom obstacle for two bed inclinations: 0° (left) and 4.65° (right)

To investigate the backwater effects and impact dynamics generated by a downstream boundary, experiments were performed using the closed-end configuration at two bed inclinations (test cases no. 22 and 40). As represented in Figure 4.59, the channel slope has a pronounced influence on the wavefront celerity. In the horizontal channel, the flow propagates more slowly, and the wavefront does not reach the downstream wall (X = 720 mm) until t = 1.2 s. In contrast, in the inclined channel, the gravitational component accelerates the flow, causing the wavefront to advance more rapidly and strike the downstream boundary earlier. At t = 1.2 s, the inclined case also exhibits a clear backwater effect.

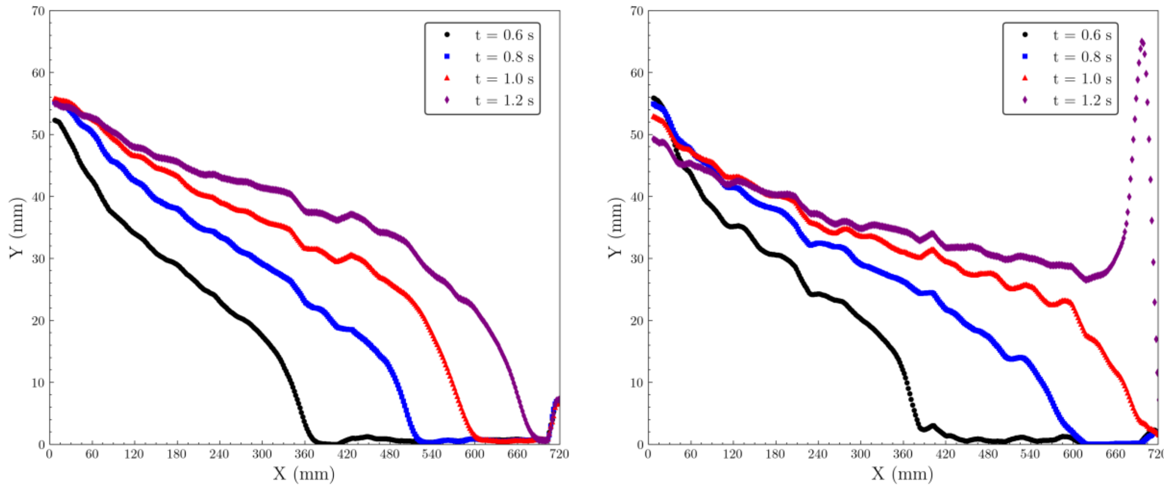

Figure 4. 59. Longitudinal flow depth profile fluid for closed-end configuration for two bed inclinations: 0° (left) and 4.65° (right)

To evaluate the rheological effects, a series of control experiments were conducted using Newtonian fluid (water) under identical initial conditions (test cases no 31, 32 and 35). Figure 4.60 reports the longitudinal free-surface profiles for the open-end, closed-end, and obstacle configurations on a horizontal bed. The results clearly show that the Newtonian fluid exhibits distinct kinematic behavior compared with the non-Newtonian cases. The water wavefront propagates with significantly higher celerity, and the profiles display a sharp, wedge-shaped front rather than the convex shape observed in the non-Newtonian tests.

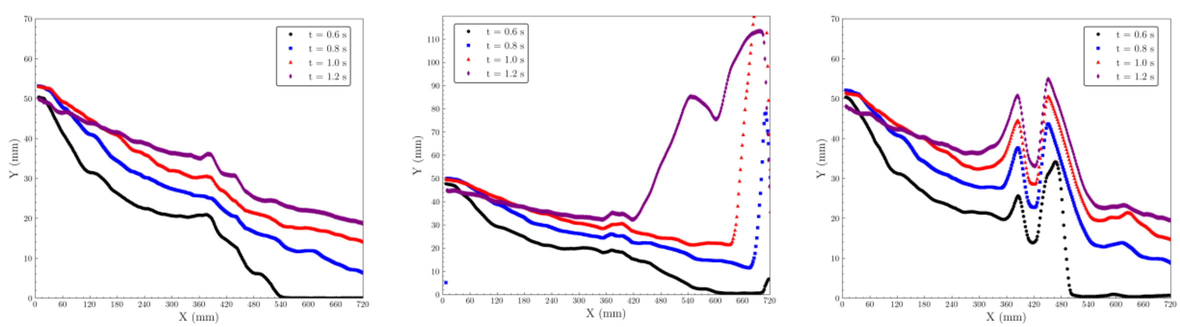

Figure 4. 60. Longitudinal free-surface profiles for the Newtonian fluid (water) on a horizontal bed: open-end (left), closed-end (center) and presence of obstacle (right)

4.3.3.2. PIV image processing and velocity field reconstruction

The raw experimental data including of high-speed image sequences captured by the PIV camera was subjected a comprehensive multi-stage analysis to extract accurate velocity vector fields. The processing workflow was divided into three main phases: initial image pre-processing (custom MATLAB scripting), PIV analysis using the PIVlab toolbox, and final data post-processing.

1. Initial Image Pre-processing and Synchronization

Before performing the PIV analysis, the raw images required enhancement to maximize the contrast between the tracer particles and the fluid background. For this purpose, a custom MATLAB code was developed by S. Martínez-Aranda from Zaragoza University.

Synchronization: The precise initiation of the flow (time t=0) was determined by detecting the state of an LED synchronized with the gate mechanism. The specific frame corresponding to the gate opening (dam break) was identified through manual visual inspection of the LED's illumination status. This start-frame index was then manually input into the MATLAB code to define the temporal origin of the event.

Image Inversion and Contrast Enhancement: The non-Newtonian fluid was originally opaque due to the addition of Titanium Dioxide, while the tracer particles were distinct. To facilitate particle tracking, an image inversion filter was applied. This process transformed the white fluid background into a dark canvas, while the plastic tracer particles were inverted to appear as bright, high-intensity spots (Figure 4.61). Several filter iterations were tested, and the optimal configuration was selected to minimize noise and maximize particle distinctness.

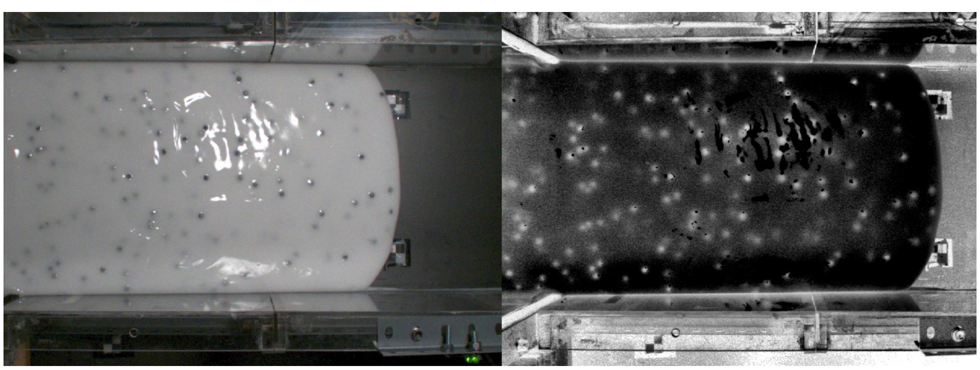

Figure 4. 61. Comparison of the original PIV image (left) and the processed image with filter applied (right)

2. Particle Image Velocimetry (PIV) Analysis

The core velocity analysis was conducted using PIVlab, a time-resolved particle image velocimetry toolbox for MATLAB (Stamhuis and Thielicke, 2014). The fundamental principle involved dividing the image into small sub-windows (Interrogation Areas) and computing the cross-correlation between two consecutive frames to determine the most probable particle displacement over the time interval. The PIVlab workflow consisted of the following steps:

- Pre-processing within PIVlab: Secondary image enhancements were applied using PIVlab's built in pre-processing module. Filters were adjusted to further equalize the histogram and sharpen particle intensities, ensuring high-quality input for cross-correlation.

- PIV Settings and Algorithms: The analysis utilized the " FFT Window Deformation" algorithm with a multi-pass strategy. This approach iteratively refines the interrogation window size to capture both large-scale flow structures and small-scale fluctuations with high resolution. An optimal Interrogation Area (IA) size was selected to balance spatial resolution with the signal-to-noise ratio (see Figure 4.62).

- PIVlab calibration

Spatial calibration: To convert pixel coordinates into physical units (meters), a calibration image was used. Reference points located at a known distance on the channel bed were identified, allowing the calculation of the scaling factor (pixels/meter).

Temporal calibration: The time step was defined by inputting the specific frame rate (frequency) of the high-speed camera used during data acquisition.

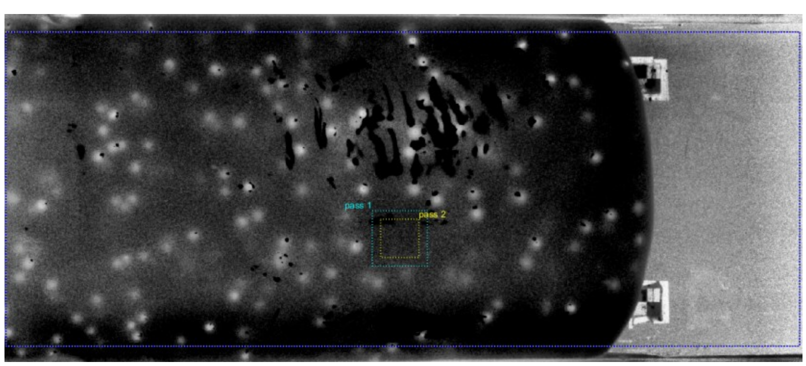

Figure 4. 62. The multi-pass interrogation area configuration employed in PIVlab and the reference markers at the channel bottom used for spatial calibration

- PIVlab Validation

Post-correlation validation was performed to identify and correct spurious vectors. Velocity vectors that deviated significantly from their neighbors were detected using median filters and replaced through interpolation to ensure a smooth and physically realistic vector field (see Figure 4.63).

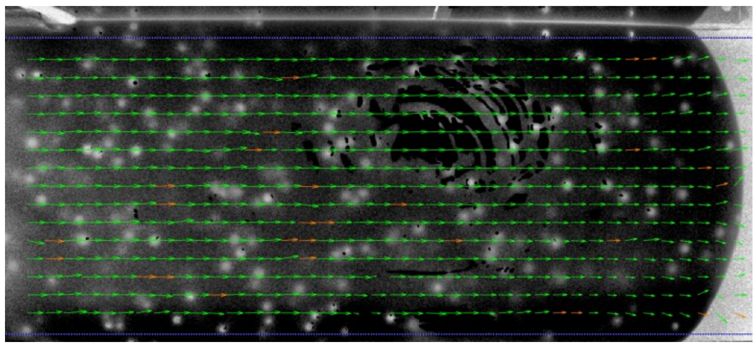

Figure 4. 63. Validated PIV velocity vector field showing accepted (green) and corrected (red) vectors

3. Data Export and Post-Processing

After completion of the PIV analysis, the validated velocity vector fields were exported for final processing. These datasets were subsequently imported into a custom MATLAB script. Utilizing the camera calibration files, the final velocity vectors were computed and mapped to the physical domain for rheological analysis. Figure 4.64 shows the velocity vector at t=1s for test case no. 3.

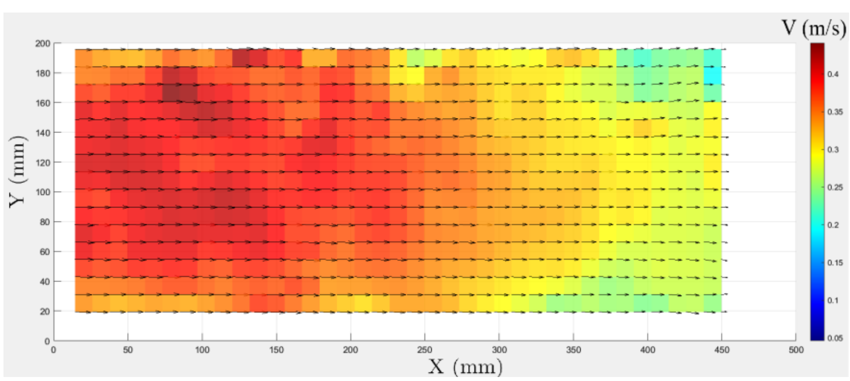

Figure 4. 64. Velocity vector field is mapped to the physical domain

Figure 4.65 depicts the longitudinal velocity at the center of flume for different times (0.6s, 0.8s, 1.0s and 1.2s) after opening the gate for non-Newtonian fluid with original rheology by initial flow depth equal to 0.12m (test case no. 3).

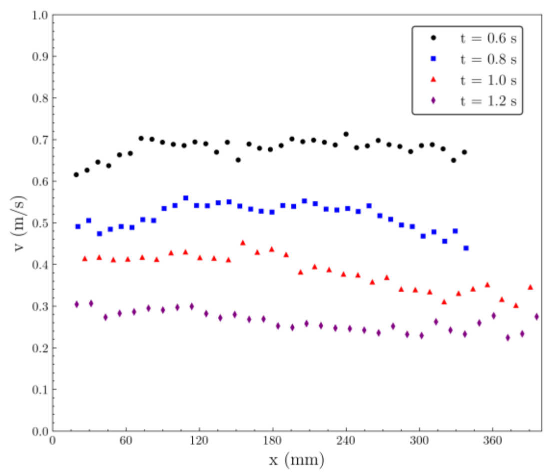

Figure 4. 65. Longitudinal velocity for different times (0.6s, 0.8s, 1.0s and 1.2s)

4.3.4. Comparison of experimental results and PVSPH simulation

A single test case was selected (test case no. 8) for the comparison between the experimental observations and the PVSPH numerical simulation: a dry-bed configuration employing the second rheological fluid modeled with the Herschel–Bulkley constitutive law, under an open-end setup with an initial flow depth of 0.12 m.

To simulate this rheology, the Herschel–Bulkley (HB) model was applied. In order to properly account for the yield stress, an apparent viscosity approach with regularization was adopted. Specifically, to avoid numerical divergence at zero shear rates—where viscosity would theoretically approach infinity—a cut-off shear rate (minimum threshold) was introduced. Below this threshold, viscosity was capped at a maximum value, thereby ensuring numerical stability and providing a realistic approximation of the unyielded regions (see Eq. 2.63).

Figure 4.66(a) compares the free-surface profiles from both the experimental measurements and the PVSPH simulation at t = 1.0 s. As observed, both results exhibit the same fluid depth of 0.056 m at the gate location. However, while the overall wave propagation appears approximately similar, notable discrepancies are present in the curvature of the wave profile. In contrast, Figure 4.66(b) compares the flow-propagation velocity profiles, demonstrating a highly satisfactory agreement between the experimental data and the PVSPH solution.

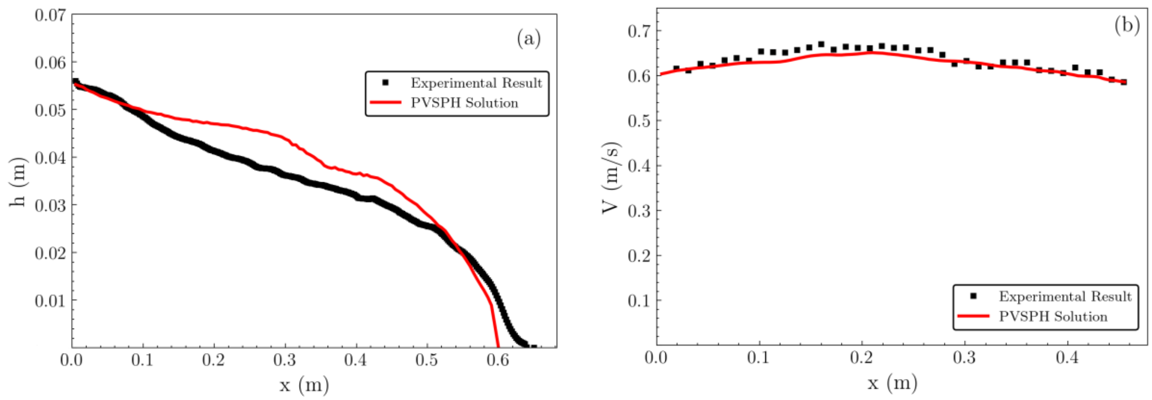

Figure 4. 66. Comparison between Experimental results and PVSPH solution at t=1.0 s: (a) Free-surface elevation profiles; (b) Velocity distribution profiles

5. Conclusions and future work

5.1. Conclusions

In modelling non-Newtonian fluids such as mudflow and debris flow, early research relied heavily on empirical observations, laboratory tests, and simplified analytical approaches. More recent studies have increasingly integrated theoretical developments with advanced numerical methods. Within this context, Smoothed Particle Hydrodynamics (SPH) has emerged as a suitable technique for simulating free-surface flows and analyzing the complex dynamics of mud and debris flows. This study investigated the propagation of mudflows through dam-break simulations using a Weakly-Compressible Smoothed Particle Hydrodynamics (PVSPH) model, with emphasis on assessing its capability to reproduce non-Newtonian behavior and the influence of clay concentration.

- Validation against SPHERIC dry-bed dam-break benchmark tests confirmed the accuracy of the PVSPH model for Newtonian flows. The model reproduced the wave-front shape and propagation with excellent agreement, achieving RMSE values below 3% and demonstrating strong predictive performance in simulating fluid behavior.

- For second validation under wet-bed conditions with downstream layers of 0.018 m and 0.038 m, the PVSPH model also showed essential flow features—such as the formation of a vertical mushroom-shaped jet and plunging bubble. Although the RMSE values were higher (13–20% for the 0.038 m case), the overall agreement in wave evolution and front dynamics remained satisfactory.

- To assess the accuracy of PVSPH model for non-Newtonian fluid dynamics, plane Poiseuille flow was selected as a benchmark test. The comparison between the analytical and simulated velocity profiles demonstrates the PVSPH model's ability to accurately replicate fluid behavior, with correlation coefficients ranging from 0.958 to 0.997 across different rheological indices. These findings confirm the PVSPH method’s strong accuracy in predicting fluid behavior across a variety of rheological conditions. Although this test primarily reflects one-dimensional fluid behavior, further validations are required for more complex flow scenarios.

- Simulations with and without a gate under wet-bed conditions showed that the gate introduces a slight delay in the initial wave propagation and produces a higher initial peak. As the flow evolves, these differences progressively diminish, indicating that the gate's influence is confined mainly to the early transient stage of the dam-break. Thus, the presence of the gate has a meaningful impact on the flow behavior only during the initial phase.

- Based on the results obtained from both the one-phase and two-phase (water-air) models, it can be concluded that the simulations produced acceptable outcomes. However, the results from the one-phase model were closer to the laboratory data.

- For the horizontal-bed open-end dam-break case with a Newtonian fluid (water), the PVSPH results agree well with the experimental data. The correlation is especially good for the prediction of the peak depth.

- Even in the scheme with a reverse slope bed, the maximum water depth estimated by the Newtonian model closely matches the experimental observations at the changing slope section. A good agreement between the experimental and PVSPH results is observed at the gate section.

- According to the Reynolds number results, shear-thinning fluids with rheological indices n =0.1, 0.2 exhibited laminar and transitional behavior, respectively. Since the SPH simulation does not include specific modeling for turbulent and transitional flow regimes, the simulation of fluid with a flow behavior index of n =0.2 should be treated with caution.

- At the gate section, the effect of the non-Newtonian rheology can be appreciated from the reduction in the peak value of the flow rate during the initial transient, while the further evolution of the dam-break flow appears to be dominated by inertial forces and, hence, it does not substantially differ from the turbulent flow case.

- The results presented in this work are applicable primarily to homogeneous mudflows and hyper concentrated flows.

- Non-Newtonian fluid with higher rheological index shows greater wave propagation speed compared to more non-Newtonian fluid with lower rheological index. The higher viscosity in the bulk flow dominates the non-Newtonian flow; however, the fluid viscosity decreases in the near-wall boundary layer due to shear-thinning rheological behavior.

- Non-Newtonian fluids propagated more slowly than water and formed steeper fronts. For reverse-slope and closed-end configurations, PVSPH predictions remained consistent with the Eulerian approaches.

- The results demonstrate that fluid consistency substantially influences wave propagation dynamics. Higher consistency fluids (n = 0.1) exhibit a similar downstream wave propagation speed, an anticipated surge due to the slope change and lower peak depths compared to water, while the lower consistency suspension (n = 0.2 shows essentially the same behaviour of the water wave, apart from a slightly lower peak depth. A possible interpretation might be that, for the mud with higher clay concentration, the more pronounced non-linear rheology leads to lower viscosities at high shear rates which, in turn, lead to a more rapid local response of the flow to the sudden slope change, compared to the less viscous cases (water and lower concentration clay suspension). On the other hand, in the slower process of the propagation of the reflected wave, dissipative effects due to the higher viscosity prevail and lead to overall lower water depths.

- Comparative analysis with two Eulerian approaches—the Depth Averaged Model (EDAM) and the Depth Resolved Model (EDRM)— in the simulation of dam-break waves of power-law fluid over initially dry beds revealed generally consistent predictions across all three numerical methods for both horizontal and adverse slope configurations. The PVSPH model exhibited comparable accuracy to the Eulerian models while offering the advantage of a mesh-free formulation, particularly beneficial for free-surface flows and complex geometries.

- In dam-break simulations for power law fluids at the gate section, the numerical results showed consistent agreement between PVSPH, EDAM, and EDRM for both horizontal and adverse slopes.

- Minor discrepancies were observed among the three numerical approaches during interaction of the wave with the downstream channel end and the bottom slope. The EDRM model occasionally predicted higher peak values and showed more pronounced fluctuations. However, the overall agreement among the models confirms the reliability of the SPH approach for mudflow simulations.

- Experimental tests conducted at the Zaragoza laboratory for shear-thinning fluids with yield stress demonstrated that the PVSPH model achieves highly satisfactory agreement with physical measurements regarding flow velocity distributions and fluid depths at the gate, despite minor discrepancies observed in the wave profile curvature.

Overall, the PVSPH model demonstrated several advantages, including computational efficiency, natural handling of free surfaces, and accurate representation of non-Newtonian rheology. The close agreement between numerical predictions and experimental data confirms that SPH is a valuable tool for simulating complex fluid dynamics and has strong potential for applications in mudflow hazard assessment and mitigation design.

5.2. Applicability to Real-World Mudflow and Debris Flow Events

The validation of the PVSPH code against experimental dam-break benchmarks showed that the model can reliably capture the main features of free-surface flows with non-Newtonian behaviour. This provides a meaningful indication of its potential for simulating real mudflow and debris-flow scenarios, a field where SPH has seen increasing application in recent years (e.g., Wang et al., 2016; Yeylaghi et al., 2017)

One clear advantage is the Lagrangian framework of the SPH method, which avoids the use of a fixed computational mesh. This makes the PVSPH model particularly suitable for representing flows over complex and irregular terrains, such as those typically found in mountainous areas where mudflows develop (Violeau and Rogers, 2016). In situations where Eulerian approaches may struggle with mesh deformation or difficulties in tracking moving interfaces, the present model naturally handles large deformations and interactions with uneven bed geometries.

Another important aspect is the implementation of the generalized Power-Law rheology, which allows the model to reproduce the shear-thinning response commonly observed in natural mud suspensions (Ng and Mei, 1994). The Power-Law rheology is suitable for flows strongly influenced by the behaviour of the finer mud matrix. The simulations carried out in this work show that the PVSPH code is capable of reproducing the propagation speed and flow depth of shear-thinning fluids, two quantities that are essential for hazard assessment and the design of protective structures.

For fluids characterized by rheology in which a yield stress is present, an extension of the current model to Herschel–Bulkley or Bingham formulations (Zhu et al., 2010) is required. Large-scale simulations also significantly increase the computational cost, making the adoption of high-performance computing strategies, such as the parallelization (Jagtap et al., 2021; Shi and Huang, 2022).

5.3. Future work

The findings derived from this research are highly encouraging, particularly given that the use of SPH for real-world engineering challenges is still in its early stages and that the method is still undergoing significant developments. Based on the findings, the following recommendations are proposed for future developments:

- Increasing the computational speed and number of particles in Smoothed Particle Hydrodynamics (SPH) simulations through the use of parallel computing, while maintaining caution to ensure accuracy and stability.
- Extend the Smoothed Particle Hydrodynamics approach to three-dimensional simulations of non-Newtonian dam-break flows.
- SPH simulations of dam-break scenarios with non-Newtonian fluids by investigating the impact of wet and rough bed conditions downstream.
- Processing the available experimental test data and comparing the results with the outputs of the numerical models, particularly focusing on the estimation of impact forces on obstacles.
- Enhance the PVSPH model by incorporating more advanced rheological laws (e.g., Herschel–Bulkley) and validate them against experimental non-Newtonian dam-break tests.

List of References

Adrian, R.J., 1984. Scattering particle characteristics and their effect on pulsed laser measurements of fluid flow: speckle velocimetry vs particle image velocimetry. Applied optics 23, 1690–1691.

Amicarelli, A., Kocak, B., Sibilla, S., Grabe, J., 2017. A 3D smoothed particle hydrodynamics model for erosional dam-break floods. International Journal of Computational Fluid Dynamics 31, 413–434. https://doi.org/10.1080/10618562.2017.1422731

Ancey, C., 2007. Plasticity and geophysical flows: A review. Journal of non-Newtonian fluid mechanics 142, 4–35.

Anderson, J.D., 2002. Computational fluid dynamics: the basics with applications. McGraw-Hill New York.

Andrea, D., Giovanni, L., George, C., Francesco, D., Cristiana, D., Iervolino, M., Angelo, L., Vacca, A., 2024. Modelling the impact of a dam-break wave on a vertical wall. EARTH SURFACE PROCESSES AND LANDFORMS.

Aslami, M.H., Rogers, B.D., Stansby, P.K., Bottacin-Busolin, A., 2023. Simulation of floating debris in SPH shallow water flow model with tsunami application. Advances in Water Resources 171, 104363. https://doi.org/10.1016/j.advwatres.2022.104363

Ata, R., Soulaïmani, A., 2005. A stabilized SPH method for inviscid shallow water flows: STABILIZED SPH METHOD. Int. J. Numer. Meth. Fluids 47, 139–159. https://doi.org/10.1002/fld.801

Bai, Y., Tian, Q., 2011. Interaction between mud and wave in different rheological models [J]. Journal of Tianjin University (Science and Technology) 44, 196–201.

Berberović, E., van Hinsberg, N.P., Jakirlić, S., Roisman, I.V., Tropea, C., 2009. Drop impact onto a liquid layer of finite thickness: Dynamics of the cavity evolution. Physical Review E—Statistical, Nonlinear, and Soft Matter Physics 79, 036306.

Berti, M., Genevois, R., Simoni, A., Tecca, P.R., 1999. Field observations of a debris flow event in the Dolomites. Geomorphology 29, 265–274.

Bukreev, V.I., 2009. Force action of discontinuous waves on a vertical wall. Journal of applied mechanics and technical physics 50, 278–283.

Capone, T., 2009. SPH numerical modelling of impulse water waves generated by landslides.

Chanson, H., 2004. The hydraulics of open channel flow, 2nd ed. ed. Butterworth-Heinemann, Oxford.

Chen, Z., Shu, C., 2020. Simplified lattice Boltzmann method for non-Newtonian power-law fluid flows. Numerical Methods in Fluids 92, 38–54. https://doi.org/10.1002/fld.4771

Chen, Z., Zong, Z., Liu, M.B., Zou, L., Li, H.T., Shu, C., 2015. An SPH model for multiphase flows with complex interfaces and large density differences. Journal of Computational Physics 283, 169–188. https://doi.org/10.1016/j.jcp.2014.11.037

Chhabra, R.P., Richardson, J.F., 2004. Non-Newtonian flow and applied rheology. Engineering application., second Edition. ed. Elsevier Ltd.

Ciervo, F., Papa, M.N., Medina, V., Bateman, A., 2015. Simulation of flash floods in ungauged basins using post-event surveys and numerical modelling. Journal of flood risk management 8, 343–355.

COChARD, S., 2007. Measurements of time-dependent free-surface viscoplastic flows down steep slopes. Verlag nicht ermittelbar.

Colagrossi, A., Antuono, M., Le Touzé, D., 2009. Theoretical considerations on the free-surface role in the smoothed-particle-hydrodynamics model. Physical Review E—Statistical, Nonlinear, and Soft Matter Physics 79, 056701.

Colagrossi, A., Landrini, M., 2003. Numerical simulation of interfacial flows by smoothed particle hydrodynamics. Journal of Computational Physics 191, 448–475. https://doi.org/10.1016/S0021-9991(03)00324-3

Coussot, P., 2017. Mudflow rheology and dynamics. Routledge.

Coussot, P., 1994. Steady, laminar, flow of concentrated mud suspensions in open channel. Journal of Hydraulic Research 32, 535–559.

Crespo, A.J., Gómez-Gesteira, M., Dalrymple, R.A., 2008. Modeling Dam Break Behavior over a Wet Bed by a SPH Technique. J. Waterway, Port, Coastal, Ocean Eng. 134, 313–320. https://doi.org/10.1061/(ASCE)0733-950X(2008)134:6(313)

Cummins, S.J., Rudman, M., 1999. An SPH Projection Method. Journal of Computational Physics 152, 584–607. https://doi.org/10.1006/jcph.1999.6246

Cuomo, G., Panizzo, A., Dalrymple, R., 2007. SPH-LES TWO-PHASE SIMULATION OF WAVE BREAKING AND WAVE-STRUCTURE INTERACTION, in: Coastal Engineering 2006. Presented at the Proceedings of the 30th International Conference, World Scientific Publishing Company, San Diego, California, USA, pp. 274–286. https://doi.org/10.1142/9789812709554_0024

Dalrymple, R.A., Knio, O., 2001a. SPH Modelling of Water Waves, in: Coastal Dynamics ’01. Presented at the Fourth Conference on Coastal Dynamics, American Society of Civil Engineers, Lund, Sweden, pp. 779–787. https://doi.org/10.1061/40566(260)80

Dalrymple, R.A., Knio, O., 2001b. SPH modelling of water waves, in: Coastal Dynamics’ 01. pp. 779–787.

DARBY, R., 1988. Laminar flow and turbulent pipe flows of non-Newtonian fluids. Rheology and non-Newtonian Flows 19–54.

De Padova, D., Meftah, M.B., Mossa, M., Sibilla, S., 2022. A multi-phase SPH simulation of hydraulic jump oscillations and local scouring processes downstream of bed sills. Advances in Water Resources 159, 104097. https://doi.org/10.1016/j.advwatres.2021.104097

Di Cristo, C., Fecarotta, O., Iervolino, M., Vacca, A., 2022. Impact dynamics of mud flows against rigid walls. Journal of Hydrology 612, 128221.

Di Cristo, C., Iervolino, M., Vacca, A., 2014. Simplified wave models applicability to shallow mud flows modeled as power-law fluids. J. Mt. Sci. 11, 1454–1465. https://doi.org/10.1007/s11629-014-3065-6

Di Cristo, C., Iervolino, M., Vacca, A., 2012. Discussion of "Analysis of dynamic wave model for unsteady flow in an open channel" by Maurizio Venutelli. Journal of Hydraulic Engineering 138, 915–917.

Di Cristo, C., Iervolino, M., Vacca, A., 2013a. Waves dynamics in a linearized mud-flow shallow model. Applied Mathematical Sciences 7, 377–393.

Di Cristo, C., Iervolino, M., Vacca, A., 2013b. Boundary conditions effect on linearized mud-flow shallow model. Acta Geophysica 61, 649–667.

Di Cristo, C., Iervolino, M., Vacca, A., 2013c. On the applicability of minimum channel length criterion for roll-waves in mud-flows. J. Hydrol. Hydromech 61, 286–292.

Di Cristo, C., Iervolino, M., Vacca, A., Zanuttigh, B., 2009. Roll-waves prediction in dense granular flows. Journal of Hydrology 377, 50–58.

Divoux, T., Tamarii, D., Barentin, C., Manneville, S., 2010. Transient shear banding in a simple yield stress fluid. Physical review letters 104, 208301.

Dressler, R., 1954. Comparison of theories and experiments for the hydraulic dam-break wave. Proc. Int. Assoc. Scientific Hydrology Assemblee Generale, Rome, Italy, 1954 3, 319–328.

Dressler, R.F., 1952. Hydraulic resistance effect upon the dam-break functions. National Bureau of Standards Washington, DC.

Dutra Fraga Filho, C.A., 2019. Smoothed Particle Hydrodynamics: Fundamentals and Basic Applications in Continuum Mechanics. Springer International Publishing, Cham. https://doi.org/10.1007/978-3-030-00773-7

Ellero, M., Kröger, M., Hess, S., 2002. Viscoelastic flows studied by smoothed particle dynamics. Journal of Non-Newtonian Fluid Mechanics 105, 35–51. https://doi.org/10.1016/S0377-0257(02)00059-9

Ellero, M., Tanner, R.I., 2005. SPH simulations of transient viscoelastic flows at low Reynolds number. Journal of Non-Newtonian Fluid Mechanics 132, 61–72.

Fan, X.-J., Tanner, R.I., Zheng, R., 2010. Smoothed particle hydrodynamics simulation of non-Newtonian moulding flow. Journal of Non-Newtonian Fluid Mechanics 165, 219–226. https://doi.org/10.1016/j.jnnfm.2009.12.004

Ferrari, A., Dumbser, M., Toro, E.F., Armanini, A., 2009. A new 3D parallel SPH scheme for free surface flows. Computers & Fluids 38, 1203–1217. https://doi.org/10.1016/j.compfluid.2008.11.012

Forterre, Y., Pouliquen, O., 2003. Long-surface-wave instability in dense granular flows. Journal of Fluid Mechanics 486, 21–50.

Fourtakas, G., Rogers, B.D., 2016. Modelling multi-phase liquid-sediment scour and resuspension induced by rapid flows using Smoothed Particle Hydrodynamics (SPH) accelerated with a Graphics Processing Unit (GPU). Advances in Water Resources 92, 186–199. https://doi.org/10.1016/j.advwatres.2016.04.009

Gallati, M., Braschi, G., 2002. Numerical description of rapidly varied flows via SPH method, in: Proceedings of the IASTED International Conference on Applied Simulation and Modelling. pp. 25–28.

Gesteira, M.G., Rogers, B.D., Dalrymple, R.A., Crespo, J.C., Narayanaswamy, M., 2008. User guide for the SPHysics code.

Gingold, R.A., Monaghan, J.J., 1977. Smoothed particle hydrodynamics: theory and application to non-spherical stars. Monthly notices of the royal astronomical society 181, 375–389.

Gomez-Gesteira, M., 2004. Using a 3D SPH method for wave impact on a tall structure. J. Waterways, Port, Coastal, Ocean Engineering 130, 630–669.

Gómez-Gesteira, M., Dalrymple, R.A., 2004. Using a Three-Dimensional Smoothed Particle Hydrodynamics Method for Wave Impact on a Tall Structure. J. Waterway, Port, Coastal, Ocean Eng. 130, 63–69. https://doi.org/10.1061/(ASCE)0733-950X(2004)130:2(63)

Gomez-Gesteira, M., Rogers, B.D., Dalrymple, R.A., Crespo, A.J., 2010. State-of-the-art of classical SPH for free-surface flows. Journal of Hydraulic Research 48, 6–27.

Gotoh, H., Khayyer, A., 2018. On the state-of-the-art of particle methods for coastal and ocean engineering. Coastal Engineering Journal 60, 79–103.

Gottlieb, S., Shu, C.-W., 1998. Total variation diminishing Runge-Kutta schemes. Mathematics of computation 67, 73–85.

Gouet-Kaplan, M., Tartakovsky, A., Berkowitz, B., 2009. Simulation of the interplay between resident and infiltrating water in partially saturated porous media. Water Resources Research 45, 2008WR007350. https://doi.org/10.1029/2008WR007350

Grenier, N., Antuono, M., Colagrossi, A., Le Touzé, D., 2009. An Hamiltonian interface SPH formulation for multi-fluid and free surface flows. Computational Physics 228, 8380–8393.

Gu, S., Zheng, X., Ren, L., Xie, H., Huang, Y., Wei, J., Shao, S., 2017. SWE-SPHysics Simulation of Dam Break Flows at South-Gate Gorges Reservoir. Water 9, 387. https://doi.org/10.3390/w9060387

Hart, D.P., 2000. PIV error correction. Experiments in fluids 29, 13–22.

Harten, A., Lax, P.D., 1983. On Upstream Differencing and Godunov-Type Schemes for Hyperbolic Conservation Laws. SIAM Review, 25(1), 35-61.

Hejazi, K., Soltanpour, M., Aslani Kordkandi, A., 2023. An incompressible SPH numerical model for simulating wave and non-Newtonian mud interaction. Coastal Engineering 185, 104379. https://doi.org/10.1016/j.coastaleng.2023.104379

Hogg, A.J., Pritchard, D., 2004. The effects of hydraulic resistance on dam-break and other shallow inertial flows. J. Fluid Mech. 501, 179–212.

Hosseini, K., Omidvar, P., Kheirkhahan, M., Farzin, S., 2019. Smoothed particle hydrodynamics for the interaction of Newtonian and non-Newtonian fluids using the μ(I) model. Powder Technology 351, 325–337.

Hosseini, S.M., Manzari, M.T., Hannani, S.K., 2007. A fully explicit three-step SPH algorithm for simulation of non-Newtonian fluid flow. International Journal of Numerical Methods for Heat & Fluid Flow 17, 715–735. https://doi.org/10.1108/09615530710777976

Hu, X.Y., Adams, N.A., 2007. An incompressible multi-phase SPH method. Journal of computational physics 227, 264–278.

Huang, X., Garcia, M.H., 1998. A Herschel–Bulkley model for mud flow down a slope. Journal of fluid mechanics 374, 305–333.

Hughes, J.P., Graham, D.I., 2010. Comparison of incompressible and weakly-compressible SPH models for free-surface water flows. Journal of Hydraulic Research 48, 105–117.

Hungr, O., Morgan, G.C., Kellerhals, R., 1984. Quantitative analysis of debris torrent hazards for design of remedial measures. Canadian Geotechnical Journal 21, 663–677.

Imran, J., Harff, P., Parker, G., 2001. A numerical model of submarine debris flow with graphical user interface. Computers & geosciences 27, 717–729.

Iverson, R.M., 2000. Landslide triggering by rain infiltration. Water resources research 36, 1897–1910.

Iverson, R.M., 1997. The physics of debris flows. Reviews of geophysics 35, 245–296.

Jagtap, P., Nasre, R., Sanapala, V.S., Patnaik, B.S.V., 2021. Efficient parallelization of SPH algorithm on modern multi-core CPUs and massively parallel GPUs. International Journal of Modeling, Simulation, and Scientific Computing 12, 2150054.

Jandaghian, M., Krimi, A., Shakibaeinia, A., 2021. Enhanced weakly-compressible MPS method for immersed granular flows. Advances in Water Resources 152, 103908. https://doi.org/10.1016/j.advwatres.2021.103908

Janosi, I.M., Jan, D., Szabó, K.G., Tél, T., 2004. Turbulent drag reduction in dam-break flows. Experiments in Fluids 37, 219–229.

Jeng, C.-J., Sue, D.-Z., 2016. Characteristics of ground motion and threshold values for colluvium slope displacement induced by heavy rainfall: a case study in northern Taiwan. Natural Hazards and Earth System Sciences 16, 1309–1321.

Jiang, T., Ouyang, J., Li, Q., Ren, J., Yang, B., 2011. A corrected smoothed particle hydrodynamics method for solving transient viscoelastic fluid flows. Applied Mathematical Modelling 35, 3833–3853. https://doi.org/10.1016/j.apm.2011.02.014

Jing, L., Kwok, C.Y., Leung, Y.F., Zhang, Z., Dai, L., 2018. Runout scaling and deposit morphology of rapid mudflows. Journal of Geophysical Research: Earth Surface 123, 2004–2023.

Kattel, P., Kafle, J., Fischer, J.-T., Mergili, M., Tuladhar, B.M., Pudasaini, S.P., 2018. Interaction of two-phase debris flow with obstacles. Engineering Geology 242, 197–217.

Khanpour, M., Zarrati, A.R., Kolahdoozan, M., Shakibaeinia, A., Amirshahi, S.M., 2016. Mesh-free SPH modeling of sediment scouring and flushing. Computers & Fluids 129, 67–78. https://doi.org/10.1016/j.compfluid.2016.02.005

Khayyer, A., Gotoh, H., 2010. On particle-based simulation of a dam break over a wet bed. Journal of Hydraulic Research 48, 238–249. https://doi.org/10.1080/00221681003726361

Kim, S., 2002. A study of non-Newtonian viscosity and yield stress of blood in a scanning capillary-tube rheometer. Drexel University.

Kitsionas, S., Whitworth, A.P., 2002. Smoothed particle hydrodynamics with particle splitting, applied to self-gravitating collapse. Monthly Notices of the Royal Astronomical Society 330, 129–136.

Laigle, D., Labbe, M., 2017. SPH-Based Numerical Study of the Impact of Mudflows on Obstacles. IJECE 10, 56–66. https://doi.org/10.13101/ijece.10.56

Lauber, G., Hager, W.H., 1998. Experiments to dambreak wave: Horizontal channel. Journal of Hydraulic research 36, 291–307.

Lee, C., Bathe, K.-J., Noh, G., 2024. Stability of the Bathe implicit time integration methods in the presence of physical damping. Computers & Structures 295, 107294.

Lee, E.-S., Moulinec, C., Xu, R., Violeau, D., Laurence, D., Stansby, P., 2008. Comparisons of weakly compressible and truly incompressible algorithms for the SPH mesh free particle method. Journal of Computational Physics 227, 8417–8436. https://doi.org/10.1016/j.jcp.2008.06.005

LeVeque, R.J., 2002. Finite volume methods for hyperbolic problems. Cambridge university press.

Li, D., Li, X., Lin, Y., 2011. Numerical simulation of droplet impacting liquid surface by SPH. Science China Technological Sciences 54, 1873–1880.

Li, L., Gupta, V., Li, X., Reynolds, A.P., Grant, G., Soulami, A., 2022. Meshfree simulation and experimental validation of extreme thermomechanical conditions in friction stir extrusion. Comp. Part. Mech. 9, 789–809. https://doi.org/10.1007/s40571-021-00445-7

LI, T., JIA, Y., LI, H., ZHENG, B., ZHOU, N., QI, H., 2023. Simulation method of dam break flood propagation based on improved SPH model. Advances in Water Science 34, 744–752.

Libersky, L.D., Petschek, A.G., Carney, T.C., Hipp, J.R., Allahdadi, F.A., 1993. High Strain Lagrangian Hydrodynamics: A Three-Dimensional SPH Code for Dynamic Material Response. Journal of Computational Physics 109, 67–75. https://doi.org/10.1006/jcph.1993.1199

Lind, S.J., Xu, R., Stansby, P.K., Rogers, B.D., 2012. Incompressible smoothed particle hydrodynamics for free-surface flows: A generalised diffusion-based algorithm for stability and validations for impulsive flows and propagating waves. Journal of Computational Physics 231, 1499–1523. https://doi.org/10.1016/j.jcp.2011.10.027

Liu, G.R., Liu, M.B., 2003. Smoothed particle hydrodynamics: a meshfree particle method. World Scientific, New Jersey.

Liu, M., Liu, G., Lam, K., 2002. Investigations into water mitigation using a meshless particle method. Shock. Waves 12, 181–195.

Liu, M., Liu, G.-R., 2015. Particle methods for multi-scale and multi-physics. World Scientific.

Liu, Y., Balmforth, N.J., Hormozi, S., Hewitt, D.R., 2016. Two–dimensional viscoplastic dambreaks. Journal of Non-Newtonian Fluid Mechanics 238, 65–79.

Lucy, L.B., 1977. A numerical approach to the testing of the fission hypothesis. Astronomical Journal, vol. 82, Dec. 1977, p. 1013-1024. 82, 1013–1024.

Luu, L.-H., Philippe, P., Chambon, G., 2015. Experimental study of the solid-liquid interface in a yield-stress fluid flow upstream of a step. Physical review E 91, 013013.

Macosko, C.W., 1994. Rheology: principles, measurements, and applications, Advances in interfacial engineering series. VCH, New York.

Manciola, P., Mazzoni, A., Savi, F., 1994. Formation and propagation of steep waves: an investigative experimental interpretation, in: Modelling of Flood Propagation Over Initial Dry Areas. American Society of Civil Engineers/ASCE: 345 East 47th Street, New York …, pp. 283–297.

Martys, N.S., George, W.L., Chun, B.-W., Lootens, D., 2010. A smoothed particle hydrodynamics-based fluid model with a spatially dependent viscosity: application to flow of a suspension with a non-Newtonian fluid matrix. Rheol Acta 49, 1059–1069. https://doi.org/10.1007/s00397-010-0480-7

Minussi, R.B., Maciel, G. de F., 2012. Numerical experimental comparison of dam break flows with non-Newtonian fluids. Journal of the Brazilian Society of Mechanical Sciences and Engineering 34, 167–178.

Molteni, D., Colagrossi, A., Colicchio, G., 2007. On the use of an alternative water state equation in SPH, in: Proc. SPHERIC, 2nd Intl Workshop, Universidad Politécnica de Madrid, Spain, May. pp. 23–26.

Monaghan, J.J., 1997. Implicit SPH drag and dusty gas dynamics. Journal of Computational Physics 138, 801–820.

Monaghan, J.J., 1994. Simulating free surface flows with SPH. Journal of computational physics 110, 399–406.

Monaghan, J.J., 1992. Smoothed particle hydrodynamics. In: Annual review of astronomy and astrophysics. Vol. 30 (A93-25826 09-90), p. 543-574. 30, 543–574.

Monaghan, J.J., 1989. On the problem of penetration in particle methods. Journal of Computational physics 82, 1–15.

Monaghan, J.J., Kocharyan, A., 1995. SPH simulation of multi-phase flow. Computer Physics Communications 87, 225–235.

Monaghan, J.J., Kos, A., 1999. Solitary Waves on a Cretan Beach. J. Waterway, Port, Coastal, Ocean Eng. 125, 145–155. https://doi.org/10.1061/(ASCE)0733-950X(1999)125:3(145)

Monaghan, J.J., Lattanzio, J.C., 1985. A refined particle method for astrophysical problems. Astronomy and Astrophysics (ISSN 0004-6361), vol. 149, no. 1, Aug. 1985, p. 135-143. 149, 135–143.

Morris, J.P., 1996. Analysis of smoothed particle hydrodynamics with applications. Monash University Australia.

Morris, J.P., 1995. A study of the stability properties of SPH. arXiv preprint astro-ph/9503124.

Morris, J.P., Fox, P.J., Zhu, Y., 1997. Modeling low Reynolds number incompressible flows using SPH. Journal of computational physics 136, 214–226.

Mulligan, R.P., Franci, A., Celigueta, M.A., Take, W.A., 2020. Simulations of landslide wave generation and propagation using the particle finite element method. Journal of Geophysical Research: Oceans 125, e2019JC015873.

Ng, C.-O., Mei, C.C., 1994. Roll waves on a shallow layer of mud modelled as a power-law fluid. J. Fluid Mech. 263, 151–184. https://doi.org/10.1017/S0022112094004064

Ni, X., Sheng, J., Feng, W., 2016. Simulation of Free-Surface Flow Using the Smoothed Particle Hydrodynamics (SPH) Method with Radiation Open Boundary Conditions. Journal of Atmospheric and Oceanic Technology 33, 2435–2460. https://doi.org/10.1175/JTECH-D-15-0179.1

O'Brien, J.S., 2003. Reasonable assumptions in routing a dam break mudflow, in: 3rd Conference on Mud and Debris Flows on Proceeding of Debris Flow Hazards Mitigation: Mechanics, Prediction, and Assessment.

OpenCFD Ltd., 2016. User Guide: interFoam.

Ostwald, W., 1929. Ueber die rechnerische Darstellung des Strukturgebietes der Viskosität. Kolloid-Zeitschrift 47, 176–187.

Pan, W., Tartakovsky, A.M., Monaghan, J.J., 2013. Smoothed particle hydrodynamics non-Newtonian model for ice-sheet and ice-shelf dynamics. Journal of Computational Physics 242, 828–842. https://doi.org/10.1016/j.jcp.2012.10.027

Papa, M.N., Medina, V., Ciervo, F., Bateman, A., 2013. Derivation of critical rainfall thresholds for shallow landslides as a tool for debris flow early warning systems. Hydrology and Earth System Sciences 17, 4095–4107.

Pozorski, J., Olejnik, M., 2024. Smoothed particle hydrodynamics modelling of multiphase flows: an overview. Acta Mech 235, 1685–1714. https://doi.org/10.1007/s00707-023-03763-4

Rafiee, A., Manzari, M.T., Hosseini, M., 2007. An incompressible SPH method for simulation of unsteady viscoelastic free-surface flows. International Journal of Non-Linear Mechanics 42, 1210–1223. https://doi.org/10.1016/j.ijnonlinmec.2007.09.006

Randles, P., Libersky, L.D., 1996. Smoothed particle hydrodynamics: some recent improvements and applications. Computer methods in applied mechanics and engineering 139, 375–408.

Ritter, A., 1892. Die fortpflanzung der wasserwellen. Zeitschrift des vereines deutscher ingenieure 36, 947–954.

Rogers, B.D., Dalrymple, R.A., Gesteira, M., Knio, O., 2003. Smoothed particle hydrodynamics for naval hydrodynamics, in: Proc. Int. Workshop on Water Waves and Floating Bodies.

Sakakiyama, T., Byker, E.W., 1989. Mass Transport Velocity in Mud Layer Due to Progressive Waves. J. Waterway, Port, Coastal, Ocean Eng. 115, 614–633. https://doi.org/10.1061/(ASCE)0733-950X(1989)115:5(614)

Savage, S.B., Hutter, K., 1989. The motion of a finite mass of granular material down a rough incline. Journal of fluid mechanics 199, 177–215.

Schaer, N., Vazquez, J., Dufresne, M., Isenmann, G., Wertel, J., 2018. On the determination of the yield surface within the flow of yield stress fluids using computational fluid dynamics. arXiv preprint arXiv:1808.00913.

Shao, S., Lo, E.Y.M., 2003. Incompressible SPH method for simulating Newtonian and non-Newtonian flows with a free surface. Advances in Water Resources 26, 787–800. https://doi.org/10.1016/S0309-1708(03)00030-7

Shi, H., Huang, Y., 2022. A GPU-Based _-Plus-SPH Model for Non-Newtonian Multiphase Flows. Water 14, 1734.

Shi, H., Si, P., Dong, P., Yu, X., 2019. A two-phase SPH model for massive sediment motion in free surface flows. Advances in Water Resources 129, 80–98. https://doi.org/10.1016/j.advwatres.2019.05.006

Sibilla, S., 2015. An algorithm to improve consistency in smoothed particle hydrodynamics. Computers & Fluids 118, 148–158.

Sibilla, S., 2008. SPH simulation of local scour processes. ERCOFTAC BULLETIN 76, 41–44.

Sibilla, S., Manenti, S., Cazzato, T., Colombo, F., Tomei, A.A., Redaelli, A., Manzoli, V., Consolo, F., 2020. Smoothed Particle Hydrodynamics multiphase modelling of an experimental microfluidic device for conformal coating of pancreatic islets. Medical engineering & physics 77, 19–30.

Simeunović, M., Steeb, H., 2019. Simulation of generalized Newtonian fluids with the Smoothed Particle Hydrodynamics method. Proc Appl Math and Mech 19, e201900494. https://doi.org/10.1002/pamm.201900494

Soltanpour, M., Samsami, F., 2011. A comparative study on the rheology and wave dissipation of kaolinite and natural Hendijan Coast mud, the Persian Gulf. Ocean Dynamics 61, 295–309. https://doi.org/10.1007/s10236-011-0378-7

Stamhuis, E., Thielicke, W., 2014. PIVlab–towards user-friendly, affordable and accurate digital particle image velocimetry in MATLAB. Journal of open research software 2, 30.

Stansby, P.K., Chegini, A., Barnes, T., 1998. The initial stages of dam-break flow. Journal of Fluid Mechanics 374, 407–424.

Sturm, T.W., 2010. Open channel hydraulics. McGraw-Hill New York.

Swegle, J.W., Attaway, S.W., 1995. On the feasibility of using smoothed particle hydrodynamics for underwater explosion calculations. Computational Mechanics 17, 151–168.

Takahashi, T., 2007. Debris flow: mechanics, prediction and countermeasures. Taylor & Francis.

Takeda, H., Miyama, S.M., Sekiya, M., 1994. Numerical simulation of viscous flow by smoothed particle hydrodynamics. Progress of theoretical physics 92, 939–960.

Tang, J., Lin, P., Cui, P., 2022. Depth-resolved numerical model of dam break mud flows with Herschel-Bulkley rheology. Journal of Mountain Science 19, 1001–1017.

Tartakovsky, A.M., Ferris, K.F., Meakin, P., 2009. Lagrangian particle model for multiphase flows. Computer Physics Communications 180, 1874–1881. https://doi.org/10.1016/j.cpc.2009.06.002

Tartakovsky, A.M., Ward, A.L., Meakin, P., 2007. Pore-scale simulations of drainage of heterogeneous and anisotropic porous media. Physics of Fluids 19.

Vaughan, G.L., Healy, T.R., Bryan, K.R., Sneyd, A., Gorman, R.M., 2003. An SPH Model of a Seiching Basin.

Verlet, L., 1967. Computer" experiments" on classical fluids. I. Thermodynamical properties of Lennard-Jones molecules. Physical review 159, 98.

Violeau, D., 2012. Fluid mechanics and the SPH method: theory and applications. Oxford University Press.

Violeau, D., Rogers, B.D., 2016. Smoothed particle hydrodynamics (SPH) for free-surface flows: past, present and future. Journal of Hydraulic Research 54, 1–26. https://doi.org/10.1080/00221686.2015.1119209

Wang, W., Chen, G., Han, Z., Zhou, S., Zhang, H., Jing, P., 2016. 3D numerical simulation of debris-flow motion using SPH method incorporating non-Newtonian fluid behavior. Nat Hazards 81, 1981–1998. https://doi.org/10.1007/s11069-016-2171-x

Wang, Z.-B., Chen, R., Wang, H., Liao, Q., Zhu, X., Li, S.-Z., 2016. An overview of smoothed particle hydrodynamics for simulating multiphase flow. Applied Mathematical Modelling 40, 9625–9655. https://doi.org/10.1016/j.apm.2016.06.030

Wendland, H., 1995. Piecewise polynomial, positive definite and compactly supported radial functions of minimal degree. Adv Comput Math 4, 389–396. https://doi.org/10.1007/BF02123482

Westerweel, J., 1997. Fundamentals of digital particle image velocimetry. Measurement science and technology 8, 1379.

Whitham, G.B., 1955. The Effects of Hydraulic Resistance in the Dam-Break Problem. Proceedings of the Royal Society of London. Series A, Mathematical and Physical Sciences 227, 399–407.

Xenakis, A.M., Lind, S.J., Stansby, P.K., Rogers, B.D., 2015. An incompressible SPH scheme with improved pressure predictions for free-surface generalised Newtonian flows. Journal of Non-Newtonian Fluid Mechanics 218, 1–15. https://doi.org/10.1016/j.jnnfm.2015.01.006

Xu, X., Ouyang, J., Yang, B., Liu, Z., 2013. SPH simulations of three-dimensional non-Newtonian free surface flows. Computer Methods in Applied Mechanics and Engineering 256, 101–116. https://doi.org/10.1016/j.cma.2012.12.017

Xu, X., Yu, W., 2025. SPH simulations of non-isothermal viscoplastic free-surface flows incorporating Herschel-Bulkley-Papanastasiou model. Computers & Fluids 287, 106491. https://doi.org/10.1016/j.compfluid.2024.106491

Ye, T., Pan, D., Huang, C., Liu, M., 2019. Smoothed particle hydrodynamics (SPH) for complex fluid flows: Recent developments in methodology and applications. Physics of Fluids 31, 011301. https://doi.org/10.1063/1.5068697

Yeylaghi, S., Moa, B., Buckham, B., Oshkai, P., Vasquez, J., Crawford, C., 2017. ISPH modelling of landslide generated waves for rigid and deformable slides in Newtonian and non-Newtonian reservoir fluids. Advances in Water Resources 107, 212–232. https://doi.org/10.1016/j.advwatres.2017.06.013

Yuan, T.-J., Qiu, L.-C., Zhao, K.-L., 2024. Two-phase two-layer SPH modeling of surge waves generated by debris flows. Ocean Engineering 295, 116841. https://doi.org/10.1016/j.oceaneng.2024.116841

Zainali, A., Tofighi, N., Shadloo, M.S., Yildiz, M., 2013. Numerical investigation of Newtonian and non-Newtonian multiphase flows using ISPH method. Computer Methods in Applied Mechanics and Engineering 254, 99–113. https://doi.org/10.1016/j.cma.2012.10.005

Zhou, X., Sun, Z., 2021. Numerical investigation of non-Newtonian power law flows using B-spline material point method. Journal of Non-Newtonian Fluid Mechanics 298, 104678. https://doi.org/10.1016/j.jnnfm.2021.104678

Zhu, H., Martys, N.S., Ferraris, C., Kee, D.D., 2010. A numerical study of the flow of Bingham-like fluids in two-dimensional vane and cylinder rheometers using a smoothed particle hydrodynamics (SPH) based method. Journal of Non-Newtonian Fluid Mechanics 165, 362–375. https://doi.org/10.1016/j.jnnfm.2010.01.012

Zou, S., 2007. Coastal sediment transport simulation by smoothed particle hydrodynamics. a dissertation submitted to The Johns Hopkins University in conformity with the requirements for the degree of Doctor of Philosophy.